eVTOL Arrival Sequencing and Scheduling

in On-Demand Urban Air Mobility

I.C. Kleinbekman

Technische Universiteit Delft

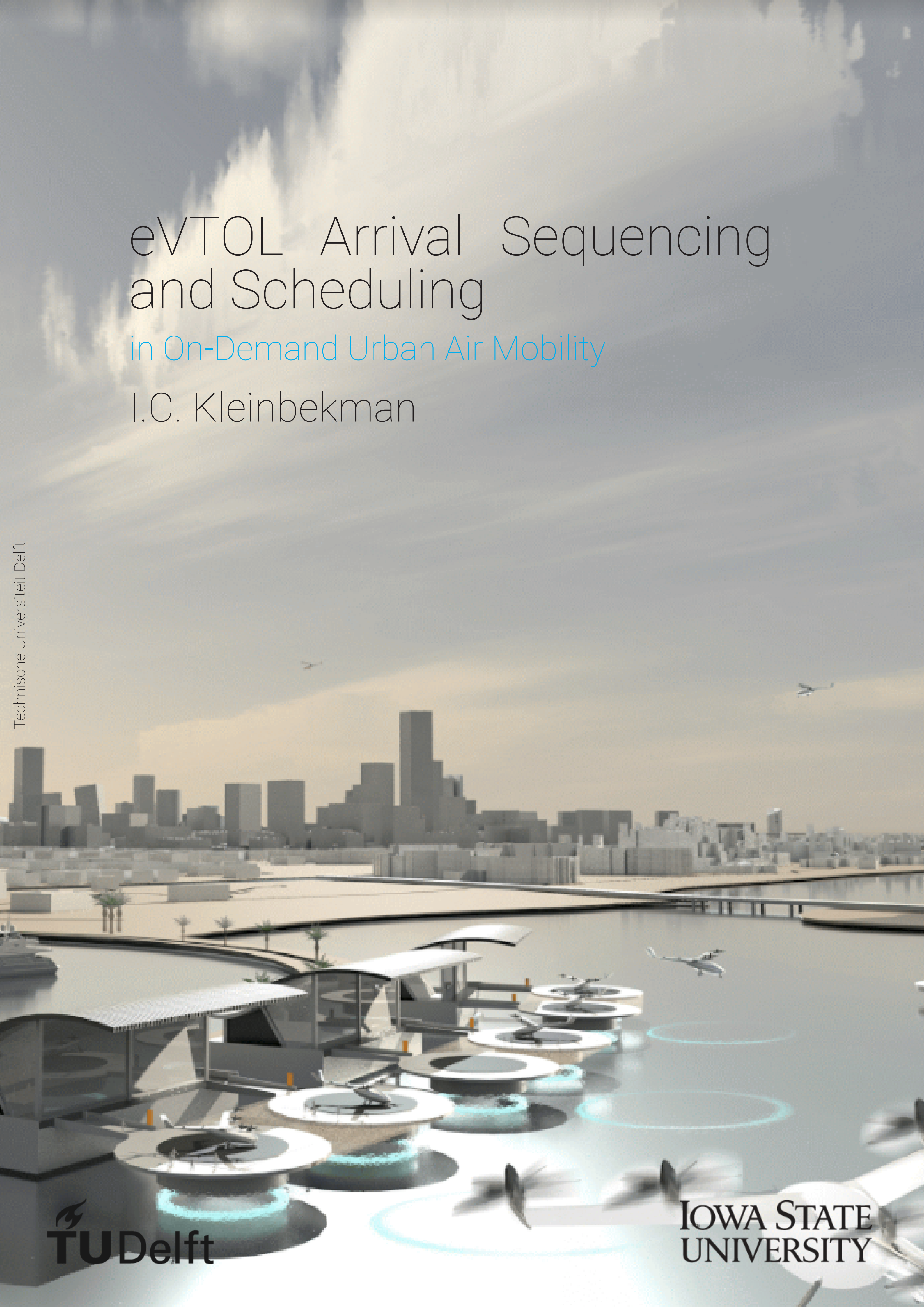

TUDelft

IOWA STATE UNIVERSITY

[1]

---

[1] Frontpage Image obtained from Uber Elevate

eVTOL Arrival Sequencing and Scheduling

in On-Demand Urban Air Mobility

by

I.C. Kleinbekman

to obtain the degree of Master of Science
at the Delft University of Technology,
to be defended publicly on Friday January 18, 2019 at 2:30 PM.

Student number:	4289757	
Project duration:	Jan 8, 2018 – Jan 18, 2019	
Thesis committee:	Dr. M.A. Mitici,	Delft University of Technology, supervisor
	Dr. P. Wei,	Iowa State University, supervisor
	Prof. Dr. R. Curran,	Delft University of Technology, section chair
	Dr. F. Oliviero,	Delft University of Technology, committee member

This thesis is confidential and cannot be made public until January 18, 2019.

TU Delft

IOWA STATE UNIVERSITY

Preface

This report is the final thesis deliverable for the obtainment of the degree of MSc. Aerospace Engineering. The research on eVTOL arrival sequencing and scheduling for on-demand urban air mobility is performed in collaboration with Iowa State University. The first part of the research was performed during the Spring semester in Ames, Iowa, U.S.A. as part of the Intelligent Aerospace Systems Lab (IASL). The thesis was finalised at the Air Transport & Operations department of the Delft University of Technology during the Fall semester. I would like to express my gratitude to Peng Wei, Priyank Pradeep, Guodung Zhu and the fellow IASL research group members for facilitating this collaboration and my stay in Iowa, taking me to company visits and making me feel at home. Also, I would like to thank Airbus Vahana A^3, the attendees of the Digital Aviation Systems Conference 2018 in London and Fabrizio Oliviero for their suggestions for improvement. At last, I am grateful for the constructive feedback and coaching provided by my daily supervisor at TU Delft, Mihaela Mitici.

I.C. Kleinbekman
Delft, January 3, 2019

Executive Summary

Urban Air Mobility (UAM) has the ability to reduce ground traffic congestion by enabling rapid on-demand flight through three-dimensional airspace. Due to the use of electric Vertical Take-Off and Landing (eVTOL) vehicles with distributed electric propulsion, UAM operates under zero operational emissions and cheaper and at a lower noise level compared to helicopters. In the long term with more UAM flights, air traffic control is expected to limit further growth of such operations. Therefore, first research has been performed on energy-efficient trajectory optimisation for a given required time of arrival, as the arrival phase is the most safety-critical flight phase with higher air traffic density and limited battery energy. However, research on the separation between eVTOL aircraft by computing their optimal required time of arrival (RTA) is limited. Besides, the available research has not considered limited battery power of the eVTOL aircraft or a limited vertiport landing pad capacity, neither discusses the ATC procedures for eVTOL flight.

Unlike fixed-wing aircraft or helicopters in commercial aviation, eVTOL aircraft fly on-demand and have different flight dynamics, limited battery energy supply and a limited number of landing spots at a vertiport such as on top of high-rise buildings. Therefore, this research has aimed to take the first step in the development of Urban Air Mobility Traffic Management for autonomous on-demand eVTOL operations by developing the arrival procedures and arrival sequencing and scheduling tool searching for minimum total delay considering limited battery power and vertiport landing pad capacity.

A concept of operations for vertiport terminal area airspace design has been proposed for a vertiport with one or two landing pads while making iterative use of the existing energy-efficient trajectory optimisation tool. A final approach area with a standard arrival route and two approach fixes is used to organise the flow inside the high-density area. Any scheduled delay is absorbed outside this area by flying a shallow descent, an approach fix detour or, only if necessary, in hover. The characteristics of the EHANG-184 multi-rotor eVTOL have been used throughout the research, such that a time separation requirement of $90s$ is determined.

This work is the first to compute the optimal RTAs for eVTOLs to safely separate them for minimum delay based on remaining battery state of charge and vertiport capacity in three modules. Module 1 computes the most energy-optimal arrival trajectory for a set of different RTAs at the vertiport. The state and control vectors corresponding to this set of trajectories are fed into Module 2. Also, the earliest and latest feasible arrival time based on flight dynamics, most energy-optimal arrival trajectory and the flight time between the approach fix and vertiport landing pad is obtained from this optimisation and fed into Module 3. Module 2 is used to relate the initial eVTOL battery status to the scheduler in Module 3. It first computes the power required to perform each of the RTA trajectories using the flight dynamics. Afterwards, the power demand and the required SOC to perform each RTA trajectory are determined using a simplified battery model. A regression is then created between the RTAs and the required SOC to compute the latest possible landing time based on the initial SOC of each arriving eVTOL. This so-called RTA constraint is an input for Module 3. Module 3 is a mixed-integer linear program which ensures eVTOL separation and selects the arrival route and corresponding landing pad for minimum total delay. A column generation algorithm has been applied to enable delay absorption in hover. Besides, it contains a position shifting constraint with respect to the first-come-first-serve sequence and a rolling horizon algorithm to reduce the computational time required to solve the model.

The concept of operations and eVTOL arrival sequencing and scheduling tool have been tested for a proof of concept and afterwards validated using a hexagonal vertiport network and eVTOL arrival demand model for Houston, TX, USA. The number of eVTOLs expected to arrive has been obtained from the demand model, after which the expected time of arrival for each eVTOL has been modelled as a Poisson process. The initial state of charge of the arriving eVTOLs has been assumed to be normally distributed.

The input has been solved both for a single and a double landing pad concept. It has been concluded that the double landing pad concept has a higher capacity than the single landing pad vertiport, also when hover is applied. Besides, a Monte Carlo simulation for the double landing pad concept has shown that the scheduled eVTOL delay is likely to stay within 1 minute (94%) or 3 minutes (96%) when arriving during a commuter peak or off-peak period, respectively. A simulation of one entire day has shown that most delay is created during the peak hours and that the maximum eVTOL arrival capacity at a double landing pad vertiport is approximately 60 eVTOLs/hr for a hub in the Houston network.

The sensitivity of the model has been tested for four model inputs or parameters, namely the number of position shifts in the Constrained Position Shifting, the time separation between eVTOL arrivals, the rolling horizon period length and the initial eVTOL battery state of charge (SOC) distribution. Where the position shift did not have a high impact on the results, the rolling horizon period highly influenced the computational time. Therefore, a rolling horizon period of 5 minutes is recommended for further research. Also, a decrease in the time separation requirement positively and significantly influenced the daily cumulative delay. It is thus recommended to flight test the minimally required separation to avoid creating redundant delay. At last, it has been concluded that the SOC influences the distribution of delay over the eVTOLs, but does not significantly impact the computational time nor the cumulative delay.

This research serves as a basis for further development of safe and efficient UAM operations. It is then recommended to test the model for different eVTOL types and vertiport networks and to extend the model with stochastic influences, e.g. weather conditions and sudden vertiport closure. Also, the algorithm can be incorporated with other departure scheduling and conflict detection and resolution models to reach the highest efficiency in Urban Air Mobility and enable autonomous flight. The model formulation can also be applied to Unmanned Aircraft System Traffic Management (UTM) by inserting new separation requirements and flight dynamics for smaller drones when optimising a high-density arrival terminal airspace.

Contents

List of Figures

List of Tables

Nomenclature

Greek symbols

α	Angle of Attack	°
$\Delta t^p_{l,af}$	Delay scheduled for eVTOL p due to flying through a different approach fix	s
Δt^p_e, Δt^p_l	Time that eVTOL p is scheduled to arrive before, after $ETA^p(A)$ or $ETA^p(B)$ by flying shallow descent	s
$\Delta t^p_{l,h}$	Time that eVTOL p is scheduled to hover	s
Δt^{pq}_{sep}	Time separation requirement between eVTOLs p and q	s
η_e	Efficiency of the motor in converting electrical to mechanical power	–
η_P	Efficiency of the rotors due to tip vortices	–
γ	Flight Path Angle	°
λ	eVTOL arrival rate	eVTOLs/hr
ρ	Air density	kg/m^3
θ	Pitch angle	°

Roman symbols

$A(t_k)$	Arrival variable taking 1 if there is an eVTOL arrival at vertiport during time t_k	–
a^p	Decision variable taking 1 if eVTOL p flies through approach fix A	–
c^p_e	Cost for eVTOL p to be one second early	–
c^p_l, $c^p_{l,af}$,$c^p_{l,h}$	Cost for eVTOL p to be one second late by flying a shallow descent, an approach fix divert, in hover	–
D	Drag	N
$D(t_k)$	Demand probability density function at timestep t_k	–
E	Energy	J
$ETA^p(A)$	Estimated Time of Arrival of eVTOL p at approach fix A	s
G	Set of arriving eVTOLs considered for optimisation	eVTOLs
g	Gravitational Acceleration	m/s^2
$I(t)$	Total current at time t	A
K	Maximum eVTOL position shift with respect to FCFS sequence	–
k	Planning period in the rolling horizon framework	min
m	Mass	g
M_4	Demand probability density function scalar	–

M^{pq}	Scalar to ensure convergence in arrival sequencing and scheduling of eVTOL p and q	–
N	Flight stage	–
N	Number of planning periods in the planning horizon of the rolling horizon algorithm	–
P_a	Parasite power	W
P_c	Power required to climb	W
P_d	Power demand	W
P_f	Profile power	W
P_r	Induced power	W
P_r	Required power	W
Q	Battery capacity	Ah
R	Radius of rotor	m
R_{FA}, R_{TMA}	Radius of Final Approach Area, Terminal Area	m
RTA^p, $RTA^p(A)$	Required Time of Arrival of eVTOL p at the vertiport landing pad, at approach fix A	s
RTA_e^p, RTA_l^p	Earliest, latest possible Required Time of Arrival of eVTOL p at the vertiport	s
$RTA_{e,lp}^p(A)$	Earliest possible Required Time of Arrival of eVTOL p at landing pad A	s
S	Time between eVTOL arrivals	s
s^{pq}	Decision variable taking 1 if eVTOL p arrives prior to eVTOL q	–
T	Thrust	N
t	Time	s
t_0	Time of start of arrival flight trajectory	s
t_f	Time of end of arrival flight trajectory	s
t_k	Time step	s
T_r	Thrust per rotor	N
$T_t^p(A)$	Transfer Time between approach fix A and the vertiport landing spot for eVTOL p	s
u	Uniform distributed random variable	–
V	True Airspeed	m/s
v_h	Induced velocity in hover	m/s
V_h	Ground speed	m/s
v_i	Induced velocity	m/s
V_n	Nominal battery voltage	V
V_x	Vertical speed	m/s
z^{pq}	Decision variable taking 1 if eVTOL p and eVTOL q fly through the same approach fix	–

List of Abbreviations

AF	Approach Fix
ATC	Air Traffic Control
ATM	Air Traffic Management
ConOps	Concept of Operations
CDA	Continuous Descent Approach
DEP	Distributed Electric Propulsion
DV	Decision Variable
ECM	Equivalent Circuit Model
ETA	Estimated Time of Arrival
eVTOL	Electric Vertical Take-Off and Landing
FA	Final Approach Area
MILP	Mixed-Integer Linear Programming
ODM	On-Demand Mobility
RTA	Required Time of Arrival
RUT	Remaining Useful Time
SF	Safety Factor
SLT	Scheduled Landing Time
SOC	State of Charge
STA	Scheduled Time of Arrival
TMA	Terminal Area
TOD	Top of Descent
TRACON	Terminal Radar Approach Control
UAM	Urban Air Mobility
UAS	Unmanned Aircraft System
UTM	Unmanned Aircraft System Traffic Management
VRS	Vortex Ring State
VTOL	Vertical Take-Off and Landing

I

Scientific Article

eVTOL Arrival Sequencing and Scheduling for On-Demand Urban Air Mobility

Imke C. Kleinbekman
MSc. Student Aerospace Engineering
Delft University of Technology
Delft, the Netherlands

Mihaela A. Mitici
Assistant Prof. Aerospace Engineering
Delft University of Technology
Delft, the Netherlands

Peng Wei
Assistant Prof. Aerospace Engineering
Iowa State University
Ames, IA, United States of America

Abstract*—Urban Air Mobility (UAM) has the ability to reduce ground traffic congestion by enabling rapid on-demand flight through three-dimensional airspace with zero operational emissions by using electric Vertical Take-Off and Landing (eVTOL) vehicles. In the long term with more UAM flights, air traffic control is expected to limit further growth of such operations. Therefore, a first research has been performed on energy-efficient trajectory optimisation for a given required time of arrival, as the arrival phase is the most safety-critical flight phase with much higher air traffic density and limited battery energy. However, research on the computation of the optimal required time of arrival (RTA) for eVTOL aircraft has not yet been performed. Unlike fixed-wing aircraft or helicopters in commercial aviation, eVTOL aircraft fly on-demand and have different flight dynamics, limited battery energy supply and a limited number of landing spots at a vertiport such as the top of high-rise buildings. This work is the first to utilise a mixed-integer linear program that computes the optimal RTAs for eVTOLs to safely separate them for minimum delay based on remaining battery state of charge and vertiport capacity. A concept of operations for vertiport terminal area airspace design is also proposed for a vertiport with one or two landing pads while making use of the existing energy-efficient trajectory optimisation tool. The concept of operations and eVTOL arrival sequencing and scheduling tool are validated using a hexagonal vertiport network and eVTOL arrival demand expected for Houston, TX, USA. The research serves as a basis for further development of safe and efficient UAM operations. The mathematical model can also be applied to Unmanned Aircraft System Traffic Management (UTM) by inserting new separation requirements and flight dynamics for smaller drones when optimising a high-density arrival terminal airspace.

***Index Terms*—Urban Air Mobility, on-demand, eVTOL, arrival, sequencing, scheduling**

I. INTRODUCTION

Urban Air Mobility (UAM) is an envisioned air transportation concept, where innovative aircraft could safely and efficiently transport passengers and cargo within urban areas by rising above traffic congestion on the ground. “The convergence of technologies, and new business models enabled by the digital revolution, is making it possible to explore this new way for people and cargo to move within our cities,” said Jaiwon Shin, NASA Associate Administrator for Aeronautics Research Mission Directorate. Companies such as Airbus, Bell, Embraer, Joby, Zee Aero, Pipistrel, Volocopter, and Aurora Flight Sciences are working with their battery vendors to build and test electric vertical take-off and landing (eVTOL) aircraft to ensure that vehicle safety and energy efficiency become an integral part of people’s daily commute. However, there is a lack of a concept of operations (ConOps) and air traffic control tools to support safe and efficient UAM operations with these new eVTOL aircraft. In this paper, we focus on designing the optimal UAM arrivals by integrating airspace design/configuration, trajectory optimisation, eVTOL battery modelling and arrival scheduling to enable safe and efficient flight operations in on-demand urban air transportation.

Unlike the small drones that can take off and land almost anywhere in the UAS Traffic Management (UTM) framework, eVTOL vehicles of UAM operations need to take off from and land at vertiports. When UAM operations are expected to increase, one of the major emerging bottlenecks will be the limited number of vertiports and landing pads, which will create a denser arrival UAM traffic in the corresponding terminal airspace. Therefore, we believe UAM arrival is the most safety-critical flight phase due to high-density terminal traffic, low remaining battery energy on eVTOLs, and limited resource of vertiport landing pads.

In this paper, we address the challenges of UAM arrival by developing an arrival sequencing and scheduling algorithm for multiple arriving eVTOL aircraft competing for limited terminal airspace and vertiport resources. Our approach is to formulate this problem as a mixed-integer linear program. We propose a ConOps for UAM terminal airspace design with multiple arrival fixes/routes. The objective is to minimise the total eVTOL arrival delay at the vertiport. Each eVTOL aircraft is constrained by its remaining battery energy and flight performance parameters. We provide an optimal required time of arrival (RTAs) to all the arriving eVTOLs, whose onboard avionics can then compute their energy-efficient optimal arrival trajectories using tools presented in [1], [2].

The remainder of this paper is as follows. In Section II we outline the current research on aircraft and eVTOL arrival sequencing and scheduling. In Section III we present our model for eVTOL arrival scheduling. The results for the EHANG-184 eVTOL are discussed in Section IV. A case study on eVTOL arrivals in Houston, TX, USA is performed in Section V. In Section VI we provide conclusions and recommendations.

II. RELATED LITERATURE

In recent years, several studies have been conducted for on-demand UAM, i.e., point-to-point air traffic operations that do not follow a pre-defined service schedule, as is the case of traditional commercial aviation. Most research efforts are focused on the current UAM concept definition, demand forecasting, and vehicle design. In [3] the UAM concept is described in terms of certification needs, infrastructure, traffic management, operational challenges. The nature of these challenges and quantification of their impact are researched in a case study on Los Angeles, USA [4]. The development of tools and analysis to support this investigation of near- to far-term evolution of UAM has been described in [5] by a study on the San Fransisco Bay Area, USA. Both [4], [5] simulate the passenger flight demand to perform their feasibility studies. A system-level model on the number of vehicles needed in the system to meet demand, the number of vehicles airborne at any given time, and the length of time vehicles may have to loiter before a landing pad has been developed in [6].

One of the operational challenges for eVTOLs is the scheduling of arrivals at vertiports since eVTOLs are battery constraint and, thus, flight time in the final approach is restricted. Moreover, pre-scheduling is not possible since flights are performed on-demand. This also requires scheduling arrivals in real-time and absorbing delays while airborne. For commercial aviation, a significant amount of research has addressed the problem of aircraft arrival sequencing and scheduling [7]–[9], with the objective, for instance, of minimising delay [10]–[13], cost or environmental impact [14], [15]. Such problems are constrained by, for instance, feasible landing time, time-based separation requirements, runway capacity [10], sequence position shift [16], airline preferences [17], [18]. Some of the frequently used methods to solve the aircraft arrival scheduling problem are position shifting [19], dynamic programming [18], [20], branch-and-bound [10], branch-and-price [12] and data-splitting [21], [22]. These methods are also combined with heuristics [23] or a rolling horizon algorithm [24], [25]. None of the models, however, are constrained to airport (e.g. gate) capacity or remaining fuel, while this should be considered when modelling eVTOL arrivals. Current research on the scheduling of eVTOL arrivals at a vertiport is, however, limited. In [1], [2] the arrival trajectory of eVTOLs is optimised for minimal energy consumption based on a given RTA for a multi-rotor and tandem-tilted wing eVTOL, the EHANG-184 and Airbus A^3 Vahana respectively. In [26] a study on airspace system demand is performed for a range of values that future separation requirements would need to take to support high-demand, high-tempo UAM operations. In [27] continuous eVTOL vehicle routing, departure and arrival scheduling for UAM is developed such that minimum separation is ensured and eVTOL traffic is integrated with existing air traffic.

An important constraint for eVTOLs is the current electric battery technology. No battery models for eVTOL vehicles are available, but research on battery predictions for electric winged aircraft [28], [29] and drones [30] has been performed. These models create a voltage and state of charge profile based on a flight plan using an Equivalent Circuit Model (ECM) to check if the plan can be fulfilled. Also, the ECM parameters are determined by flight testing a 33% scale model of the Zivko Edge 540T aircraft and one battery cell of the DJI Phantom 3 Standard drone, respectively. Complementary to existing research on eVTOLs traffic management, this research develops an arrival sequencing and scheduling model for UAM that minimises total delay while considering the battery status of each eVTOL and flying energy-optimal trajectories where possible.

III. MODELLING APPROACH

In this section, we describe our model for eVTOL arrivals at one vertiport. The model consists of 5 parts: i) the concept of eVTOL arrivals at a vertiport; ii) the flight dynamics model for an eVTOL equipped with one electric battery; iii) the electric battery prognostics model; iv) an optimisation model for eVTOL arrival sequencing and scheduling at a single or double landing vertiport and v) an eVTOL arrival demand model.

A. eVTOL Arrivals at A Vertiport - Concept of Operations

We consider eVTOLs arriving at one landing platform, i.e., a vertiport. Moreover, the eVTOLs operate in a segregated airspace volume. We assume a total cruise phase of 25 minutes and altitude $500m$ [31] with the final approach at a vertiport defined as follows. We also assume 2 arrival and 2 departure metering fixes at the vertiport [19] (see Fig. 1). These metering fixes have the purpose of separating climbing and descending traffic.

The arrival approach fixes are located at a radius of $400m$ away from the vertiport. A minimum time separation of $90s$ [13] is assumed for the eVTOLs arriving at the 2 approach fixes. Furthermore, their required altitude at the approach fix

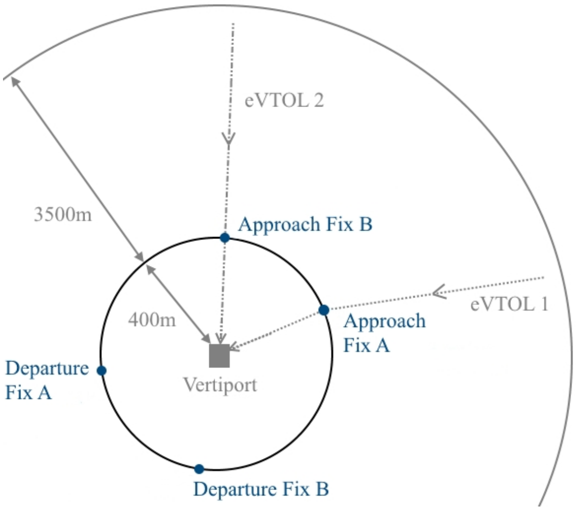

Fig. 1. eVTOL arrivals at a vertiport - concept of operations.

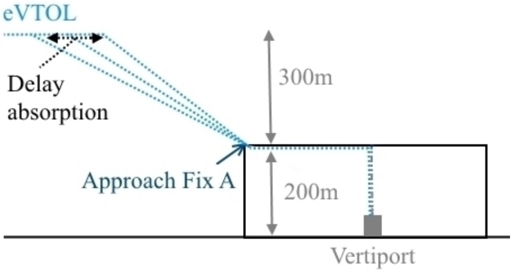

Fig. 2. eVTOL arrivals at a vertiport through approach fix A - side view.

is set to $200m$. This requirement is needed to ensure clearance from high rise buildings, as well as to provide sufficient space to absorb delay through shallow descent paths [1]. Between the approach fix and the vertiport, each eVTOL flies at a predefined speed and altitude profile (see Fig. 2), while maintaining a separation of $90s$ between consecutive arrivals. This last phase of the trajectory is a step-down approach, which is considered to be efficient in minimising delay [32] and beneficial for clearance from high rise buildings.

We assume that the arrival sequencing and scheduling of incoming eVTOLs is initiated at $3900m$ radius around the vertiport (see Fig. 1). This radius has been determined based on a trade-off between maximising shallow descent flights and minimising the duration of approach procedures. This proposed ConOps allows for the absorption of delay up to 6 minutes without applying holding or vectoring. If more delay needs to be absorbed during a demand peak, a hover period at the terminal area boundary or a second landing pad can be introduced.

The concept of operations of eVTOL arrivals at a double landing pad vertiport is similar to the single landing pad approach (see Fig. 3). A $135m$ horizontal approach and a vertical landing funnel connect the approach fix to the corresponding landing pad. The $530m$ separation between both funnels allows for independent arrivals at pad A and B.

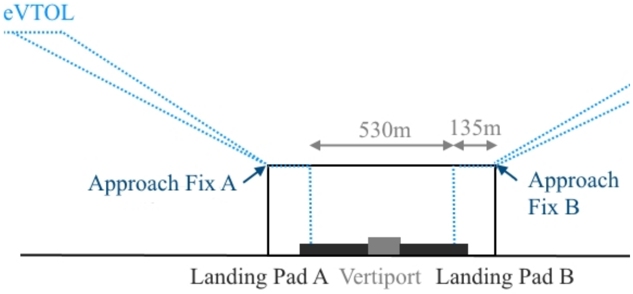

Fig. 3. eVTOL arrivals at a vertiport with double landing pad - side view.

B. eVTOL Flight Dynamics Model

We use the following flight dynamics model for the EHANG-184 multi-rotor eVTOL designed to transport a single passenger [31] and equipped with one electric battery [1].

$$P_r = P_i + P_a + P_c + P_f \tag{1}$$

$$= 4 \cdot T \cdot v_i + T \cdot V \cdot \sin\alpha + 0.2 \cdot P_r \tag{2}$$

$$V = \sqrt{V_x^2 + V_h^2} \tag{3}$$

$$\alpha = \theta + \gamma = \theta + \arctan\left(\frac{V_x}{V_h}\right) \tag{4}$$

$$v_h = \sqrt{\frac{T_r}{2\rho\pi R^2}} \tag{5}$$

$$v_i = \frac{v_h^2}{\sqrt{(V\cdot\cos(\alpha))^2 + (V\cdot\sin(\alpha)+v_i)^2}}, \tag{6}$$

where P_r, P_i, P_a, P_c, P_f are the required, induced, parasite, climb and profile power, respectively, with $P_f = 0.2P_r$ [33]. V is the true airspeed with the vertical component V_x and the horizontal component V_h. T, α, θ, γ are the thrust, the angle of attack, the pitch angle and flight path angle, respectively. v_i, v_h, R, T_r, ρ are the induced velocity, the induced velocity in hover, rotor radius, thrust per rotor and the air density, respectively. ρ is assumed to be equal to the international standard atmosphere density at sea level.

We further assume that all rotors produce equal thrust. Thus, we assume an upper and lower rotor to produce equal thrust [34], such that $T_r = \frac{1}{8}T$. The induced velocity v_i is computed using Momentum Theory and v_h, leading to Eq. (6). A fourth-degree polynomial arises when computing v_i, which is solved using the MATLAB Roots package [35].

C. Battery Prognostics Model

We consider the following model for the total electric power demand, P_d, [30], [36]:

$$P_d = SF \cdot \frac{1}{\eta_P}\frac{1}{\eta_e}P_r \tag{7}$$

where SF is the safety factor to account for weather conditions and emergency diversion, $SF = 1.5$, η_P is the rotor efficiency, $\eta_P = 0.7652$, η_e, is the mechanical efficiency, $\eta_e = 0.85$.

We further consider the following model for the battery State of Charge (SOC) demand during a mission between time t_0 and t_f [36]:

$$I(t_k) = \frac{P_d(t_k)}{V_n} \tag{8}$$

$$SOC(t_k) = \frac{I(t_k)\cdot(t_k - t_{k-1})}{3600\cdot Q}\cdot 100\% \tag{9}$$

$$SOC = \sum_{t_0}^{t_f} SOC(t_k) \tag{10}$$

where $I(t_k)$ is the total current of all battery cells during time step t_k, V_n is the nominal battery voltage, Q is the battery capacity. The battery is assumed to be empty if it reaches a 10% SOC to prevent it from deep discharge [37], [38].

D. eVTOL Arrival Sequencing and Scheduling Model for Single Landing Pad

Using the ConOps for eVTOL arrivals at a vertiport in Section III-A, the flight dynamics model for an eVTOL in Section III-B and the eVTOL battery model in Section III-C, we propose an optimal sequencing and scheduling algorithm for eVTOL arrivals at a vertiport (see Fig. 4).

Firstly, using the ConOps for eVTOL arrivals at a single landing pad (Section III-A) and the eVTOL flight dynamics (Section III-B), we determine the optimal flight trajectory with respect to energy consumption for a given RTA at the vertiport [1], [2]. The optimal trajectories are computed using the GPOPS-II software [39]. The rotorcraft equations of motion are continuous-time nonlinear differential equations, such that the trajectory optimisation problem is solved numerically using a pseudospectral method. This method transcribes a multi-phase optimal control problem to a large sparse nonlinear programming problem. The output of the GPOPS-II optimisation is the total energy required to fulfil the trajectory, the state variables (V_x, V_h, altitude and distance) and the control variables (T and θ).

Secondly, we use the GPOPS-II optimisation output to determine P_r at each instance of the flight trajectory (see Section III-B). Further, P_r is used to determine the battery power demand P_d and the SOC demand (see Section III-C). The latest possible RTA is now found for each arriving eVTOL based on its battery status.

Thirdly, we determine an eVTOL arrival sequence and schedule at a vertiport for minimal total arrival delay by Eq. (11 - 30). Eq. (11) shows the objective function for minimum total delay for all eVTOLs p in set G, where G is the set of all eVTOLs considered, c_e^p, c_l^p are the cost of eVTOL p being earlier and later than the expected time of arrival $ETA^p(i)$ at approach fix $i \in \{A, B\}$, respectively. Here, $ETA^p(i)$, $i \in \{A, B\}$, is obtained from the most energy-optimal trajectory and c_e^p, c_l^p from the power required to absorb the scheduled delay.

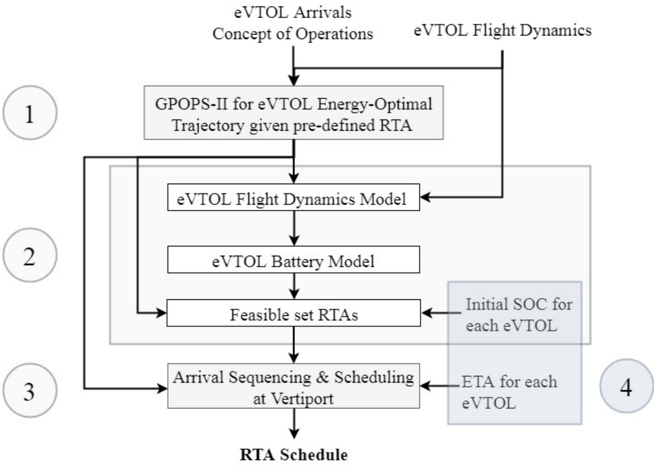

Fig. 4. eVTOL arrival sequencing and scheduling model overview.

We consider the decision binary variable $a^p \in \{0, 1\}$, where $a^p = 1$ means that eVTOL p uses approach fix A and $a^p = 0$ that eVTOL p uses approach fix B. Also, the decision variables Δt_e^p and Δt_l^p describe the time that eVTOL p arrives before and after $ETA^p(i)$, respectively, at the approach fix i, $i \in \{A, B\}$ from flying a less or more shallow descent. The delay resulting from the choice of arrival route $\Delta t_{l,i}^p$, $i \in \{A, B\}$, is calculated by (12) and (13) in which T_t^p is the transfer time of flight between the approach fix and vertiport and penalised by cost $c_{l,af}^p$.

Objective function

$$\min \qquad \sum_{p \in G} c_e^p \cdot \Delta t_e^p + c_l^p \cdot \Delta t_l^p + c_{l,af}^p \cdot a^p \cdot (\Delta t_{l,A}^p - \Delta t_{l,B}^p) \tag{11}$$

$$\Delta t_{l,A}^p = \max\left(0, (ETA^p(A) + T_t^p(A) - ETA^p(B) - T_t^p(B)\right)) \tag{12}$$

$$\Delta t_{l,B}^p = \max\left(0, (ETA^p(B) + T_t^p(B) - ETA^p(A) - T_t^p(A)\right)) \tag{13}$$

Constraints

$$s^{pq} = \{0, 1\} \qquad \forall p \in G, q \in \ [p - K, p + K], p \neq q \tag{14}$$

$$z^{pq}, a^p = \{0, 1\} \qquad \forall p, q \in G \tag{15}$$

$$\Delta t_e^p, \Delta t_l^p \geq 0 \qquad \forall p, q \in G \tag{16}$$

$$s^{pq} + s^{qp} = 1 \qquad \forall p, q \in G \tag{17}$$

$$z^{pq} = z^{qp} \qquad \forall p, q \in G \tag{18}$$

$$z^{pq} \geq a^p + a^q - 1 \qquad \forall p, q \in G, p \neq q \tag{19}$$

$$z^{pq} \geq -a^p - a^q + 1 \qquad \forall p, q \in G, p \neq q \tag{20}$$

$$z^{pq} \leq \frac{1}{2} a^p - \frac{1}{2} a^q + 1 \qquad \forall p, q \in G, p \neq q \tag{21}$$

$$z^{pq} \leq -\frac{1}{2} a^p + \frac{1}{2} a^q + 1 \qquad \forall p, q \in G, p \neq q \tag{22}$$

$$RTA_e^p \leq RTA^p \leq RTA_l^p \qquad \forall p \in G \tag{23}$$

$$RTA^p \geq RTA^q + \Delta t_{sep}^{qp} - M^{pq} \cdot s^{pq} \tag{24}$$

$$RTA^p(A) \geq RTA^q(A) + \Delta t_{sep}^{qp} \cdot z^{qp} - M^{pq} \cdot s^{pq} \tag{25}$$

$$RTA^p(B) \geq RTA^q(B) + \Delta t_{sep}^{qp} \cdot z^{qp} - M^{pq} \cdot s^{pq} \tag{26}$$

$$\forall p, q \in G, p \neq q$$

in which

$$M^{pq} = RTA_l^q + \Delta t_{sep}^{qp} - RTA_e^p \tag{27}$$

$$RTA^p = a^p \cdot (RTA^p(A) + T_t^p(A)) + (1 - a^p) \cdot (RTA^p(B) + T_t^p(B)) \tag{28}$$

$$RTA^p(A) = ETA^p(A) + \Delta t_l^p - \Delta t_e^p \tag{29}$$

$$RTA^p(B) = ETA^p(B) + \Delta t_l^p - \Delta t_e^p \tag{30}$$

Eq. (14) defines $s^{pq} = 1$ if eVTOL p arrives prior to eVTOL q and $s^{pq} = 0$ otherwise for the parameters inside the Constrained Position Shifting (CPS) window. The CPS limits the number of positions K an eVTOL can deviate from the first-come-first-serve landing sequence. Eq. (15) and (16) define $z^{pq} = 1$ if eVTOL p and q fly through the same approach fix and $z^{pq} = 0$ otherwise and constrain the decision variables seen in Eq. 11. Constraint (17) ensures that either eVTOL p follows eVTOL q or eVTOL q follows eVTOL p. Eq. (18) ensures that if eVTOL p and q go through the same approach fix, the reverse is also true. Eq. (19) and (20) further define $z^{pq} = 1$ if both eVTOL p and q use approach fix A and B, respectively. Eq. (21) and (22) define $z^{pq} = 0$ if eVTOLs p and q fly through different approach fixes. The time window available for landing at the vertiport is described in (23). The earliest possible time of arrival RTA_e^p is derived from the flight performance model (see Section III-B), while the latest RTA_l^p results from the battery model (see Section III-C). Eq. (24-26) ensure a time-based separation of at least Δt_{sep}^{qp} if p follows q at the vertiport and the approach fixes. Lastly, Eq. (27-30) show the calculation for the Big-M method and define the RTA for eVTOL p at the vertiport or approach fix A and B, respectively.

Column Generation for Hover

If necessary, eVTOLs with sufficient remaining battery SOC can also absorb delay in hover at the terminal area boundary. We extend the eVTOL arrival sequencing and scheduling model in Eq. (11 - 30) with decision variable $\Delta t_{l,h}^p$ for delay absorbed in hover using a column generation algorithm. The objective function in Eq. (11) is extended with the cost to hover by $c_{l,h}^p \cdot \Delta t_{l,h}^p$. Big-M parameter M^{pq} in Eq. (27) is increased with the maximum possible time in hover $\Delta t_{l,h,max}^p$, depending on remaining battery SOC. $\Delta t_{l,h}^p$ is added to the RTA^p, $RTA^p(A)$ and $RTA^P(B)$ in Eq. (28 - 30). This is also demonstrated in the eVTOL arrival sequencing and scheduling for a double landing pad in Eq. (34 - 52).

Rolling Horizon Algorithm

The rolling horizon algorithm is applied to increase the computational efficiency of the eVTOL arrival sequencing and scheduling model by cutting the problem into smaller planning horizons. The solver uses a planning period of 15 minutes and a planning horizon of two planning periods. The resulting arrival sequence and schedule is frozen for the eVTOLs in the first period and the RTA of the last frozen eVTOL approach through each approach fix $RTA_{last}(i)$, $i \in \{A, B\}$ is saved. To ensure separation between eVTOL p approaching in the new planning horizon and the eVTOLs in the frozen horizon, the input for the RTA window constraint in Eq. (23) is adapted according to Eq. (31 - 33).

$$RTA_e^p(A) = \max\left(RTA_{last}(A) + \Delta t_{sep}^{pq}, RTA_e^p(A)\right) \quad (31)$$

$$RTA_e^p(B) = \max\left(RTA_{last}(B) + \Delta t_{sep}^{pq}, RTA_e^p(B)\right) \quad (32)$$

$$RTA_e^p = \min\left(RTA_e^p(A) + T_t^p(A), RTA_e^p(B) + T_t^p(B)\right) \quad (33)$$

E. eVTOL Arrival Sequencing and Scheduling Model for Double Landing Pad with Hover

We extend the eVTOL arrival sequencing and scheduling model from Section III-D for the double landing pad ConOps (Section III-A). Again, the flight dynamics model for an eVTOL in Section III-B and the eVTOL battery model in Section III-C are used (see Fig. 4). The changes required to allow for the implementation of hover and the double landing pad ConOps are depicted and highlighted in Eq. (34 - 52). In Eq. (34), $\Delta t_{l,i}^p$, $i \in \{A, B\}$ is calculated by (12) and (13) where T_t^p is adapted for the double landing pad ConOps.

The RTA_e^p in Eq. (44) is altered according to Eq. (48). Here, $RTA_{e,lp}^p(i)$ is the earliest possible landing time of eVTOL p arriving through approach fix i and thus at landing pad i, $i \in \{A, B\}$. This is also incorporated in the Big-M parameter in Eq. (49). Eq. (45) separates eVTOLs arriving at the same landing pad.

Objective function

$$\begin{aligned} \min \quad & \sum_{p \in G} c_e^p \cdot \Delta t_e^p + c_l^p \cdot \Delta t_l^p + c_{l,h}^p \cdot \Delta t_{l,h}^p \\ & + c_{l,af}^p \cdot a^p \cdot (\Delta t_{l,A}^p - \Delta t_{l,B}^p) \end{aligned} \quad (34)$$

Constraints

$$s^{pq} = \{0, 1\} \qquad \forall p \in G, q \in [p-K, p+K], p \neq q \quad (35)$$

$$z^{pq}, a^p = \{0, 1\} \qquad \forall p, q \in G \quad (36)$$

$$\Delta t_e^p, \Delta t_l^p, \Delta t_{l,h}^p \geq 0 \qquad \forall p, q \in G \quad (37)$$

$$s^{pq} + s^{qp} = 1 \qquad \forall p, q \in G \quad (38)$$

$$z^{pq} = z^{qp} \qquad \forall p, q \in G \quad (39)$$

$$z^{pq} \geq a^p + a^q - 1 \qquad \forall p, q \in G, p \neq q \quad (40)$$

$$z^{pq} \geq -a^p - a^q + 1 \qquad \forall p, q \in G, p \neq q \quad (41)$$

$$z^{pq} \leq \frac{1}{2}a^p - \frac{1}{2}a^q + 1 \qquad \forall p, q \in G, p \neq q \quad (42)$$

$$z^{pq} \leq -\frac{1}{2}a^p + \frac{1}{2}a^q + 1 \qquad \forall p, q \in G, p \neq q \quad (43)$$

$$RTA_e^p \leq RTA^p \leq RTA_l^p \qquad \forall p \in G \quad (44)$$

$$RTA^p \geq RTA^q + \Delta t_{sep}^{qp} \cdot z^{qp} - M^{pq} \cdot s^{pq} \quad (45)$$

$$RTA^p(A) \geq RTA^q(A) + \Delta t_{sep}^{qp} \cdot z^{qp} - M^{pq} \cdot s^{pq} \quad (46)$$

$$RTA^p(B) \geq RTA^q(B) + \Delta t_{sep}^{qp} \cdot z^{qp} - M^{pq} \cdot s^{pq} \quad (47)$$

$$\forall p, q \in G, p \neq q$$

in which

$$RTA_e^p = a^p \cdot RTA_{e,lp}^p(A) + (1 - a^p) \cdot RTA_{e,lp}^p(B) \quad (48)$$

$$\begin{aligned} M^{pq} = {} & RTA_l^q + \Delta t_{l,h,max}^p + \Delta t_{sep}^{qp} \\ & - \min\left(RTA_{e,lp}^p(A), RTA_{e,lp}^p(B)\right) \end{aligned} \quad (49)$$

$$\begin{aligned} RTA^p = {} & a^p \cdot (RTA^p(A) + T_t^p(A)) + \\ & (1 - a^p) \cdot (RTA^p(B) + T_t^p(B)) \end{aligned} \quad (50)$$

$$RTA^p(A) = ETA^p(A) + \Delta t_l^p - \Delta t_e^p + \Delta t_{l,h}^p \quad (51)$$

$$RTA^p(B) = ETA^p(B) + \Delta t_l^p - \Delta t_e^p + \Delta t_{l,h}^p \quad (52)$$

Rolling Horizon Algorithm

We also apply the rolling horizon algorithm (Section III-D) to the eVTOL arrival sequencing and scheduling model for double landing pad with hover. The RTA_e^p in Eq. (48) is now computed using $RTA_{e,lp}^p(A)$ and $RTA_{e,lp}^p(B)$ from Eq. (53) and (54), respectively. Here, $RTA_{last,lp}(i)$ is the RTA of the last frozen eVTOL arrival at landing pad i, $i \in \{A, B\}$.

$$\begin{aligned} RTA_{e,lp}^p(A) = \max\big(&RTA_{last,lp}(A) + \Delta t_{sep}^{pq}, \\ &RTA_e^p(A) + T_t^p(A)\big) \end{aligned} \quad (53)$$

$$\begin{aligned} RTA_{e,lp}^p(B) = \max\big(&RTA_{last,lp}(B) + \Delta t_{sep}^{pq}, \\ &RTA_e^p(B) + T_t^p(B)\big) \end{aligned} \quad (54)$$

F. eVTOL Arrival Demand Model

An eVTOL arrival demand model is used to simulate the battery SOC and ETA of each arrival p (see Fig. 4). The expected eVTOL arrival demand distribution over a day is based on a case study for a hexagonal vertiport network in Houston, TX, USA [6]. The distribution consists of the sum of three normal distributions: two commuter rush hour peaks at 8AM and 4PM ($N(8, 2)$ and $N(16, 2)$) and one day peak at noon ($N(12, 6)$). The curve is normalised to a cumulative distribution of 1 and scaled by $M_4 = 8500$ to obtain a realistic demand. The hub vertiport in the hexagon center is expected to receive a double arrival demand.

An eVTOL arrival $A(t_k)$ for each time step $t_k = 10s$ is simulated if a uniform random number generation ($u \sim U(0, 1)$) is lower than or equal to the demand probability. The total number of arrivals between t_{start} and t_{end} are used to find the expected eVTOL arrival rate per hour $\lambda(t)$ in Eq. (55).

The expected time of arrival $ETA^p(i)$ of eVTOL p at approach fix i, $i \in \{A, B\}$, is modelled as an inhomogeneous Poisson process in Eq. (56) and (57). Here, S is an exponential random variable based on $\lambda(t)$. $\Delta t_{l,i}^p$, $i \in \{A, B\}$ is computed from the origin of eVTOL p in the hexagonal vertiport network layout [6] with a radius of $20km$. Arrivals from each origin v at the hub are equally likely to occur such that $P_v = \frac{1}{6}$.

$$\lambda(t_{start}, t_{end}) = \frac{1}{t_{end} - t_{start}} \cdot \sum_{t_{start}}^{t_{end}} A(t_k) \quad (55)$$

$$ETA^p = ETA^{p-1} + S \qquad S \sim exp\left(\lambda(t)\right) \quad (56)$$

$$ETA^p(i) = ETA^p - T_t^p(i) + \Delta t_{l,i}^p \quad (57)$$

The initial SOC of eVTOL p is modelled as a normal distribution with mean 30% and variance of 5% ($N(30, 5)$).

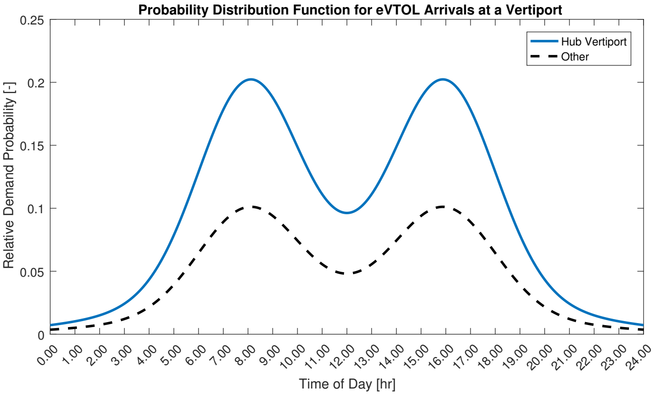

Fig. 5. Demand probability distribution function for eVTOL arrivals in Houston, TX, USA.

IV. RESULTS FOR EHANG-184 EVTOL

We demonstrate the working of the eVTOL arrival sequencing and scheduling model for a single landing pad ConOps from Section III with a study on the EHANG-184, a multi-rotor, single-passenger eVTOL [31].

Fig. 6 shows the results from the first step in the algorithm, the GPOPS-II energy-efficient trajectory optimisation for a trivial selection of RTAs. An RTA$= 165s$ at the approach fix (AF) is the lowest input to ensure convergence to a solution. The cruise flight phase is performed at $500m$ altitude and $27.8m/s$ cruise speed. The eVTOL arrival scheduling and sequencing is initiated at $3900m$ distance from the vertiport (see Section III-A). Based on the results of this optimisation, the eVTOL control system initiates a shallow descent between $3400m$ and $1000m$ from the vertiport at a constant $V_x = 5.9m/s$ and variable V_h. After passing the AF, a horizontal flight phase is executed at cruise speed and a vertical flight at $2.9m/s$. Fig. 6 also shows the feasible landing time window as input for the scheduling tool. For an RTA at the AF between $165s$ and $525s$ and a single landing pad concept, the eVTOL is required to arrive at the vertiport between $307s$ and $667s$ as the flight time between the AF and vertiport $T_t = 142s$. In an

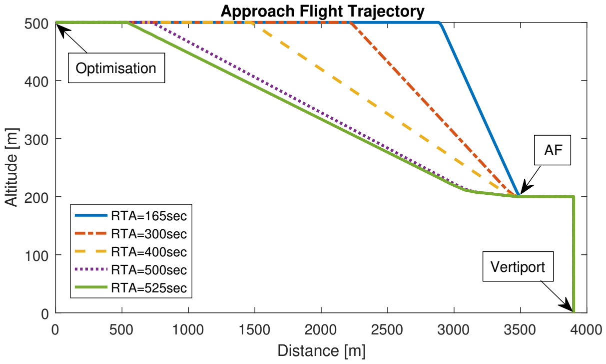

Fig. 6. EHANG-184 energy-optimal trajectory to single landing pad for different RTA to approach fix.

approach to a double landing pad, $T_t = 97s$. A trajectory with RTA$= 165s$, which also corresponds to the minimum energy required, is used as a baseline trajectory to determine the ETA as input for the scheduling model.

The SOC required to perform each of the trajectories shown in Fig. 7 is computed during the second step of the model (see Fig. 4). The battery characteristics specific to EHANG-184 are not made public so it is assumed that Q is $5000Ahr$ and V_n is $12V$. When the remaining SOC of an incoming eVTOL is equal to e.g. 25%, Fig. 7 indicates RTA$= 434s$ at the AF, thus an RTA at the vertiport of $576s$ can be scheduled at the latest.

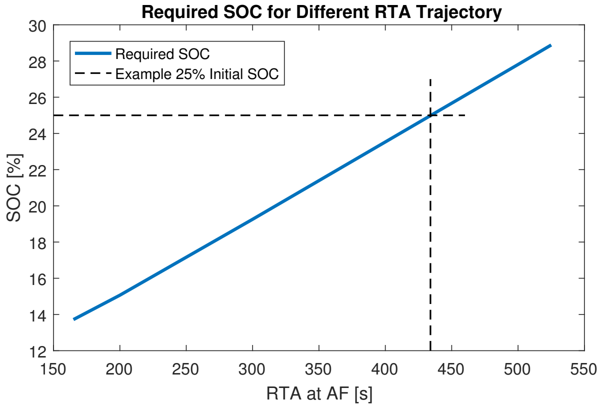

Fig. 7. SOC required to perform different delay absorption trajectories with example 25% SOC and resulting latest RTA of $434s$.

The eVTOL sequence and schedule are now obtained using the model in step 3 (see Fig. 4). An example of input for our model is shown in Tab. I. We also assume $K = 2$ [16], $c_e = 10$ and $c_l = 30$ [11]. Tab. II presents the results when using a single landing pad ConOps. The values for Δt_l^p represent the delay to be absorbed by flying shallow descent, while $\Delta t_{l,AF}^p$ is the delay due to flying through the furthest approach fix (AF). Tab. II shows that the eVTOLs are rescheduled and sequenced when this minimises delay or when an eVTOL has a low SOC (Flight 8 and 9). Furthermore, eVTOLs are delayed if the separation requirements are not satisfied (Flight 8 and 10). It also selects the AF, which is a means to separate eVTOLs and absorb delay (Flight 3 and 4). These results indicate the proof of concept of the model formulation.

TABLE I
TEST DATASET OF 10 EHANG-184 EVTOLS.

Flight Nr. [-]	**ETA (A)** [s]	**ETA (B)** [s]	**Initial SOC [%]**
1	165	180	13
2	250	250	18
3	335	325	25
4	420	410	30
5	505	505	18
6	590	590	13
7	665	675	25
8	750	760	25
9	855	845	14
10	930	930	28

TABLE II
ARRIVAL SEQUENCE AND SCHEDULE FOR TEST DATASET.

Flight Nr [-]	**RTA [s]**	Δt_l^p [s]	**AF [-]**	$\Delta t_{l,AF}^p$ [s]
1	307	0	A	0
2	397	5	B	0
3	487	20	A	10
4	577	25	A	10
5	667	20	A	0
6	757	25	A	0
7	847	40	A	0
9	987	0	B	0
8	1077	185	A	0
10	1167	95	B	0

The computational time required to obtain the described results without rolling horizon solver is 2 seconds, using CPLEX LP Solver [40] extension of MATLAB [35] on a computer with Intel CORE i7 processor.

V. CASE STUDY ON EVTOL ARRIVALS IN HOUSTON

We validate the eVTOL arrival sequencing and scheduling model including rolling horizon solver (Section III-D and III-E) with the eVTOL arrival demand model for a hub vertiport in Houston, TX, USA (Section III-F). We use the input as described in Section IV and the cost function presented in Tab. III found from the power required for each delay absorption strategy.

TABLE III
COST FUNCTION FOR DELAY WITH EHANG-184 EVTOL

Cost Function	c_e^p **[-]**	c_l^p **[-]**	$c_{l,af}^p$ **[-]**	$c_{l,h}^p$ **[-]**
Value	$\emptyset$	28	36	42

We perform a Monte Carlo simulation to find the expected arrivals, hovers and delays during a peak (7.30-8.30) and off-peak (11.30-12.30) slot. The single pad model finds 1227 feasible schedules from 2000 arrival demand generations during off-peak and none during peak. The double landing pad model finds 100 and 90 feasible schedules from 100 arrival demand generations during off-peak and peak, respectively. The expectations are presented for the time of the day in Tab. V and for each eVTOL in Tab. VI.

It is recognised in Tab. V that twice as many eVTOL arrivals are expected during peak as during off-peak hours which follows Fig. 5. Besides, using one extra landing pad results in 1) the ability to host a double amount of eVTOL arrivals for a similar total delay and 2) an 85% reduction of the expected total delay for the same amount of eVTOL arrivals. Independent of the time of the day, a double pad ConOps performs better on average delay and has lower maximum delay outliers. It shows a 19% probability that one or two eVTOLs are scheduled to hover only in a single pad ConOps, leading to a 1% chance of a scheduled delay larger than 6 minutes (see Tab. VI).

Tab. VI proofs that the scheduled delay is higher for increasing number of arrivals and decreasing number of landing pads. Where delay larger than 6 minutes can occur for eVTOLs arriving at a single landing pad during off-peak, the scheduled eVTOL delay is likely to stay within 1 minute (94%) or 3 minutes (96%) when arriving at a double landing pad during peak or off-peak, respectively.

We also perform one generation of daily eVTOL arrivals (see Fig. 8). Fig. 8 again represents the stochastic arrival of eVTOLs according to the arrival demand forecast from Fig. 5. The delay propagation over this day is analysed for the baseline $\Delta t_{sep} = 90s$ and for a selection of $\Delta t_{sep} = 60s$, $80s$, $100s$ in Fig. 9 and 10.

The baseline result in Fig. 9 depicts that most delay is scheduled during the rush hour peaks around 8.00 and 16.00 o'clock, due to a higher amount of eVTOL arrivals. An increase in eVTOL arrivals per hour from 50 to 70 shows to triple the hourly total delay. This suggests that the maximum hourly arrival capacity is reached around 60 eVTOLs/hr. Furthermore, the daily delay increases with higher Δt_{sep}. More specifically, expanding the separation between eVTOLs from $80s$ to $100s$, the cumulative delay is more than doubled. Therefore, designing eVTOLs for low time separation requirements is highly beneficial to on-time operations and thus to the feasibility of on-demand urban air mobility.

Fig. 10 presents similar behaviour for the hourly maximum delay for $\Delta t_{sep} = 90s$. However, the maximum delay between 8.00 and 9.00 (175s) and between 15.00 and 16.00 (309s) differs significantly while they both host around 70 eVTOL arrivals. This indicates that the maximum delay also depends on the spread of the arrivals, thus the ETAs, over the hour. Fig. 10 also shows that the maximum delay per hour is negatively influenced by increasing the time separation requirements as expected. The highest maximum delay is however observed for Δt_{sep} = 90s. This results from optimising for a minimum total delay, such that a sequence swap and thus absorption of high delay by one eVTOL can be more beneficial than or identical to spreading delay over multiple eVTOLs.

The sensitivity of the eVTOL arrival sequencing and scheduling model is also examined for K in constrained position shifting and the duration of the planning period in the rolling horizon (RH) algorithm. Both did not have a large influence on the delay results but showed to impact the computational time (see Tab. IV). A higher amount of decision variables or an increased challenge to solve the problem explain the reduced computational efficiency compared to the highlighted baseline. Because eVTOLs are envisioned to fly on-demand, only data sets up to 40 eVTOLs are expected which can be solved real-time using the rolling horizon solver. At last, the mean of the initial battery SOC distribution is varied. The SOC input showed to mainly impact the distribution of the delay over the eVTOLs, where the computational time and cumulative delay were not significantly impacted.

TABLE IV
COMPUTATIONAL TIME TO SOLVE THE eVTOL ARRIVAL SEQUENCE AND SCHEDULE FOR ONE DAY

K [-]	**1**	**2**	**2**	**2**	**3**
RH [min]	**15**	**10**	**15**	**20**	**15**
Comp. Time [s]	20501	10813	18477	36495	22127

VI. CONCLUSION AND RECOMMENDATIONS

A sequencing and scheduling algorithm with a route selection function for on-demand eVTOL arrivals in UAM is proposed in this paper. The problem is formulated as a mixed integer linear program whose objective is to minimise the total arrival delay. The problem formulation includes constraints such as minimum time separation, eVTOL battery energy, and vehicle dynamics. We compute the optimal required times of arrival (RTAs) for eVTOLs arriving at a vertiport within a given planning horizon. Numerical experiments show that our proposed algorithm has near real-time computational performance when scheduling the arrival of up to 40 eVTOLs. Our proposed algorithm and ConOps for terminal airspace design provide a potential solution framework to support safe and efficient on-demand arrivals in Urban Air Mobility (UAM).

The contribution of this paper is threefold. Firstly, we propose a ConOps for the airspace design and configuration of a vertiport with a single or double landing pad. We introduce multiple arrival routes with multiple arrival metering fixes. Secondly, this is the first research work on eVTOL arrival sequencing and scheduling for on-demand UAM. The algorithm has arrival route selection capability. It includes a battery discharge prediction model that makes this arrival scheduling algorithm specially designed for eVTOL operations. It outputs landing time slots (or RTAs) for all arriving eVTOLs for minimum total delay. Thirdly, the expected delay is generated for a hub in a hexagonal vertiport network in Houston, TX, USA using this ConOps and eVTOL arrival sequencing and scheduling model. This algorithm and the delay forecasts can be used as a baseline for future research on optimal UAM arrival scheduling and airspace design.

Future work includes a more in-depth research on the airspace design, both for arrival and departure procedures, as well as safe separation from other aviation traffic in the integrated airspace. Detailed battery testing and modelling are recommended to provide a more accurate model for battery discharge prediction. Research on the eVTOL separation requirement is advised to prevent unsafe operations and redundant scheduled arrival delay. Finally, this arrival sequencing and scheduling algorithm should be incorporated with departure scheduling and conflict detection and resolution models to reach the highest efficiency in UAM and ensure safe flight operations.

ACKNOWLEDGEMENT

The authors would like to thank Guodong Zhu for his support throughout the project and Priyank Pradeep for his assistance and the use of the GPOPS-II trajectory optimisation tool.

TABLE V
HOURLY EXPECTATIONS FOR EVTOLS ARRIVING AT A SINGLE OR DOUBLE LANDING PAD AT 7.30-8.30 (PEAK) AND 11.30-12.30 (OFF-PEAK)

	Double Pad, Peak		**Double Pad, Off-Peak**		**Single Pad, Off-Peak**	
	Mean μ	**St. Dev. σ**	**Mean μ**	**St. Dev. σ**	**Mean μ**	**St. Dev. σ**
Hourly Arrivals [-]	73	8	36	6	33	5
Hourly Hovers [-]	0	0	0	0	0.19	0.59
Average Delay [s]	37	22	9	7	66	36
Max Delay [s]	189	67	74	45	274	98
Total Delay [s]	2776	1858	356	299	2260	1388

TABLE VI
DELAY EXPECTATIONS PER EVTOL ARRIVING AT A SINGLE OR DOUBLE LANDING PAD AT 7.30-8.30 (PEAK) AND 11.30-12.30 (OFF-PEAK)

Scheduled Delay per eVTOL	**Double Pad, Peak Probability [-]**	**Double Pad, Off-Peak Probability [-]**	**Single Pad, Off-Peak Probability [-]**
$\Delta t_l < 30\ s$	0.55	0.86	0.42
$\Delta t_l < 1$ min	0.72	0.94	0.56
$\Delta t_l < 2$ min	0.88	1.00	0.74
$\Delta t_l < 3$ min	0.96	1.00	0.85
$\Delta t_l < 4$ min	0.98	1.00	0.91
$\Delta t_l < 5$ min	1.00	1.00	0.96
$\Delta t_l < 6$ min	1.00	1.00	0.99
$\Delta t_{l,h} < 0\ s$	0	0	0.01

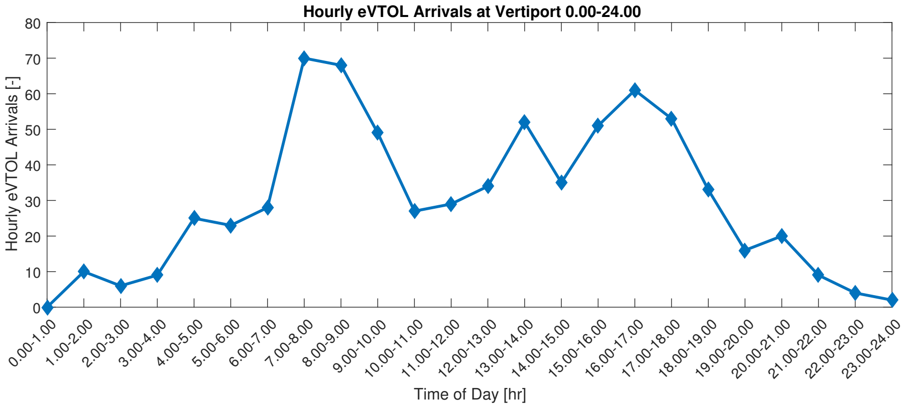

Fig. 8. Hourly eVTOL arrivals at the hub of a hexagonal vertiport network in Houston, TX, USA.

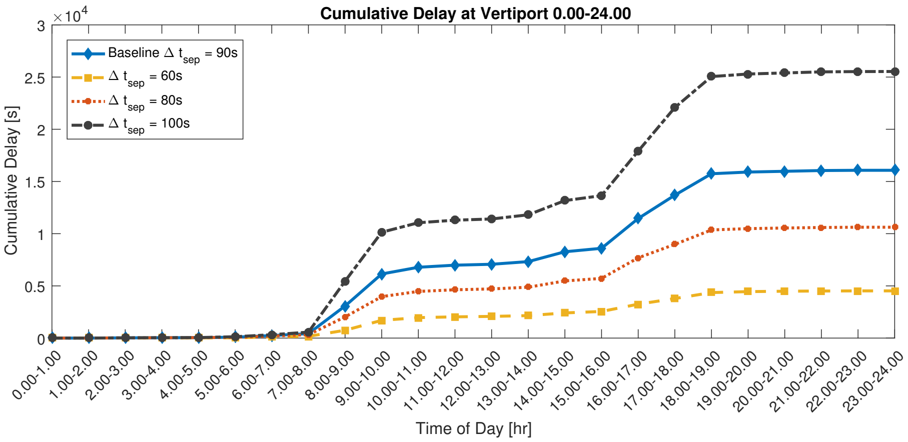

Fig. 9. Cumulative delay at a vertiport with double landing pad for one day for selection of time separation requirements.

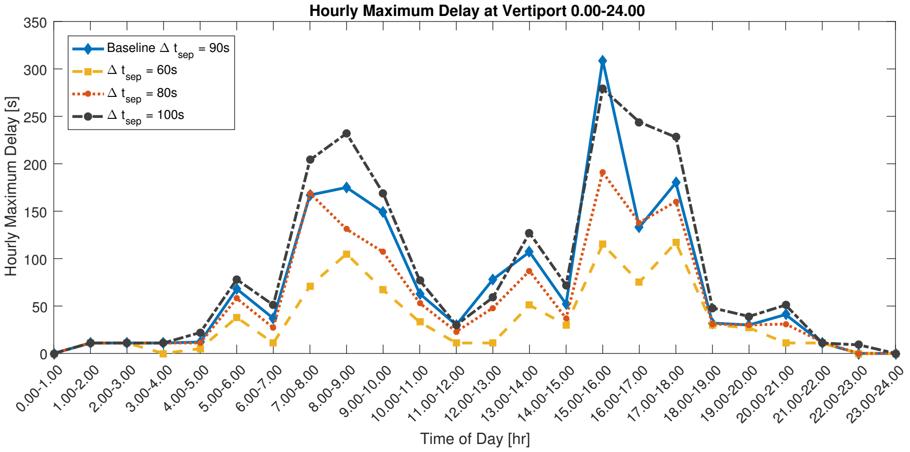

Fig. 10. Hourly maximum delay at a vertiport with double landing pad over one day for selection of time separation requirements.

REFERENCES

[1] P. Pradeep and P. Wei. Energy efficient arrival with RTA constraint for urban eVTOL operations. In *Proceedings of 2018 AIAA Aerospace Sciences Meeting*, pages 1–13, 2018.

[2] P. Pradeep and P. Wei. Energy optimal speed profile for arrival of tandem tilt-wing eVTOL aircraft with RTA constraint. In *Accepted by 2018 IEEE CSAA Guidance, Navigation and Control Conference*, pages 1–6, 2018.

[3] Uber Elevate. Fast-forwarding to a future of on-demand urban air transportation. Technical report, Uber Elevate Whitepaper, 2016.

[4] P. Vascik and J. Hansman. Constraint identification in on-demand mobility for aviation through an exploratory case study of Los Angeles. In *Proceedings of 17th AIAA Aviation Technology, Integration, and Operations Conference*, pages 1–25, 2017.

[5] J.J. Alonso, H.M. Arneson, J.E. Melton, M. Vegh, C. Walker, and L.A. Young. System-of-systems considerations in the notional development of a metropolitan aerial transportation system. Technical report, Stanford University and NASA Ames Research Center, 2017.

[6] L.W. Kohlman and M.D. Patterson. System-level urban air mobility transportation modeling and determination of energy-related constraints. In *Proceedings of 2018 Aviation Technology, Integration, and Operations Conference*, page 3677, 2018.

[7] P. Belobaba, A. Odoni, and C. Barnhart. *The Global Airline Industry*. John Wiley & Sons, 2009.

[8] R. de Neufville and A.R. Odoni. *Airport Systems: Planning, Design and Management*. McGraw-Hill Education LLC, 2^{nd} edition, 2003.

[9] C. Potts and J. Benell. A review of airport runway optimization. Technical report, School of Management, University of Southampton, UK supported by EUROCONTROL, 2009.

[10] J.E. Beasley, M. Krishnamoorthy, Y.M. Sharaiha, and D. Abramson. Scheduling aircraft landings - the static case. *Transportation Science*, 34(2):180–197, 2000.

[11] C. Gurert, C. Prins, and M. Sevaux. *Applications of optimization with XPress-MP*. Dash Optimization Ltd., 2000.

[12] M. Wen. Algorithms of scheduling aircraft landing problem. Technical report, Technical University of Denmark, 2005.

[13] A. Pawelek, P. Lichota, R. Dalmau, and X. Prats. Arrival traffic synchronisation with required time of arrivals for fuel-efficient trajectory. In *Proceedings of the 17th ATIO-AIAA Aviation Technology, Integration, and Operations Conference*, pages 1–14, 2017.

[14] I. Anagnostakis, J.P. Clarke, D. Bhme, and U. Vlckers. Runway operations planning and control: Sequencing and scheduling. *Journal of Aircraft*, 38(6):988–996, 2001.

[15] G. Slveling, S. Solak, J.P. Clarke, and E.L. Johnson. Scheduling of runway operations for reduced environmental impact. *Transportation Research Part D: Transport and Environment*, 16(2):110 – 120, 2011.

[16] A. Rodriguez-Diaz, B. Adenso-Diaz, and P.L. Gonzalez-Torre. Minimizing deviation from scheduled times in a single mixed operation runway. *Computer Operations Research*, 78:193–202, 2017.

[17] G. C. Carr, H. Erzberger, and F. Neuman. Fast-time study of airline-influenced arrival sequencing and scheduling. *Journal of Guidance, Control, and Dynamics*, 23(3):526–531, 2000.

[18] B. Chandran and H. Balakrishnan. A dynamic programming algorithm for robust runway scheduling. In *Proceedings of 2007 American Control Conference*, pages 1161–1166, July 2007.

[19] H. Erzberger and E. Itoh. Design principles and algorithms for air traffic arrival scheduling. Technical report, NASA Ames Research Center, California, USA and Electronic Navigation Research Institute, Tokyo, Japan, 2014.

[20] G. De Maere, J.A.D. Atkin, and E.K. Burke. Pruning rules for optimal runway sequencing. *Transportation Science*, pages 1–19, 2017.

[21] R. Prakash and J. Desai. A data-splitting algorithm for flight sequencing and scheduling on two runways. In *Proceedings of IIE Annual Conference*, pages 764–769, 2017.

[22] J. Desai and R. Prakash. Flight sequencing and scheduling: A data-driven approach. In *Proceedings of Industrial and Systems Engineering Research Conference*, pages 764–769, 2016.

[23] J.E. Beasley, J. Sonander, and P. Havelock. Scheduling aircraft landings at London Heathrow using a population heuristic. *Journal of the Operational Research Society*, 52(5):483–493, 2001.

[24] D'Ariano A. Sam, M. and D. Pacciarelli. Optimal aircraft traffic flow management at a terminal control area during disturbances. *Procedia - Social and Behavioral Sciences*, 54(1):460–469, 2014.

[25] X.B. Hu and W.H. Chen. Genetic algorithm based on receding horizon control for arrival sequencing and scheduling. *Engineering Applications of Artificial Intelligence*, 18(5):633–642, 2005.

[26] K.H. Goodrich and B. Barmore. Exploratory analysis of the airspace throughput and sensitivities of an urban air mobility system. In *Proceedings of 2018 Aviation Technology, Integration, and Operations Conference*, page 3364, 2018.

[27] C. Bosson and T.A. Lauderdale. Simulation evaluations of an autonomous urban air mobility network management and separation service. In *Proceedings of 2018 Aviation Technology, Integration, and Operations Conference*, page 3365, 2018.

[28] G. Cuong Chi, B. Bole, E. Hogge, S. Vazquez, M. Daigle, J. Celaya, A. Weber, and K. Goebel. Battery charge depletion prediction on an electric aircraft. In *Proceedings of Annual Conference of the Prognostics and Health Management Society 2013*, pages 1–11, 2013.

[29] B. Bole, M. Daigle, and G. Gorospe. Online prediction of battery discharge and estimation of parasitic loads for an electric aircraft. *ESC*, 2:5S2P, 2014.

[30] A.H. Alnaqeb, Y. Li, Y. Lui, P. Pradeep, J. Wallin, C. Hu, S. Hu, and P. Wei. Online prediction of battery discharge and flight mission assessment for electrical rotorcraft. In *Proceedings of 2018 AIAA Aerospace Sciences Meeting*, page 2005, 2018.

[31] EHANG184. EHANG184 autonomous aerial vehicle specs. http://www.ehang.com/ehang184/specs/. Accessed 05-March-2018.

[32] Y. Cao, T. Kotegawa, D. Sun, D. DeLaurentis, and J. Post. Evaluation of continuous descent approach as a standard terminal airspace operation. In *Proceedings of 9th USA/Europe Air Traffic Management R&D Seminar*, 2011.

[33] W. Johnson. *Rotorcraft Aeromechanics*. Cambridge University Press, 2013.

[34] W. Johnson. *Helicopter Theory*. Courier Corporation, 2012.

[35] The MathWorks. MATLAB and Statistics Toolbox Release 2016a. https://www.mathworks.com/. Computer Software, Retrieved on Sep-2016.

[36] G.L. Plett. *Equivalent-Circuit Methods*, volume II of *Battery Management Systems*. Artech House, 2016.

[37] H. Hilaire and M. Ausman. Airbus A^3 Vahana company visit. Personal communication on 21-May-2018.

[38] F. Oliviero. Flight Performance and Propulsion department meeting on battery prognostics. Personal communication on 8-Nov-2018.

[39] M.A. Patterson and A.V. Rao. GPOPS-II: A MATLAB software for solving multiple-phase optimal control problems using hp-adaptive gaussian quadrature collocation methods and sparse nonlinear programming. *ACM Transactions on Mathematical Software (TOMS)*, 41(1):1:1–1:37, 2014.

[40] IBM Analytics. CPLEX Optimizer, high-performance mathematical programming solver for linear programming, mixed integer programming, and quadratic program. www.ibm.com/analytics/data-science/prescriptive-analytics/cplex-optimizer. Computer Software, Retrieved on Nov-2016.

II

Technical Report

1
Introduction

This chapter introduces the eVTOL arrival sequencing and scheduling research. It discusses the motivation and relevance of the project in Section 1.1. Afterwards, the aim of the research and corresponding research questions are discussed in Section 1.2. The research scope and the structure of the report are described in Section 1.3 and 1.4, respectively.

1.1. Motivation and Relevance

In the past few decades, commuting time has been rising everywhere around the world. Commuters in Los Angeles e.g. spend more than 100 hours in traffic jams every year, while the average in America is one hour every week. Traffic congestion in London, UK costs drivers more than £2,000 each [1]. Traffic problems lead to a loss of time, increase in fuel consumption and emissions and in general a lot of stress. Besides, mountainous areas and natural parks do not always allow commuters to travel 'as the crow flies'. Therefore, multiple research groups have been working on on-demand Urban Air Mobility (UAM) using small air taxis, such as Uber Elevate [2], NASA [3] and several universities worldwide [4, 5]. This started already in the 20^{th} century by introducing the 'Small Aircraft Transportation System' using existing fixed-wing single-pilot aircraft. An annual decline in pilots licensed for personal transport, a limited number of airports, challenges in air traffic management and high costs made this idea unattractive for further research [3]. Later, electric Vertical Take-Off and Landing (eVTOL) vehicles were introduced because of their autonomous flight, zero operational emissions, reduced noise and better affordability for mass-scale use. “The convergence of technologies and new business models enabled by the digital revolution is making it possible to explore this new way for people and cargo to move within our cities," said Jaiwon Shin, NASA Associate Administrator for Aeronautics Research Mission Directorate. Companies such as Airbus, Volocopter, and Aurora Flight Sciences are working with their battery vendors to build and test eVTOL aircraft to ensure that vehicle safety and energy efficiency become an integral part of people's daily commute. However, there is a lack of a concept of operations and air traffic control tools to support safe and efficient UAM operations with these new eVTOL aircraft.

Unmanned Aircraft System (UAS) Traffic Management (UTM) is currently under development for small UAS up to 25 kg, also known as drones, for a wide range of applications e.g. agriculture, cargo delivery and rescue operations. Unlike these drones that can take off and land almost anywhere in the UTM framework, eVTOL vehicles need to take-off from and land at vertiports e.g. on top of a high-rise building or within suburbs. When UAM operations become a reality and increase in the future, one of the major emerging bottlenecks will be the limited number of vertiports and landing pads, which will create a denser arrival UAM traffic in the corresponding terminal airspace. Therefore, UAM arrival is expected to be the most safety-critical flight phase due to high-density terminal traffic, low remaining eVTOL battery energy and limited resources or vertiport landing pads. Current arrival procedures and arrival sequencing and scheduling tools for commercial aviation are widely available and developing at a high pace, but can not directly be implemented for eVTOL arrivals for several reasons: 1) the arrival trajectories are different due to the capability of landing vertically, 2) the on-demand service of UAM requires real-time arrival scheduling and -tooling, 3) the limited eVTOL battery capacity requires arrivals to be executed for minimal energy consumption and to be scheduled while considering the remaining battery energy and 4) the limited vertiport landing pad capacity may constrain the time between each arrival. NASA also explicitly describes the desire for this research: "Dynamic scheduling for on-demand access to constrained resources and interaction between vehicles." [6]. Therefore, this research focuses on designing the optimal UAM arrivals by integrating airspace design, trajectory optimisation, eVTOL battery modelling and arrival scheduling to enable safe and efficient flight operations in on-demand urban air transportation.

1.2. Research Objective and Questions

The research objective of this study is to take the first step in the development of Urban Air Mobility Traffic Management for autonomous on-demand eVTOL operations by developing the arrival procedures and arrival sequencing and scheduling tool searching for minimum total delay considering limited battery power and vertiport landing pad capacity. To reach this research goal, several sub-goals are formed:

1. Develop a first airspace design for UAM.
2. Find the optimal arrival trajectory for an eVTOL aircraft.
3. Develop a model that can predict remaining flight time based on battery status.
4. Adapt existing arrival sequencing and scheduling algorithms for on-demand UAM using eVTOLs.
5. Show a proof of concept of the arrival sequencing and scheduling model.
6. Consider a data set that estimates the expected demand and frequency of eVTOL arrivals.

From the motivation and aim of research as described above, the main research question has been defined:

How can on-demand eVTOL aircraft arriving at a vertiport be sequenced and scheduled for minimum delay considering limited battery power?

To answer this, multiple core questions have been identified which are further split up into sub-questions.

1. What technique should be used for an optimal arrival of eVTOLs at a vertiport?
   (a) What arrival sequencing and scheduling techniques are currently used for commercial aviation?
   (b) What arrival sequencing and scheduling techniques are currently used for helicopter operations?
   (c) What are the differences and additional constraints for on-demand eVTOL arrivals compared to current commercial aviation and helicopter operations?
2. How can the eVTOL arrival sequencing and scheduling be translated into a mathematical optimisation model?
   (a) What airspace configuration and arrival procedures will be assumed most appropriate for eVTOL arrivals at a vertiport?
   (b) What are the assumptions, decision variables and objective of the mathematical model?
   (c) What are the constraints with respect to:
      - Battery power
      - Separation
      - Vertiport landing pad capacity
      - Delay
3. How is the design of the scheduler with regard to the relevant assessment criteria for designing a scheduler?
   (a) What is the maximum eVTOL arrival capacity of the proposed model?
   (b) What is the effect of assuming energy-optimal trajectories on the proposed model outcome?
   (c) What is the effect of the eVTOL battery constraint on the proposed model outcome?
   (d) What is the effect of minimum separation on the proposed model outcome?
   (e) What is the effect of the airspace configuration on the proposed model outcome?
   (f) What is the performance of the algorithm in terms of computational time?

1.3. Research Scope

The arrival procedures and arrival sequencing and scheduling model will be realised to simulate one day of eVTOL operations. During the research, the following is considered:

1. Each eVTOL network is operated as a monopoly market, such that only *one eVTOL type* is flown in the network simultaneously.
2. The eVTOL arrival sequence and schedule is generated for eVTOL arrivals at *one vertiport* in the network.
3. eVTOLs operate in a *segregated airspace volume*, such that separation from other forms of aviation and UAS is already ensured.
4. eVTOL arrival flight trajectories are *deterministic*, such that stochastic wind, weather influences etc. are not modelled.

1.4. Structure of this Report

The aim of this final report is to describe the research on eVTOL arrival sequencing and scheduling in on-demand Urban Air Mobility. It elaborates on the entire research process, assumptions and mathematics and results through the following report structure. Chapter 2 summarises the literature study in which the past research on UAM, eVTOL arrival trajectories, battery models for aviation and arrival procedures and arrival sequencing and scheduling models in commercial aviation are discussed. Afterwards, the concept of operations for the arrival of eVTOL vehicles at a vertiport is described in Chapter 3. Chapter 4 discusses the eVTOL arrival sequencing and scheduling model using the eVTOL arrival trajectory optimisation and simplified battery formulation. It also covers all model variations based on hover, rolling horizon and a double landing pad design. Afterwards, the results of the trajectory optimisation, battery model and first proof of concept using 10 eVTOL arrivals are shown in Chapter 6. An elaborate case study on daily eVTOL arrivals at a vertiport using a demand model for Houston, TX, USA is described in Chapter 7. A sensitivity analysis in Chapter 8 discusses the sensitivity of model parameters and assumptions made during the design of the eVTOL arrival sequencing and scheduling tool. A short description of the model verification and validation process is described in Chapter 9. Chapter 10 finishes the report with a short conclusion and recommendations for further research. Appendix A provides a guideline through the code packages written for this research purpose and Appendices B and C shows the detailed eVTOL arrival sequencing and scheduling results.

2

Background

This chapter describes the background researched during the literature study on UAM arrival sequencing and scheduling. Section 2.1 elaborates on the UAM concept and the eVTOL vehicles, after which work on energy-efficient arrival trajectories for eVTOLs is discussed in Section 2.2. Section 2.3 covers available battery models for electric or hybrid aircraft and drones. Section 2.4 and Section 2.5 describe the arrival procedures and arrival sequencing and scheduling tools used in commercial aviation, respectively. At last, Section 2.6 describes demand models for the arrival of aircraft and eVTOLs. The complete literature study can be reviewed in [7].

2.1. Urban Air Mobility

Urban Air Mobility (UAM) can potentially solve traffic congestion in large urban areas by providing transport through three-dimensional airspace at the request of the passenger. Besides, using electric Vertical Take-Off and Landing (eVTOL) vehicles will allow for rapid take-off and landing and zero operational emissions, while noise is reduced and affordability is improved compared to current small general aviation aircraft and helicopters. Multiple research groups have been working on the challenges and feasibility of UAM [2–4], see Subsection 2.1.1. The eVTOL aircraft and the Air Traffic Management of Unmanned Aerial Systems is discussed in Subsection 2.1.2 and Subsection 2.1.3, respectively.

2.1.1. Current Vision and Challenges

The UAM concept is delineated by [2–4, 8] as eVTOLs flying from point to point between vertiports within the cities and suburbs using flexible flight routes, preferably geodesic paths. The development of infrastructure to support operations is cheaper than building or extending ground infrastructure due to the use of free airspace and realisation of vertiports on top of existing high-rise buildings or water platforms. An impression of what the vertiports around a city are envisioned to look like is depicted on the front page. The Uber company [2] is currently partnering with three launch cities, amongst which Dallas, Texas, USA and Los Angeles, California, USA have already confirmed their participation. The three cities will be the first to offer UberAIR flights, with the goals of operating demonstrator flights starting in 2020 and beginning commercial operations in 2023. Lilium is working parallel to Uber and its stakeholder by designing both its own vehicle and its own operations [8]. A case study by eVTOL design company Lilium on a commute between JFK International Airport and Manhattan, New York City, New York shows that UAM can reduce the travel time of 55 min by taxi to a travel time of 5 min. Besides, the price of an on-demand eVTOL flight will range from $36 initially to only $6 on the long term compared to a $56-73 taxi ride and can be ordered via the smartphone.

In [2] the challenges currently faced in the UAM industry are described in terms of certification needs, availability of eVTOLs and infrastructure, community acceptance regarding privacy and noise, traffic management and operational challenges. The nature of some of those challenges and a quantification of their impact are researched in [4] by performing a case study on Los Angeles, USA. The results are depicted in Figure 2.1. This study will focus on one of the operational challenges relating to the Air Traffic Control (ATC), which is expected to limit UAM or On-Demand Mobility (ODM) for a high network density. ATC faces problems regarding safe separation between all aviation types and an autonomous infrastructure such as voiceless interaction. Therefore, Subsection 2.1.3 takes a closer look into research performed on ATC for unmanned aerial vehicles.

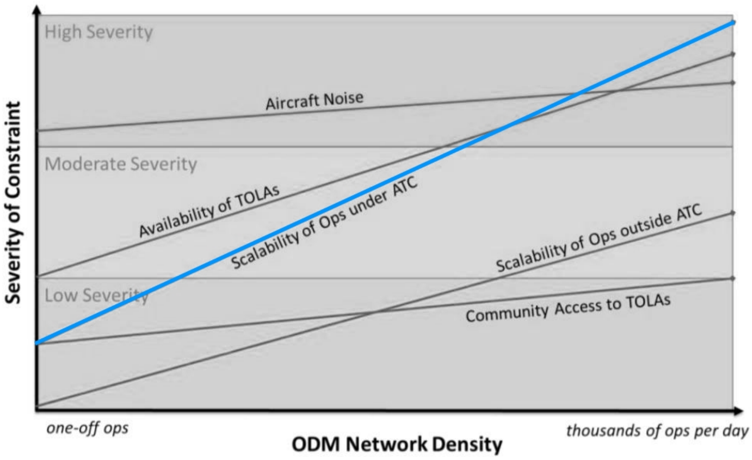

Figure 2.1: Severity of Constraints on On-Demand Mobility with respect to Network Density [4]

2.1.2. eVTOL aircraft

Together with the development of UAM goes the design of Electric Vertical Take-off and Landing aircraft (eVTOLs). This type of aircraft is rapid in manoeuvres, reliable due to autonomous flight and has zero operational emissions. Besides, using electric propulsion makes flying more affordable under a high number of operations and reduces noise compared to helicopters or general aviation. Although over fifty companies worldwide are working on designs for this promising new market, it is not yet possible to buy eVTOLs. The main challenges in eVTOL production are the certification process, the battery technology, vehicle efficiency, vehicle cost and vehicle performance and reliability. By the use of Distributed Electric Propulsion (DEP) safety is increased and noise is abated, but design challenges and increased cost are faced due to complexity. Besides, the current battery technology does not yet provide sufficient power per unit weight, or specific energy, for long-range commutes. Also, the speed of charge, or charge rate, is yet too long to allow for fast turnarounds [2].

Figure 2.2: EHANG-184 Coaxial Multi-rotor eVTOL [9]

Variable	**Value**
Cruise duration above sea level [min]	25
Cruise speed [km/h]	100
Range based on cruise speed [km]	42
Cruise altitude [m]	500
Payload mass [kg]	100
Aircraft net mass [kg]	260
Charging time [min]	60
Number of engines & rotors [-]	8
Propeller diameter [m]	1.6
Fuselage length [m]	4.0
Tip-to-tip length [m]	2.1

Table 2.1: EHANG-184 Specifications [9]

The current eVTOL designs vary highly in layout, e.g. autogyros, twin-hull, tilt-wing, multi-rotor [10, 11], which all have different flight performance and flight dynamics, thus require different concepts of operations. Therefore, a specific eVTOL type is selected for the research discussed in this report based on the public availability of flight performance data and the maturity of the design e.g. status of prototype flight testing. The EHANG-184 [9] was found to be one of the furthest developed eVTOL designs and also is the model used in arrival trajectory research [5] as described later in Section 2.2. The EHANG-184 (Figure 2.2) is a multi-rotor eVTOL air taxi designed to carry a single person payload. The vehicle is classified as a short range and low-speed eVTOL, as depicted in the vehicle specifications in Table 2.1.

2.1.3. Unmanned Aircraft Systems Traffic Management

Different from general aviation, eVTOLs are envisioned to fly autonomous and thus there is no flight crew available to communicate with ATC. Therefore, voiceless or automatic conflict detection and resolution should be realised between eVTOLs and the surrounding aviation. Each Unmanned Aircraft System (UAS) encounters this challenge whilst using the freedom of 3D airspace for several purposes, e.g. passenger transport and cargo delivery. Unmanned Aircraft Systems Traffic Management (UTM) refers to the Air Traffic Management of these UASs [12] and is researched amongst others by NASA.

Due to the complexity of the integration of UASs into the existing ATC procedures, NASA assumes in this early development stage that UAS and thus eVTOLs operate in a segregated, uncontrolled airspace [13]. To account for further development stages, they pose two main operating principles to all research in the UTM field. First, it should implement flexibility where possible but structure where necessary. Second, it should use a risk-based approach where geographical needs will dictate the performance requirement for airspace operations.

However, sufficient separation between the eVTOLs itself also needs to be ensured. In [14] continuous eVTOL vehicle routing, departure and arrival scheduling for UAM is developed such that minimum separation is ensured and eVTOL traffic is integrated with existing air traffic. It uses a highly-autonomous AutoResolver algorithm developed for traditional aviation and adapts this to future eVTOL operations in the Dallas-Forth Worth metroplex with 20 vertiports. It performs case studies on different separation requirements and scheduling horizons. It does, however, not consider limited battery power of the eVTOL aircraft, neither a limited vertiport landing pad capacity. Besides, it does not discuss ATC procedures for eVTOL flight. This research, therefore, focuses on the proposal of arrival procedures and the adaption of arrival sequencing and scheduling models from commercial aviation to the arrivals of eVTOLs considering limited battery power.

2.2. Previous Energy-Efficient eVTOL Arrival Trajectory Research

First work on eVTOL arrival management is an eVTOL arrival trajectory research presented in [5]. The tool presented is able to compute the most energy-efficient arrival trajectory for the EHANG-184 eVTOL (see Subsection 2.1.2) with Required Time of Arrival (RTA) constraint. The rotorcraft equations of motion are continuous-time nonlinear differential equations, such that the trajectory optimisation problem is solved numerically using commercially available GPOPS-II software [15]. [5] evaluates optimal trajectories and their energy consumption for different pitch settings, different approach trajectories and delay absorption methods based on the RTA obtained from an arrival schedule. The conclusion states that the collective pitch mechanism is required for the operational feasibility of a multi-rotor eVTOL vehicle considering passenger comfort, compared to using fixed pitch during descent. Besides, flying a shallower descent trajectory is found to be the most energy-efficient method of delay absorption compared to e.g. holding or cruise speed reduction.

2.3. Battery Models for Electric Aircraft and Drones

Like any other vehicle or device running on batteries or fuel, the Remaining Useful Time (RUT) depends on how intensively it is used [16]. The battery is assumed to be empty, so RUT is reached, at either a State of Charge (SOC) lower limit or terminal voltage. However, currently no simple method exists to determine when this RUT is reached based on a known flight or power demand profile and thus if a planned flight mission is feasible for given battery status. Sophisticated battery models for this purpose are available for an electric winged aircraft in [16–18] and for a drone in [19]. These models create a voltage and SOC profile based on a flight plan using an Equivalent Circuit Model (ECM). However, the ECM parameters are determined by battery or flight testing or provided by the battery manufacturer so are aircraft (type) specific. Flight test data, battery models or battery characteristics are not publicly available for the currently developed eVTOL designs. Besides, eVTOL design companies do not share battery details as this is highly restricted intellectual property [8, 20]. A simplified battery model proposed in [21] is therefore advised for this research. This model is recommended for short periods of operation and situations where the initial conditions are well known. Both apply to the arrival of eVTOL aircraft as long as the initial SOC measurement inside the eVTOL is accurate.

2.4. Arrival Management in Commercial Aviation

Subsection 2.1.3 discussed the current developments in Unmanned Aircraft Systems Traffic Management. However, this literature does not provide enough information to perform safe and reliable arrival management for eVTOLs. Therefore, this section describes arrival procedures and scheduling tools for commercial aviation, as they can serve as a good starting point for this work in UAM.

The terminal airspace (referred to as TMA or TRACON) around the larger airports is fully controlled and usually, traffic is organised and metered via meter gates on the area border [22, 23] as also seen in Figure 2.3. These meter gates also enable separation between departing and arriving traffic, which allows for separate scheduling of aircraft departures and arrivals. Furthermore, different types of aircraft (e.g. jet vs. turboprops) are separated until the final descent phase. Inside the terminal airspace, standard arrival routes (STARs) are used to guide the aircraft to the runway. These STARs are step-down or continuous descent approaches (CDAs), whether using level-offs during descent or not. CDAs are beneficial in terms of fuel consumption and noise abatement, but in general lead to a lower arrival capacity and thus increased arrival delay. Therefore, step-down approaches are commonly applied when capacity is at its maximum and when obstacles (e.g. mountains) need to be cleared [24]. Aircraft entering the TRACON are separated by holding, radar vectoring [25] or a point-merge approach [26, 27]. The latter uses a route structure consisting of a merge point and segments tangent to a circle around this point, such that aircraft can be directed at any time. However, this method is not further evaluated for UAM due to the reduced flexibility in, e.g. energy efficient route selection. Radar vectoring is possible in UAM, but not recommended by [5, 28] due to the higher energy consumption in combination with the limited battery power of the vehicles.

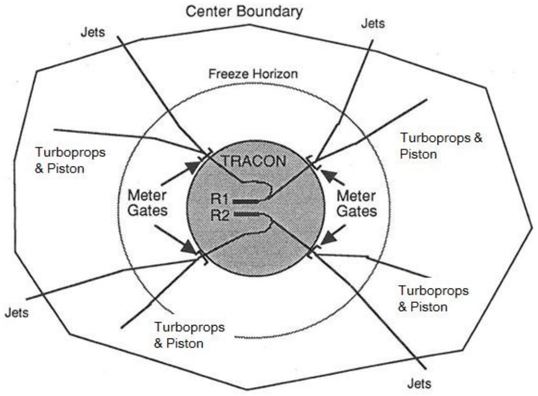

Figure 2.3: TRACON Airspace Structure and Arrival Routes [22]

Helicopter arrivals are described in [29, 30]. Most helicopters fly a similar approach path as winged aircraft, although they have the capability to land vertically like eVTOLs. This is to enable the use of autorotation in case of engine failure and to prevent losing lift in a vortex ring state.

2.5. Arrival Sequencing & Scheduling Models in Commercial Aviation

Arrival sequencing and scheduling tools are widely available for commercial aviation such that ATC can ensure that [31]: an aircraft has time to safely fly from its current position to the runway, the aircraft do not run low on fuel and aircraft are sufficiently separated from each other. All those requirements are also important to Urban Air Mobility and thus an arrival sequencing and scheduling model is needed. This model should provide a landing sequence, landing time and a runway or landing pad assignment. These, in turn, lead to a choice of approach route, holding and approach and descent speed. This section explains the research that is available on arrival sequencing and scheduling models in commercial aviation and what these models miss before applying the technique to eVTOL arrivals.

2.5.1. Objectives in Arrival Sequencing & Scheduling Models in Commercial Aviation

Different stakeholders may have different interests regarding the goal of arrival sequencing and scheduling leading to different objective functions in such algorithms. An overview of all objective functions that are used in arrival sequencing and scheduling for commercial aviation is provided below.

- Time-based objectives, e.g. minimise total delay [22, 32], minimise deviation from the target time [31, 33], minimise average delay [34], minimise average approach and/or landing time [23], minimise makespan or time of latest arrival [35]
- Cost-based objectives, e.g. minimise crew and/or passenger cost [36]
- Fairness objectives, e.g. maximise fairness among the aircraft [34]
- Environmental objectives, e.g. minimise fuel burn [37], minimise environmental impact (noise and emissions) [38]
- Multi-objectives, e.g. a combination of cost-based and environmental objective [36]

Although arriving on time is one of the priorities always observed within commercial aviation, it is even of higher importance to Urban Air Mobility. As passengers pay to arrive at their destination faster than when driving a car or taxi, being late is highly undesirable. Besides, the short-haul nature of UAM compared to commercial aviation makes delay have a relatively large impact on travel time. Furthermore, environmental cost is low due to the zero operational emissions and the noise abatement from using Distributed Electric Propulsion and crew cost is irrelevant for autonomous vehicles. Therefore, the remainder of this research focuses on arrival sequencing and scheduling models that use a time-based formulation and minimise delay.

2.5.2. Constraints in Arrival Sequencing & Scheduling Models in Commercial Aviation

This subsection discusses the constraints that are recognised in commercial arrival sequencing & scheduling tools with a time-based objective. An overview is provided below.

- Minimum separation between aircraft based on sequence and runway selection [33, 38]
- Landing time window based on flight dynamics, current location and remaining fuel [33, 38]
- Constrained Position Shifting (CPS) limiting the maximum number of shifts relative to the First Come First Serve (FCFS) order [32, 34]
- Runway capacity based on the number of runways, ATC workload and runway clearance [33, 38]
- Airline preferences [39] e.g. precedence constraints [35]
- Reality constraints e.g. sequence decision, runway selection and non-negative time [33, 40]

Ensuring sufficient separation between aircraft is the main goal of arrival sequencing and scheduling and therefore time separation requirements are important. In commercial aviation using winged aircraft, separation requirements are defined by several aspects including wake vortex separation requirements, runway occupancy time, geometry of the final approach, runways and runway exits, mix of aircraft type, time between approach fix and landing [41]. The ICAO wake vortex separation requirements are in general critical for this type of aviation. Those standards are converted to the time domain and varying in value mostly between 60 s [31, 39] and 90 s [40] but can raise up to 196 s [32] when a lightweight aircraft follows a heavy aircraft. The same wake vortex conditions apply to helicopters performing a shallow approach [42]. On top of that, helicopters must avoid flying into each other's downwash caused by the main rotor. This requires an avoidance radius of three times the rotor diameter in slow hover taxi or stationary hover. The advantage of eVTOL flight over helicopter operations on this topic is the DEP, such that multiple rotors are operated. In [43] a study on UAM airspace system demand is performed for a range of values that future separation requirements would need to take to support high-demand, high-tempo UAM operations. The research concludes that the circular horizontal distance around an eVTOL would likely be in the range of 1000 ft – 3000 ft. Other research or time-based separation requirements for eVTOLs are not available yet.

An interesting observation in the other arrival sequencing and scheduling constraints is that none of the reviewed literature describes the fuel level of arriving aircraft as a direct constraint. However, remaining battery level of eVTOL aircraft will limit eVTOL flight and thus the arrival sequencing and scheduling tool with current battery technology [2]. Furthermore, the overview does not show any constraint on available ground space other than the runway. The current vision on the vertiport infrastructure on top of high rise buildings might lead to a limited number of parking spots for eVTOLs, especially when battery charging time is required. However, the time window, separation, constrained position shifting and reality constraints can be implemented in the eVTOL arrival sequencing and scheduling model.

2.5.3. Solution Techniques for Arrival Sequencing & Scheduling Models in Commercial Aviation

To solve the arrival sequencing and scheduling problem at an airport, both stochastic [35, 44] and deterministic models are available. Because of the new application, limited knowledge on eVTOLs and UAM and on-demand service, it is preferred to stay with a fast, relatively straightforward and simple sequencing and scheduling method. Therefore three types of deterministic models are discussed: (constrained) position shifting (CPS) [22], linear programming and dynamic programming [35, 45]. The main disadvantage of position shifting is the high computational time required to solve for a relatively small dataset. Furthermore, dynamic programs are complex, especially when applying non-linear objectives, while this first work mainly has to show a proof of concept for the new formulation and constraints. Mixed-Integer Linear Programs (MILPs) are therefore further discussed. Different algorithms are available to efficiently solve the MILP, such as branch-and-bound [33], column generation [46], branch-and-price [47] or data-splitting [32, 48]. A combination of both is also possible [33, 47]. Besides, [49] proposes to eliminate aircraft pairs for the set that are separated anyway. A heuristic is commonly applied to commercial aviation problems to further reduce the search space of the optimisation or approximate the final solution using a fast computation [31, 33, 50]. As UAM traffic is assumed to arrive on-demand and thus scheduling cannot be performed far ahead, large data sets will not need to be solved. A rolling horizon approach is, therefore, a good technique to incorporate this short look-ahead period and the on-demand arrival uncertainty as described in [51, 52]. In other runway sequencing problems in commercial aviation, solutions were provided to aircraft that were 15-30 [38] or even 40 minutes [22] from the approach fix or runway.

Table 2.2 shows an overview of the most relevant literature on arrival sequencing and scheduling. The formulation column consists of the type of formulation, in which D stands for deterministic models and S for stochastic. The constraints listed in the table are added on top of the separation and landing time window constraints used in all literature.

2.6. Demand Models for the Arrival of eVTOLs and Aircraft

As no historical data set of UAM is yet available, data to validate the arrival sequencing and scheduling model needs to be generated using an expected demand. An elaborate system-level analysis of on-demand mobility for aviation by [4] shows the constraints on the realisation of UAM for low to very high operations per day. It states that thousands of operations per day can be expected on the long run. The feasibility of UAM is also researched by [53], in which case studies are performed on e.g. the San Fransisco Bay Area using a discrete event simulator called BaySim. The results show a maximum amount of simultaneous flights between 40-100 and a maximum preflight delay between 6-15 minutes. [53] assumes constant air travel times and 8 vertiports, relating to an envisioned demand of over 800 operations per day per station. Another system-level model on the number of eVTOLs needed in the system to meet UAM demand, the number of eVTOLs airborne at any given time, and the length of time eVTOLs may have to loiter before arriving at a landing pad has been developed in [54]. It presents a network of 7 vertiports in Houston, Texas and an hourly stochastic demand distribution based on [2]. The demand distribution consists of the sum of three normal distributions: two with a standard deviation of 2 hours centred at 8AM and at 4PM, respectively, to simulate rush hour peaks and a third with a standard deviation of 6 hours centred at 12AM to simulate day- versus nighttime.

Demand models for aircraft arrivals are also reviewed. The generation of input data for 1000 problem instances and 30 aircraft sequences using a Poisson distribution and a known arrival rate is described in [50]. This probability distribution function is also applied in [46] for any type of queuing system. Errors in aircraft ETA at the metering fixes in [39, 44] are modelled by adding an approximately Gaussian distribution to the nominal ETA at the feeder gate. Besides, research has been performed on the expected flight frequency resulting from on-demand low-cost flights using electric winged aircraft by [55]. It expects 124 electric on-demand flights operated daily per airport on average in the USA.

Table 2.2: Overview of Literature Review on Arrival Sequencing and Scheduling Models

Source	**Formulation**		**Objective**	**Constraints**	**Problem size**	**Solution method**	**Novelty/Relevance**
2000 [33]	D	MILP	min total deviation of target time	runway selection & capacity, ATC workload	4 runway, 50 aircraft	Reduces search space by eliminating aircraft that are separated anyway, uses heuristic to find upper bound on optimal solution, tighten time windows and restart LP relaxation tree search till no improved feasible solution found	General formulation and solution method
2000 [49]	D	MILP	min total delay		1 runway, 10 aircraft	Reduces search space by eliminating aircraft that are separated anyway, only describes the very basics of arrival sequencing	Simplified reduction of search space
2000 [56]	D	MILP	min deviation from airline preference	airline preference	4 feeder gates, 3 runway, 108 aircraft	Fast-time simulation combining an airport model, a statistical model of the arrival traffic flow and the scheduler. The baseline ETAs are based on airline preferences rather than the FCFS sequence.	ETA baseline based on airlines preference
2001 [38]	D	MILP	min environmental impact and delay	runway clearance	30 airports up to 8 runways, 95 aircraft/hr	Does not discuss how the solution is found. Model combines departures and arrivals.	Multi-objective function
2001 [31]	D	Non-linear	min total deviation of target time		1 runway, 20 aircraft	Population heuristic	Population heuristic
2005 [47]	D	MILP	min total deviation of target time		4 runway, 50 aircraft	Simple heuristic method based on [33] is used to determining the upper bound for the total cost of the given landing problem 2) branch-and-price: combined column generation with branch-and-bound	Branch-and-price algorithm
2007 [35]	S	Dynamic	max reliability, min makespan	precedence, CPS	1 runway, 50 aircraft	Dynamic program can accommodate for several sources of uncertainty	Stochastic dynamic program
2012 [57]	S	Dynamic, MILP	min total deviation of target time, min makespan		1 runway, 30-50 aircraft	Multiple algorithms including a two-stage using Lagrangian decomposition and a single stage using branch-and-bound or a machine scheduling metaheuristic	Several solution techniques
2014 [22]	D	CPS	min total delay		2 runway, 4 aircraft	Two-stage: 1) landing time and runway assignment based on trial of all possible solutions and minimum time spacing 2) assign time to cross meter fix based on delay distribution function	Two-stage position shifting
2016 [32]	D	MILP	min total delay		1 runway, 40 flights	Data-splitting algorithm	Data-splitting algorithm
2017 [58]	D	CPS	min total delay		1 runway, 200 aircraft, 2000 instances	Simulated Annealing	Simulated annealing for CPS
2017 [44]	S	PSO, MILP	min makespan		20 sets, 8 aircraft per set	Two-stages in which first the sequence is determined and then the landing time using particle swarm optimisation	Particle Swarm Optimisation
2017 [48]	D	MILP	min makespan	runway selection, CPS	2 runway, 30 aircraft	Data-splitting algorithm	Extension of [32] now using new objective and two runway
2017 [45]	D	Dynamic	max runway utilisation, min total delay		1 runway, 55 aircraft per set, 500 sets	Objective function is non-linear non-convex and thus solved using a dynamic program with six pruning rules	Dynamic program combined with pruning
2017 [40]	D	MILP	min total delay		3 sets, 200 aircraft per set	Reduces search space by eliminating aircraft that are separated anyway	Combining sequencing and scheduling with trajectory optimisation

3

Concept of Operations for eVTOL Arrival

Section 2.1 already described the infrastructure for on-demand UAM as envisioned by companies such as Uber Elevate and NASA. It describes the eVTOL operating on the request of passengers from point to point between vertiports. These vertiports are expected to be located in highly urbanised areas, such as cities, suburbs and business districts. However, none of the described literature discusses a proposal for the design of the airspace around a vertiport. Therefore, this chapter sketches the ConOps for eVTOL arrival management as used for this research and simultaneously covers the assumptions made. This ConOps has been designed for the arrival of the EHANG-184 eVTOL at one vertiport in a segregated airspace. Section 3.1 discusses the ConOps when using a single landing pad at the vertiport, after which Section 3.2 describes the ConOps for a double landing pad infrastructure.

3.1. Concept of Operations using a Single Landing Pad

The designs of helipads in the past and first proposals for future vertiport landing pads consist of one landing pad. Therefore, this first ConOps covers the arrival of eVTOLs at one vertiport using one landing pad. Figure 3.1 and 3.2 show the side and top view of the ConOps for eVTOL arrivals at a single pad vertiport inspired by the concepts discussed in Section 2.4.

3.1.1. Organisation of the Airspace around a Vertiport

The ConOps uses separate approach and departure fixes, ensuring separation between approaching and departing traffic and thus allowing this research to focus on arrivals only. Besides, those so-called 'metering gates' provide an organised and safe method to funnel traffic into and out of the high flight density areas around the vertiport, referred to as the Final Approach Area (FA). Another advantage of using a Final Approach Area with approach fixes is that it pushes the delay absorption to an area with lower traffic density. This leads to a lower conflict risk and more space and possibilities to absorb delays. In Figure 3.2, the outer boundary indicates the Terminal Area (TMA) at which incoming eVTOLs are monitored and the arrival sequencing and scheduling is initiated to ensure sufficient separation between aircraft. Outside this boundary, separation is assumed to be ensured by an autonomous collision detection and avoidance system on each eVTOL and therefore outside the scope of this research. The inner boundary in this figure indicates the Final Approach Area (FA).

3.1.2. Arrival Route of an eVTOL to a Vertiport

Arrival management concepts in commercial aviation, e.g. [22, 24] use a principle similar to Standard Terminal Arrival Routes (STARs) which describe the trajectory and speed vector (ground, vertical) for each aircraft type inside the Terminal Area. As flying a constant and predefined trajectory reduces uncertainty, collision risk is further reduced. The same principle is applied to flight inside the Final Approach Area in this eVTOL arrival sequencing & scheduling research, see again Figure 3.1.

From [5] it was concluded that the most energy-optimal delay absorption method for multi-rotor eVTOL types, like EHANG-184, is by flying a more shallow descent than the standard 'fast' descent trajectory (see Figure 3.1).

Therefore, the arrival sequencing and scheduling takes place on the Terminal Area boundary at cruise altitude. The scheduled arrival delay is then absorbed by changing the descent trajectory between the Top of Descent (TOD) and the approach fix. At the approach fixes, all eVTOLs are thus already separated based on the set separation requirement and the landing sequence is frozen. Afterwards, the eVTOLs continue inside the Final Approach Area on the most energy-efficient and also safest predefined descent trajectory. This trajectory has been designed as a horizontal flight at the altitude of the approach fix, followed by a vertical descent towards the vertiport as also depicted in Figure 3.1. Less positioning and separation uncertainty is expected from this design. Besides, clearance from high-rise buildings is ensured which is of high importance within UAM due to their operation in highly urbanised areas. At last, rotorcraft noise effects and privacy discussions regarding low altitude flight through a highly urbanised area can be minimised.

In general, helicopters do not fly such vertical final approach to allow for autorotation and avoid VRS. As multi-rotor rotorcraft are more redundant than single-rotor helicopters, a vertical approach can still be safely executed for the EHANG-184 when taking into account the maximum descent velocity. Section 2.4 also discusses the benefits of a step-down approach like in Figure 3.1 over a CDA when delay needs to be minimised and thus capacity maximised and when clearance from e.g. mountains or urban obstacles needs to be ensured.

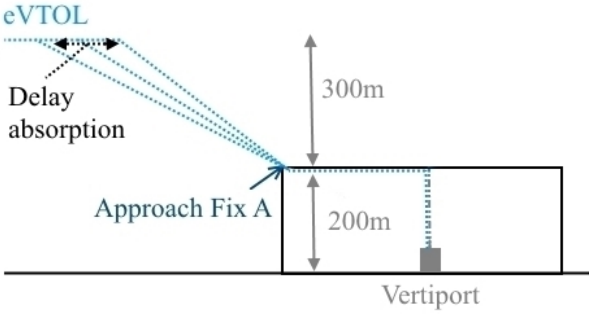

Figure 3.1: Side View of Terminal Area ConOps for eVTOL Operations

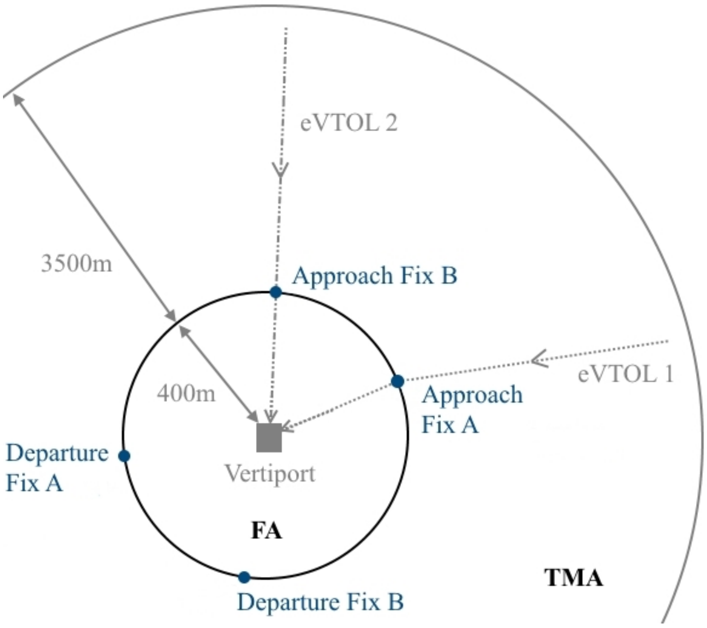

Figure 3.2: Top View of Terminal Area ConOps for eVTOL Operations

3.1.3. Scheduled Time of Arrival and Absorption of Scheduled Delay

Because battery energy is one of the limiting factors for the realisation of eVTOL operations, flying energy optimal trajectories is crucial. Therefore, it is assumed that holding, comparable to loitering in commercial aviation, is avoided as a delay absorption method where possible. Delay absorption will, therefore, be performed using three main methods. If hovering needs to be performed to temporarily increase the vertiport arrival capacity, it is performed at the TOD to avoid low-altitude noise and keep delay absorption out of high flight density airspace.

- Flying a shallow descent arrival trajectory by adapting altitude, ground speed and vertical speed profile
- Flying through the furthest approach fix by making a detour
- If these methods are insufficient: perform a hovering manoeuvre at the TOD

The baseline schedule or Estimated Time of Arrival (ETA) for each eVTOL at each approach fix is calculated based on the most energy-optimal trajectory. A deviation from the ETA is less fuel efficient and causes passenger delay thus penalised in the arrival sequencing and scheduling tool. It is assumed that an eVTOL arrival flight trajectory can be executed according to plan such that the ETA is deterministic. A safety factor on battery power is used to ensure landing in all weather conditions.

3.1.4. eVTOL Separation Requirement inside the Terminal Area

The time separation requirements specifically for eVTOLs have been determined on 90 s based on an iterative process between the arrival trajectory optimisation (see Section 4.1 and Section 6.1) and the determination of the ConOps in Figure 3.1 and 3.2. Several aspects are considered to determine the required separation between arriving eVTOLs. This includes rotor wake interactions, geometry of the final approach and vertiport landing pad occupancy time as described in Section 2.5.2 for commercial aviation. That section also describes that for lightweight aircraft following each other, separation criteria range between 60 and 90 seconds. The final time separation requirement is also tested in the Sensitivity Analysis in Chapter 8.

Considering rotor wake interactions, it should be avoided that multi-rotor eVTOLs like EHANG-184 fly into each other's rotor wake both vertical as lateral. No research has been published on rotor wake interactions between eVTOLs. Therefore, it is assumed that flying directly above each other should be avoided in the final phase of the final approach flight, so the vertical descent phase inside the Final Approach Area. From the eVTOL arrival trajectory optimisation results, discussed later in Section 6.1, this descent takes 72 s. From [43] the lateral separation should be at least 1000 ft, translating to 12 s at cruise speed (27.8 m/s) or 56 s at the horizontal flight phase inside the Final Approach Area (5.9 m/s, see Section 6.1). The limiting case is thus 72 s. To increase safety in this novel market and use the criteria approved for commercial aviation [40], a 90 s time separation requirement is set. Also looking at the landing pad capacity or occupancy time, this 90 s requirement means that the landing pad has to be completely free and the eVTOL parked within 90 s. This seems realistic and therefore no extra time needs to be added to allow for taxi and parking.

3.1.5. Terminal Area and Final Approach Area Velocity Profile

The vertical velocity profile inside the Terminal Area and Final Approach Area in Figure 3.1 is a result of the arrival trajectory simulation (see Section 4.1 and Section 6.1) and checked for passenger comfort. A maximum vertical speed is not provided by EHANG-184, but set based on induced velocity constraints. The horizontal velocity is assumed to remain constant throughout the shallow descent flight inside the Terminal Area and also after passing the approach fix into the Final Approach Area to increase passenger comfort and reduce flight trajectory uncertainty. This value is determined at 5.9 m/s by [5] and used throughout the trajectory optimisation.

3.1.6. Terminal Area and Final Approach Area Dimensions

Figures 3.1 and 3.2 show the dimensions of the Terminal Area and Final Approach Area. These dimensions have again been determined based on an iterative process between the EHANG-184 flight dynamics and arrival trajectory optimisation and the determination of this ConOps.

The cruise altitude of EHANG-184 was advised to determine the altitude of the TOD, which is 500 m. The altitude of the approach fix is set at 200 m for three main reasons. First, commercial aviation that flies a step-down approach uses a metering fix at FL100 (10,000 ft). As normal cruise altitude is around FL350 (35,000 ft), the metering fix is positioned about $\frac{1}{3}$ of the descent phase. Using the EHANG-184 cruise altitude, this would result in an approach fix altitude of approximately 170 m. Second, clearance from high-rise buildings needs to be ensured especially in UAM. Most high-rise buildings are 150-200 m high, e.g. 23, 20 and 37 skyscrapers in San Fransisco (USA), Dallas (USA) and Abu Dhabi (UAE), the cities that are referred to by Uber Elevate [2] for UAM exploration. Therefore, an approach fix altitude of at least 200 m is highly beneficial to the safety, noise abatement and public acceptance of UAM. At last, the Final Approach Area ceiling cannot be too high to allow for sufficient delay absorption possibilities by flying a shallow descent.

The Final Approach Area (FA) radius or horizontal distance between the approach fix and vertiport is set to 400 m. It is assumed that the Final Approach Area is circular and that the approach and departure fixes are equally spaced around the vertiport by at least a quarter of the Final Approach Area circumference depending on the most beneficial layout in the vertiport network. The minimal radius is then computed using the Pythagorean theorem in Equation 3.1 and 3.2 and support drawing of the geometric situation in Figure 3.3, based on the ground speed during horizontal flight (5.9 m/s, see Section 6.1) and the required time separation. This radius is rounded up for a margin of safety.

$$R_{FA}^2 + R_{FA}^2 = (v_{ground,FA} \cdot \Delta t_{sep})^2 \tag{3.1}$$

$$R_{FA} = \sqrt{\frac{1}{2} \cdot (v_{h,FA} \cdot \Delta t_{sep})^2} = \sqrt{\frac{1}{2} \cdot (5.9 \cdot 90)^2} = 375m \tag{3.2}$$

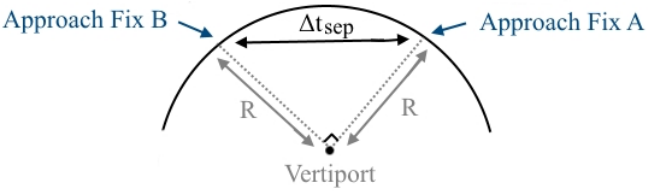

Figure 3.3: Supportive Drawing of Final Approach Area Top View for Final Approach Radius Calculations

The Terminal Area radius is set to 3900 m, such that eVTOLs report their ETA at the TOD 3500 m away from the approach fix. This radius has been determined based on a trade-off between maximising shallow descent delay absorption and minimising the duration of approach procedures. It allows for delay absorption of at maximum 360 s before arrival at the approach fix, such that 4 eVTOLs arriving at the same time can be separated 90 s in the most energy-efficient way. Besides, the complete approach procedure does not take more than 11 minutes in the extreme case, because the cruise phase of EHANG-184 takes at maximum 25 minutes.

3.1.7. Adaptability of the Proposed Concept of Operations

Although the ConOps and the eVTOL arrival sequencing & scheduling model are designed for the operation of one eVTOL type simultaneously, both are adaptable to the usage of an eVTOL mix by specifying the flight time (or transfer time) inside the Final Approach Area and the time separation requirement per aircraft type and per aircraft type combination. For example, [28] states that for a tandem-tilted wing eVTOL, delay is most energy-efficiently absorbed by reduction of the cruise speed, such that the final approach phase might be much shorter. Furthermore, the Final Approach Area is depicted as and assumed to be a perfect circle during this research. This means that only one energy-optimal trajectory needs to be computed from approach fix A or B for each aircraft type. However, the model is adaptable to different airspace shapes by specifying the transfer time from the approach fix to the vertiport for each approach fix separately. The latter will likely be required in highly urbanised areas due to e.g. high-rise buildings around the vertiport.

3.2. Concept of Operations using a Double Landing Pad

To increase the capacity of the proposed ConOps, a second landing pad can be realised on top of the existing infrastructure. This section discusses the changes made to the ConOps for a single landing pad as presented in the previous section. Figure 3.4 shows the new airspace design at a vertiport that offers two landing pads. Figure 3.1 already shows the use of two approach fixes and the arrival sequencing and scheduling tool is already capable of selecting the most efficient approach fix to fly through based on the origin of the eVTOL. Therefore, it is assumed that each landing pad corresponds to an approach fix, e.g. all eVTOL arriving through approach fix A land at landing pad A. The eVTOLs are parked between the two landing pads at the vertiport, such that passengers do not need extra transportation compared to a single landing pad design. Besides, it ensures that the descending eVTOLs are separated due to the use of descent 'funnels' from the approach fix altitude down to the vertiport.

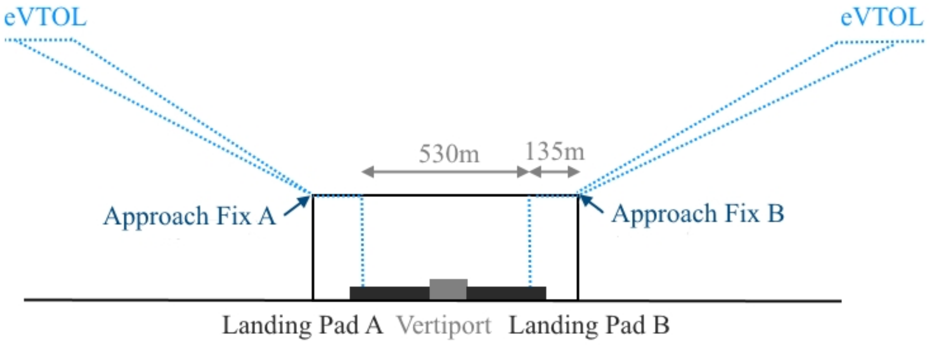

Figure 3.4: Side View of Terminal Area ConOps for eVTOL Operations using Two Landing Pads

As described, the ground speed during the horizontal phase of the final approach flight is 5.9 m/s. If a 90 s separation needs to be ensured at this speed, a distance between eVTOLs of 530 m is required. Therefore, the horizontal flight inside the Final Approach Area is reduced to only 135 m. Although eVTOLs might have the ability to descent closer to each other, no research is available for this purpose so this safe distance is used throughout this concept. The double landing pad ConOps described here would not be feasible e.g. on top of one high-rise building, but would be e.g. on two buildings next to each other or on water pads. Other than the horizontal final approach, the ConOps and arrival procedures remain the same as for the single landing pad ConOps.

4

eVTOL Arrival Sequencing & Scheduling Model

This chapter describes the total eVTOL Arrival Sequencing and Scheduling model including its side modules as depicted in Figure 4.1 for a single landing pad and double landing pad ConOps discussed in Chapter 3. This complete model determines the landing time and sequence for eVTOLs arriving at a vertiport. It uses a trajectory optimisation and battery prediction framework to determine the feasibility of each landing time per eVTOL regarding flight performance and battery status. Module 1 has been adapted from the module as described in [5], but the other modules are developed during this research. Appendix A, therefore, shows a guideline through the MATLAB coding packages developed for this model.

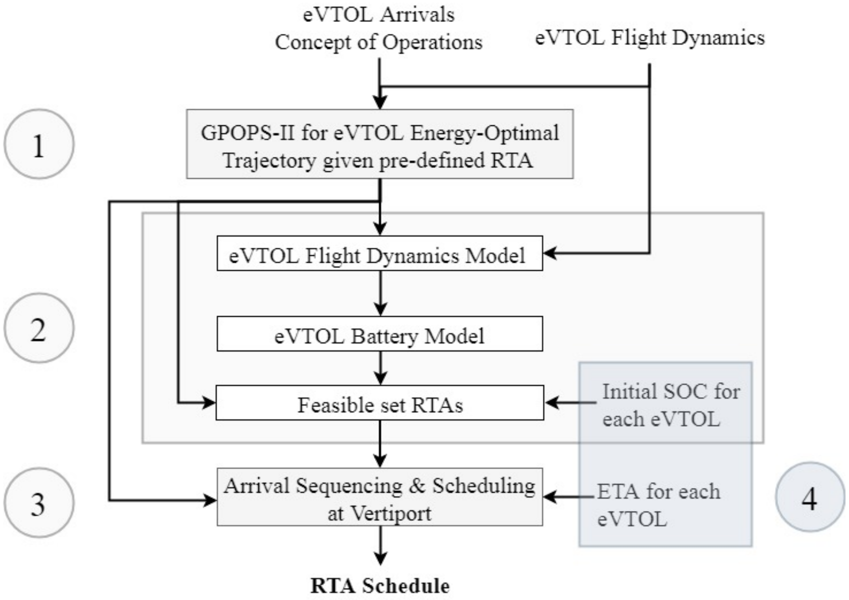

Figure 4.1: Total eVTOL Arrival Sequencing & Scheduling Model Overview

Module 1 computes the most energy-optimal arrival trajectory for an eVTOL based on the Required Time of Arrival (RTA) at the vertiport as described in Section 4.1. The module is adapted from [5] for the ConOps as proposed in Chapter 3 and uses the rotorcraft flight dynamics for EHANG-184 as described in Section 4.2. The trajectories are computed for a set of different RTAs, after which the state and control vectors corresponding to each of those so-called 'RTA trajectories' are fed into Module 2. Also, the earliest and latest feasible arrival time per eVTOL based on flight dynamics, most energy-optimal arrival trajectory and the flight time between the approach fix and vertiport landing pad is obtained from this trajectory optimisation and fed into Module 3. As the used GPOPS-II software computes the local optimum, the optimisation process in Model 1 requires manual input, iteration and verification, such that the total eVTOL arrival sequencing and scheduling is a non-iterative process.

Module 2 consists of three packages that are used to relate the initial eVTOL battery status at the Terminal Area boundary to the scheduler in Module 3. It first computes the power required to perform each of the RTA trajectories from Module 1 using the flight dynamics in Section 4.2. Afterwards, the power demand and the required SOC to perform each RTA trajectory are determined using the battery model in Section 4.3. A regression is then created between the RTAs and the required SOC. This regression is used in the last package of Module 2 to compute the latest possible landing time, relating to a set of feasible arrival trajectories, for each arriving eVTOL based on their initial SOC. This so-called RTA constraint is an input for Module 3.

Module 3 is the main eVTOL arrival sequencing and scheduling model. It computes the final landing sequence and schedule for minimal total delay while considering the computed feasible RTA window from Module 1 and 2, the required time separation between arrivals and the selection of an approach fix. Section 4.4 and Section 4.5 describe in detail the eVTOL arrival sequencing and scheduling model for a single landing pad and double landing pad ConOps, respectively.

Module 4 creates the initial SOC and ETA input for Module 2 and 3, respectively, as no historical data is available for UAM operations. A demand model is used that simulates the number of eVTOLs arriving at the TMA border per time step. It then computes the ETA at the vertiport using the flight time in the most energy-optimal arrival trajectory and the expected number of arrivals. The module is explained in Chapter 5 for a case study in Houston, TX, USA.

4.1. Module 1 - eVTOL Arrival Trajectory Optimisation Model

The eVTOL arrival trajectory optimisation model generates an energy-optimal vertical flight path for eVTOLs arriving at a vertiport at a given arrival time as elaborated on in [5, 28]. The eVTOLs are assumed to fly a geodesic or predefined horizontal arrival, such that only vertical descent optimisation is performed. The model uses the ConOps from Chapter 3 as it defines the initial and final state of each flight phase N and the rotorcraft flight dynamics from Section 4.2, because this research considers the EHANG-184 eVTOL. The rotorcraft equations of motion are continuous-time nonlinear differential equations, such that the trajectory optimisation problem is solved numerically using a pseudo-spectral method. This method transcribes a multi-phase optimal control problem to a large sparse nonlinear programming problem that is optimised using the commercially available GPOPS-II software [15]. The output of the GPOPS-II optimisation is the total energy E required to fulfil the trajectory, the state variables (vertical velocity V_x, horizontal velocity V_h, altitude h and distance d) over time t and the control variables (thrust T and pitch angle θ) over time t.

The performance index for the vertical trajectory optimisation adds the energy required in each flight phase N as given by Equation 4.1 [5]. The induced power loss per arm is represented by $P_{i,arm}$ and the term $T \cdot V \cdot sin(\alpha)$ is the power required to climb and to propel the rotorcraft forward. The profile power is assumed to remain constant due to the low forward velocity of an EHANG-184 and therefore not included in the optimisation.

$$J = \sum_{N=1}^{2} \int_{t_0^N}^{t_f^N} \left(\sum_{arm=1}^{4} P_{i,arm} + T \cdot V \cdot sin(\alpha) \right) dt \tag{4.1}$$

The trajectory optimisation is performed over 2 flight phases, making it a multi-phase optimal control problem. The multi-phase optimisation itself is performed for two flight segments based on the ConOps: 1) between the TMA border and the approach fix flying a horizontal cruise (N=1) and a shallow descent (N=2) based on the given RTA and 2) between the approach fix and the vertiport flying following a completely horizontal path (N=3) and then completely vertical path (N=4). The model searches for the optimal control inputs and the optimal TOD in flight segment 1 for different RTA inputs, while only the most optimal trajectory and RTA need to be found for segment 2. This is because no delay absorption in phase 2 is possible. The control inputs and states resulting from the control inputs are constrained to passenger comfort (V_x, θ), avoiding the Vortex Ring State (V_x), vehicle performance (V_h, T) and the initial and final state of each flight phase (t, d, h).

4.2. Module 2a - eVTOL Flight Dynamics Model for EHANG-184

To compute the ability of an eVTOL to fly a certain arrival trajectory based on its battery status, the power required to perform each stage of the trajectory needs to be known. This eVTOL flight dynamics module is designed to find the required power for each RTA trajectory from Module 1 thus based on the results for control and state variables for different RTA inputs. The power required is computed in Equation 4.2 using the vehicle dynamics stated in Equation 4.3 to 4.7. All computations are described specifically for the multi-rotor EHANG-184 and obtained from [5].

$$\begin{aligned} P_r &= P_i + P_a + P_c + P_f \\ &= 4 \cdot P_{i,arm} + T \cdot V \cdot sin(\alpha) + 0.2 \cdot P_r \\ &= 4 \cdot T \cdot v_i + T \cdot V \cdot sin(\alpha) + 0.2 \cdot P_r \\ &= 1.25\,(4 \cdot T \cdot v_i + T \cdot V \cdot \sin(\alpha)) \end{aligned} \tag{4.2}$$

where P_r, P_i, P_a, P_c and P_f are the instantaneous required, induced, parasite, climb and profile power, respectively. The induced power is computed by adding the induced power per arm i.e. coaxial rotor from the total Thrust T and the induced velocity per coaxial rotor v_i . The profile drag is assumed as 20% of the total required power. Typically the profile power is at least 10% to 20% [59], so the most critical case is chosen to prevent running out of battery. Furthermore, the true airspeed V is computed using the vertical V_x and horizontal V_h component as shown in Equation 4.3. The angle of attack α is calculated from the pitch angle θ and flight path angle γ as shown in Equation 4.4. This is different for rotorcraft compared to winged aircraft because the angle of attack is defined as the angle between rotor tip-path-plane and the velocity vector (Figure 4.2).

$$V = \sqrt{V_x^2 + V_h^2} \tag{4.3}$$

$$\alpha = \theta + \gamma = \theta + arctan\left(\frac{V_x}{V_h}\right) \tag{4.4}$$

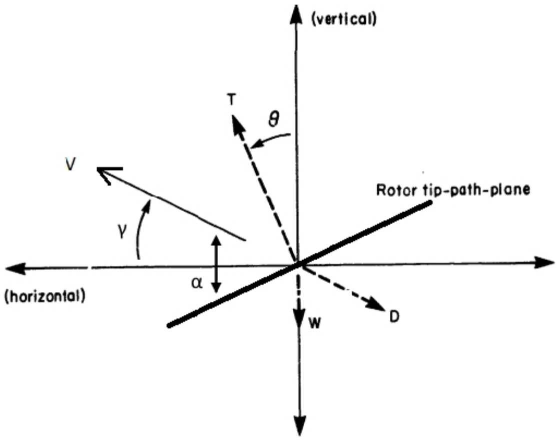

Figure 4.2: Definition of vehicle position, velocity and forces for rotorcraft [60]

The induced velocity v_i is computed using Momentum Theory and the induced velocity in hover v_h, leading to Equations 4.5 and 4.7. The fourth-degree polynomial in Equation 4.6 can be solved for v_i using the MATLAB Roots Package [61]. For the thrust per rotor T_r in Equation 4.7, it is assumed that all rotors produce equal thrust. This also means that an assumption is made on the upper and lower rotor of EHANG-184 to produce equal thrust [60], such that T_r is equal to $\frac{1}{8}T$. Furthermore, the air density ρ is assumed to be equal to international standard atmosphere density at sea level due to the low altitude eVTOLs fly on.

$$v_i = \frac{v_h^2}{\sqrt{(V \cdot cos(\alpha))^2 + (V \cdot sin(\alpha) + v_i)^2}} \tag{4.5}$$

$$v_i^4 + v_i^3(V sin(\alpha)) + v_i^2 \cdot V^2 - v_h^2 = 0 \tag{4.6}$$

$$v_h = \sqrt{\frac{T_r}{2\rho A}} = \sqrt{\frac{T_r}{2\rho\pi R^2}} \tag{4.7}$$

At some moments during descending flight, the rotor tip-path-angle θ and the total required power P_r become negative. This leads to negative power resulting from the windmill effect: the rotor rotates due to the airflow instead of motor effort. This means that no power is required and thus the power required is rounded to zero.

4.3. Module 2b - eVTOL Battery Prognostics Model

As is recognised in each electric vehicle or device, the remaining operational time depends on how intensively and for how long the vehicle or device is used [16]. The flight time of an eVTOL available for arrival thus depends on the arrival trajectory and speed profile it is going to follow. As Section 2.3 discusses, battery models and flight data are not publicly available at the time of this research. Therefore, the simplified model from [21] is advised, which is suitable for short periods of operation and for situations where the initial conditions are well known. It is assumed that the initial SOC measurement in each eVTOL is accurate, such that both conditions apply to the arrival of eVTOL aircraft.

Before converting the total electric power demand P_d to a SOC demand, the required power P_r is computed from the GPOPS-II arrival trajectory optimisation for each RTA trajectory and the flight dynamics model in Section 4.2. Equation 4.8 is then used to convert P_r to P_d [19, 21]. The difference between these is the efficiency of the rotors due to tip vortices $\eta_P = 0.7652$, the efficiency of the motor in converting electrical to mechanical power $\eta_e = 0.85$ and the safety factor $SF = 1.5$ to account for irregularities in the flight profile due to e.g. weather conditions.

$$P_d = SF \cdot \frac{1}{\eta_P}\frac{1}{\eta_e}P_r \tag{4.8}$$

Equation 4.9 and 4.11 [21] are then used to obtain a State of Charge (SOC) demand from the P_d profile for each arrival trajectory. The total current draw from all battery cells $I(t_k)$ is first computed based on P_d at each time step t_k and the nominal battery voltage V_n. Afterwards the total SOC draw SOC for the entire flight trajectory (t_0 till t_f) is found by adding the SOC draw in each time step $SOC(t_k)$ depending on the battery capacity Q.

$$I(t_k) = \frac{P_d(t_k)}{V_n} \tag{4.9}$$

$$SOC(t_k) = \frac{I(t_k) \cdot (t_k - t_{k-1})}{3600 \cdot Q} \cdot 100\% \tag{4.10}$$

$$SOC = \sum_{t_0}^{t_f} SOC(t_k) \tag{4.11}$$

The battery is assumed to be empty if it reaches a 10% SOC to prevent it from deep discharge [20, 62]. Besides, the battery capacity Q is assumed to be known and to remain constant over time. The nominal voltage V_n is also modelled constant throughout the discharge cycle [21, 62], because deep discharge is avoided. This can be observed in Figure 4.3.

Finally, the presented flight dynamics and battery prognostics model are applied to the computed arrival trajectories for different RTAs. A relation between the scheduled RTA and required SOC can now be found. From this trend line, an ultimate RTA can be assigned to each eVTOL based on their initial SOC. This in its turns is fed into the last module (Module 3), the main eVTOL arrival sequencing and scheduling tool discussed hereafter.

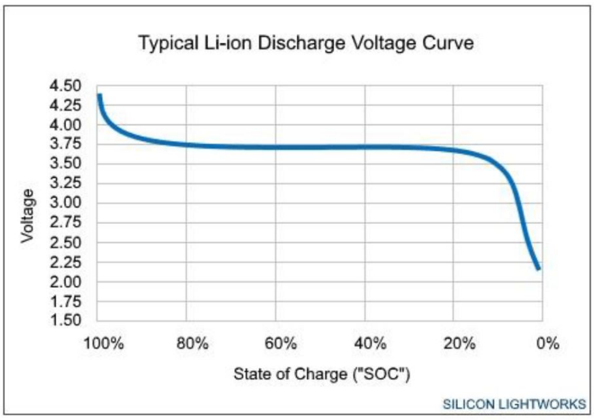

Figure 4.3: Typical Li-Ion Battery Discharge Voltage Curve [63]

4.4. Module 3 - eVTOL Arrival Sequencing & Scheduling Model for Single Landing Pad

Before covering the arrival sequencing and scheduling model for eVTOL aircraft in detail, a quick overview is provided based on the single landing pad ConOps in Section 3.1. First, the variables in the mathematical formulation are explained. Afterwards, the objective function and constraints are listed and further explained in Subsection 4.4.1 and 4.4.2, respectively. The model is designed to use inputs and provide solutions in the time domain. The formulation is adapted from similar models in commercial aviation as described in e.g. [40, 47, 49], see also Chapter 2. The Mixed-Integer Linear Programming (MILP) technique [46] is used and solved using a linear programming solver, e.g. CPLEX [64].

Decision Variables

- Δt_e^p - Time that eVTOL p is scheduled before its $ETA^p(A)$ or $ETA^p(B)$ at the chosen approach fix, defined as $|ETA^p(A/B) - RTA(A/B)|$
- Δt_l^p - Time that eVTOL p is scheduled after its $ETA^p(A)$ or $ETA^p(B)$ at the chosen approach fix, defined as $|RTA^p(A/B) - ETA(A/B)|$
- a^p - 1 if eVTOL p flies through approach fix A, 0 if it flies through approach fix B
- s^{pq} - 1 if eVTOL p arrives prior to eVTOL q, 0 if q arrives prior to q
- z^{pq} - 1 if eVTOL p and eVTOL q fly through the same approach fix, 0 if not

Input Variables

- c_e^p - Cost for eVTOL p to be early
- c_l^p - Cost for eVTOL p to be late by flying shallow descent
- $c_{l,af}^p$ - Cost for eVTOL p to be late from flying through approach fix A compared to approach fix B
- Δt_{sep}^{pq} - Required time separation for aircraft p followed by aircraft q
- K - Maximum eVTOL position shift with respect to FCFS sequence
- $ETA^p(A)$,$ETA^p(B)$ - Estimated Time of Arrival of eVTOL p at approach fix A, B
- $T_t^p(A)$, $T_t^p(B)$ - Transfer Time between approach fix A,B and the vertiport landing pad for aircraft p
- RTA_e^p, RTA_l^p - Earliest, Latest possible Required Time of Arrival of eVTOL p at the vertiport
- $\Delta t_{l,A}^p$, $\Delta t_{l,B}^p$ - Time in minutes that eVTOL p arrives late at the vertiport due to the choice for approach fix A, B
- M^{pq} - Big-M scalar for aircraft p and q

Objective function

$$min \qquad \sum_{p\in G} c_e^p \cdot \Delta t_e^p + c_l^p \cdot \Delta t_l^p + c_{l,af}^p \cdot a^p \cdot (\Delta t_{l,A}^p - \Delta t_{l,B}^p) \tag{4.12}$$

$$\Delta t_{l,A}^p = max\big(0, (ETA^p(A) + T_t^p(A) - ETA^p(B) - T_t^p(B))\big) \tag{4.13}$$

$$\Delta t_{l,B}^p = max\big(0, (ETA^p(B) + T_t^p(B) - ETA^p(A) - T_t^p(A))\big) \tag{4.14}$$

Equation 4.12 shows the objective function for this research, which optimises the rescheduling of eVTOLs by landing them earlier or delaying them with respect to their ETA for minimum total delay. The total delay results from alternating shallow descent trajectory prior to the arrival fix and rerouting through a different approach fix. The latter is calculated by Equations 4.13 and 4.14.

Constraints

$$s^{pq} = \{0,1\} \qquad \forall p \in G, q \in [p-K, p+K], p \neq q \tag{4.15}$$

$$z^{pq}, a^p = \{0,1\} \qquad \forall p, q \in G \tag{4.16}$$

$$\Delta t_e^p, \Delta t_l^p \geq 0 \qquad \forall p, q \in G \tag{4.17}$$

$$s^{pq} + s^{qp} = 1 \qquad \forall p, q \in G \tag{4.18}$$

$$z^{pq} = z^{qp} \qquad \forall p, q \in G \tag{4.19}$$

$$z^{pq} \geq a^p + a^q - 1 \qquad \forall p, q \in G, p \neq q \tag{4.20}$$

$$z^{pq} \geq -a^p - a^q + 1 \qquad \forall p, q \in G, p \neq q \tag{4.21}$$

$$z^{pq} \leq \frac{1}{2}a^p - \frac{1}{2}a^q + 1 \qquad \forall p, q \in G, p \neq q \tag{4.22}$$

$$z^{pq} \leq -\frac{1}{2}a^p + \frac{1}{2}a^q + 1 \qquad \forall p, q \in G, p \neq q \tag{4.23}$$

$$RTA_e^p \leq RTA^p \leq RTA_l^p \qquad \forall p \in G \tag{4.24}$$

$$RTA^p \geq RTA^q + \Delta t_{sep}^{qp} - M^{pq} \cdot s^{pq} \qquad \forall p, q \in G, p \neq q \tag{4.25}$$

$$RTA^p(A) \geq RTA^q(A) + \Delta t_{sep}^{qp} \cdot z^{qp} - M^{pq} \cdot s^{pq} \qquad \forall p, q \in G, p \neq q \tag{4.26}$$

$$RTA^p(B) \geq RTA^q(B) + \Delta t_{sep}^{qp} \cdot z^{qp} - M^{pq} \cdot s^{pq} \qquad \forall p, q \in G, p \neq q \tag{4.27}$$

in which

$$M^{pq} = RTA_l^q + \Delta t_{sep}^{qp} - RTA_e^p \tag{4.28}$$

$$RTA^p = ETA^p(B) + T_t^p(B) + a^p \cdot \big(ETA^p(A) + T_t^p(A) - ETA^p(B) - T_t^p(B)\big) + \Delta t_l^p - \Delta t_e^p \tag{4.29}$$

$$RTA^p(A) = ETA^p(A) + \Delta t_l^p - \Delta t_e^p \tag{4.30}$$

$$RTA^p(B) = ETA^p(B) + \Delta t_l^p - \Delta t_e^p \tag{4.31}$$

Here, Equation 4.15 allows only the sequencing parameters within the Constrained Position Shifting window to adapt from the FCFS sequence by maximum position shift K. Equation 4.16 and 4.17 cover the type and limit of the other decision variables. Equation 4.18 ensures a realistic solution by forcing one aircraft prior to the other. Besides, Equation 4.19 states that if aircraft p and q go through the same approach fix, the reversed is also true. The same variable is defined in Equations 4.20 and 4.21, setting z^{pq} to '1' or 'true' if both aircraft pass through the same approach fix. Equations 4.22 and 4.23 are similar but now force z^{pq} to '0' or 'false' if both aircraft fly through a different approach fix. The time window available for landing at the vertiport is described in Equation 4.24 based on the feasible arrival trajectories and battery prediction framework. Furthermore, Equations 4.25, 4.26 and 4.27 ensure time-based separation at the vertiport, approach fix A and approach fix B, respectively. At last, Equation 4.28 shows the calculation for the Big-M parameter and Equation 4.29, 4.30 and 4.31 define the RTA at the vertiport, approach fix A and approach fix B, respectively.

4.4.1. Objective of eVTOL Arrival Sequencing & Scheduling for Single Landing Pad

The objective of this study is to minimise total delay for all aircraft while considering energy-efficient trajectories. A minimum total delay objective is chosen because the main goal of Urban Air Mobility is to reduce travel time compared to ground transport. Besides, the limited eVTOL battery capacity requires us to reduce the flight time to save energy [5]. In this research, delay is described as the difference between the Estimated Time of Arrival (ETA) and the Required Time of Arrival (RTA) at the vertiport. Delay can be absorbed by 1) flying a shallow descent towards the vertiport, 2) flying a detour towards a further approach fix or only if necessary 3) hover at the TMA border. The ETA is calculated before scheduling and based on the most energy-optimal trajectory for eVTOL arrival, while the RTA is the output of the sequencing and scheduling algorithm as described by Equation 4.29. The objective function is mathematically described in Equation 4.32. For some eVTOL types, arriving earlier than the ETA is feasible while being less energy efficient, e.g. using gliding [28]. The objective function thus considers both an early and a late arrival parameter, Δt_e^p and Δt_l^p respectively. It also considers the cost of flying through the less efficient approach fix, explained by Equation 4.33 and 4.34.

$$min \qquad \sum_{p \in G} c_e^p \cdot \Delta t_e^p + c_l^p \cdot \Delta t_l^p + c_{l,af}^p \cdot a^p \cdot (\Delta t_{l,A}^p - \Delta t_{l,B}^p) \tag{4.32}$$

$$\Delta t_{l,A}^p = max\big(0, (ETA^p(A) + T_t^p(A) - ETA^p(B) - T_t^p(B))\big) \tag{4.33}$$

$$\Delta t_{l,B}^p = max\big(0, (ETA^p(B) + T_t^p(B) - ETA^p(A) - T_t^p(A))\big) \tag{4.34}$$

Definition of Cost Function

The cost parameters (c_e^p, c_l^p, $c_{l,AF}^p$) in this objective are used to both penalise a scheduled delay and prioritise one delay absorption method over the other. For the EHANG-184, absorption of delay in shallow descent flight is more energy-efficient than taking a detour at cruise altitude to a further approach fix. Therefore, the cost parameters in this research are energy-based. Cost c_e^p and c_l^p depict the battery energy drawn per second, thus the battery power demand P_d of flying one second less or extra in shallow descent. Cost $c_{l,AF}^p$ is determined by the battery energy draw per second, thus the battery power demand P_d in cruise flight. The P_r for both purposes can be obtained from the flight dynamics module in Section 4.2 and converted to P_d using Equation 4.8 in Section 4.3.

4.4.2. Constraints of eVTOL Arrival Sequencing & Scheduling for Single Landing Pad

This section discusses the constraints of the linear programming problem for eVTOL arrival sequencing and scheduling using a single landing pad as shown in Equation 4.12 till 4.31.

Constrained Position Shifting

Constrained Position Shifting (CPS) [22, 58] reduces the number of positions the eVTOL arrival sequence can be alternated from the fist-come-first-serve (FCFS) sequence. This thus also reduces the number of decision variables and increases the computational efficiency. Their FCFS sequence is obtained based on the ETA at the vertiport and the s^{pq} matrix is built with ones (p prior to q) and zeros (q prior to p) using this sequence. Afterwards, the parameters within the maximum allowed position shift K are allowed to be adapted to either 1 or 0 as described in Equation 4.35. The other time-based decision variables Δt are forced to be larger than 0 and binary decision variables z^{pq}, a^p like s^{pq} forced to be either 1 or 0.

$$s^{pq} = \{0, 1\} \qquad \forall p \in G, q \in [p-K, p+K], p \neq q \tag{4.35}$$

Choice of Approach Fix

As the ConOps uses two approach fixes at the boundaries of the Final Approach Area, constraints must be added that ensure the feasible and most optimal choice of approach fix for each aircraft. Besides, eVTOLs that fly through the same approach fix needs to be separated at this stage of flight, such that binary parameter z^{pq} is defined (1 if same approach fix, 0 if not).

$$z^{pq} = z^{qp} \qquad \forall p, q \in G \tag{4.36}$$

$$z^{pq} \geq a^p + a^q - 1 \qquad \forall p, q \in G, p \neq q \tag{4.37}$$

$$z^{pq} \geq -a^p - a^q + 1 \qquad \forall p, q \in G, p \neq q \tag{4.38}$$

$$z^{pq} \leq \frac{1}{2}a^p - \frac{1}{2}a^q + 1 \qquad \forall p, q \in G, p \neq q \tag{4.39}$$

$$z^{pq} \leq -\frac{1}{2}a^p + \frac{1}{2}a^q + 1 \qquad \forall p, q \in G, p \neq q \tag{4.40}$$

As discussed in the model overview, Equation 4.36 defines the z^{pq} parameter to be equal for both aircraft p and q. Equations 4.37 - 4.40 force z^{pq} to the correct value based on the decision for a^p for both aircraft p and q. The proof of these constraints is given in Table 4.1 for each possible case.

Table 4.1: Proof of Approach Fix Constraints

	Case 1	**Case 2**	**Case 3**	**Case 4**
a^p, a^q	1,1	0,0	1,0	0,1
$z_{pq} \geq \ldots$	**1**	-1	0	0
$z_{pq} \geq \ldots$	-1	**1**	0	0
$z_{pq} \leq \ldots$	1	1	2	**0.5**
$z_{pq} \leq \ldots$	1	1	**0.5**	2

- Case 1 - Both aircraft (p,q) go through approach fix A such that $a^p = a^q = 1$. Therefore, Equation 4.37 forces z^{pq} to 1 while the other equations do not constrain the result.
- Case 2 - Both aircraft (p,q) go through approach fix B such that $a^p = a^q = 0$. Therefore, Equation 4.38 forces z^{pq} to 1 while the other equations do not constrain the result.
- Case 3 - Aircraft p goes through approach fix A and aircraft q through approach fix B such that $a^p = 1$ and $a^q = 0$. Therefore, Equation 4.40 together with the binary property forces z^{pq} to 0 while the other equations do not constrain the result.
- Case 4 - Aircraft p goes through approach fix B and aircraft q through approach fix A such that $a^q = 1$ and $a^p = 0$. Therefore, Equation 4.39 together with the binary property forces z^{pq} to 0 while the other equations do not constrain the result.

Required Time of Arrival Window

The time of arrival of an eVTOL at the approach fix is limited by its flight performance capabilities and its remaining battery as discussed in Section 4.2 and 4.3, respectively. To determine the earliest possible RTA at the vertiport (RTA_e^p), the energy-efficient arrival trajectory model using GPOPS-II software is advised, while the latest possible RTA at the vertiport (RTA_l^p) is computed in the battery model. Both are added as a constraint, see again Equation 4.41. As the input model generates the ETA for approach fix A and approach fix B, RTA_e^p and RTA_l^p are determined by Equations 4.42 and 4.43, respectively.

$$RTA_e^p \leq RTA^p \leq RTA_l^p \qquad \forall p \in G \tag{4.41}$$

$$RTA_e^p = min\left(RTA_e^p(A) + T_t^p(A), RTA_e^p(B) + T_t^p(B)\right) \tag{4.42}$$

$$RTA_l^p = min\left(RTA_l^p(A) + T_t^p(A), RTA_l^p(B) + T_t^p(B)\right) \tag{4.43}$$

Using Equation 4.44, the RTA window constraint can be rewritten as input for the MILP with decision variables and their lower and upper boundaries. Besides, all constraints are written as $Ax \leq b$ such that matrix b contains the constraint upper limits. Therefore, the RTA window constraint from Equation 4.41 with all decision variables is split and written as in Equations 4.45 and 4.46.

$$\begin{aligned} RTA^p &= a^p \cdot \left(RTA^p(A) + T_t^p(A)\right) + (1 - a^p) \cdot \left(RTA^p(B) + T_t^p(B)\right) \\ &= a^p \cdot \left(ETA^p(A) + T_t^p(A)\right) + (1 - a^p) \cdot \left(ETA^p(B) + T_t^p(B)\right) + \Delta t_l^p - \Delta t_e^p \\ &= ETA^p(B) + T_t^p(B) + a^p \cdot \left(ETA^p(A) + T_t^p(A) - ETA^p(B) - T_t^p(B)\right) + \Delta t_l^p - \Delta t_e^p \end{aligned} \tag{4.44}$$

$$a^p \cdot \left(ETA^p(A) + T_t^p(A) - ETA^p(B) - T_t^p(B)\right) + \Delta t_l^p - \Delta t_e^p \leq RTA_l^p - (ETA^p(B) + T_t^p(B)) \qquad \forall p \in G \tag{4.45}$$

$$-a^p \cdot \left(ETA^p(A) + T_t^p(A) - ETA^p(B) - T_t^p(B)\right) - \Delta t_l^p + \Delta t_e^p \leq -RTA_e^p + (ETA^p(B) + T_t^p(B)) \qquad \forall p \in G \tag{4.46}$$

Time Separation

The most important constraint in the arrival sequencing and scheduling model is the time separation requirement which forces the following eVTOL to ensure sufficient separation from the leading eVTOL based on the computed landing sequence. This constraint can be written as follows in Equation 4.47 at the vertiport and Equation 4.48 and 4.49 at approach fix A and B, respectively. It uses the Big-M method, thus the Big-M parameter M^{pq} in Equation 4.50 to ensure convergence.

$$RTA^p \geq RTA^q + \Delta t_{sep}^{qp} - M^{pq} \cdot s^{pq} \qquad \forall p, q \in G \tag{4.47}$$

$$RTA^p(A) \geq RTA^q(A) + \Delta t_{sep}^{qp} \cdot z^{qp} - M^{pq} \cdot s^{pq} \qquad \forall p, q \in G \tag{4.48}$$

$$RTA^p(B) \geq RTA^q(B) + \Delta t_{sep}^{qp} \cdot z^{qp} - M^{pq} \cdot s^{pq} \qquad \forall p, q \in G \tag{4.49}$$

$$M^{pq} = RTA_l^q + \Delta t_{sep}^{qp} - RTA_e^p \tag{4.50}$$

Again using Equation 4.44, the equations above can be rewritten in a format ready for the MILP calculations. These relations are depicted in Equation 4.51 till 4.53.

$$\begin{aligned} a^p \cdot \left(ETA^p(A) + T_t^p(A)\right) + (1 - a^p) \cdot \left(ETA^p(B) + T_t^p(B)\right) + \Delta t_l^p - \Delta t_e^p - a^q \cdot \left(ETA^q(A) + T_t^q(A)\right) \\ -(1 - a^q) \cdot \left(ETA^q(B) + T_t^q(B)\right) - \Delta t_l^q + \Delta t_e^q + M^{pq} \cdot s^{pq} \geq \Delta t_{sep}^{qp} \qquad \forall p, q \in G \end{aligned} \tag{4.51}$$

$$\Delta t_l^p - \Delta t_e^p - \Delta t_l^q + \Delta t_e^q - \Delta t_{sep}^{qp} \cdot z^{qp} + M^{pq} \cdot s^{pq} \geq ETA^q(A) - ETA^p(A) \qquad \forall p, q \in G \tag{4.52}$$

$$\Delta t_l^p - \Delta t_e^p - \Delta t_l^q + \Delta t_e^q - \Delta t_{sep}^{qp} \cdot z^{qp} + M^{pq} \cdot s^{pq} \geq ETA^q(B) - ETA^p(B) \qquad \forall p, q \in G \tag{4.53}$$

To proof the mathematical formulation of the time separation constraints, each scenario for decision variables z_{pq} and s_{pq} is worked out in 4 cases.

- Case 1 - Aircraft p and q go through different approach fixes such that $z_{pq} = 0$. Also, aircraft p arrives behind aircraft q at the vertiport, so $s_{pq} = 0$. Equation 4.48 can be reduced such that the RTA at the vertiport for aircraft p is greater than the RTA of q (see Equation 4.56), which corresponds to $s_{pq} = 0$. Equation 4.47 reduces to a similar equation but adds the time separation requirement as shown in 4.57.

$$RTA^p(A) \geq RTA^q(A) \tag{4.54}$$

$$RTA^p - T_t(A) \geq RTA^q - T_t(A) \tag{4.55}$$

$$RTA^p \geq RTA^q \tag{4.56}$$

$$RTA^p \geq RTA^q + \Delta t_{sep}^{qp} \tag{4.57}$$

- Case 2 - Aircraft p and q go through the same approach fix such that $z_{pq} = 1$. Also, aircraft p arrives behind aircraft q at the vertiport, so $s_{pq} = 0$. Equation 4.48 is again reduced such that the RTA at the vertiport for aircraft p is greater than the RTA of q (see Equation 4.60) including the time separation, which corresponds to $s_{pq} = 0$. Equation 4.47 reduces to the same equation as shown in 4.61 and thus forces separation.

$$RTA^p(A) \geq RTA^q(A) + \Delta t_{sep}^{qp} \tag{4.58}$$

$$RTA^p - T_t(A) \geq RTA^q - T_t(A) + \Delta t_{sep}^{qp} \tag{4.59}$$

$$RTA^p \geq RTA^q + \Delta t_{sep}^{qp} \tag{4.60}$$

$$RTA^p \geq RTA^q + \Delta t_{sep}^{qp} \tag{4.61}$$

- Case 3 - Aircraft p and q go through different approach fixes such that $z_{pq} = 0$. Now aircraft p arrives before aircraft q at the vertiport, so $s_{pq} = 1$. This proof uses the relation for the Big-M scalar (Equation 4.50) to reduce Equation 4.48 such that the time separation requirement is always satisfied (see Equation 4.64), which corresponds to $s_{pq} = 0$. The same equation for $s_{qp} = 1$ as discussed in case 2 will force the separation between the aircraft anyway for the reversed sequence. Equation 4.47 reduces to a similar satisfied equation as shown in 4.67.

$$RTA^p(A) \geq RTA^q(A) - M^{pq} \tag{4.62}$$

$$RTA^p - T_t(A) \geq RTA^q - T_t(A) - \left(RTA_l^q + \Delta t_{sep}^{qp} - RTA_e^p\right) \tag{4.63}$$

$$RTA^p - RTA_e^p (\geq 0) \geq RTA^q - \Delta t_{sep}^{qp} - RTA_l^q (\leq 0) \tag{4.64}$$

$$RTA^p \geq RTA^q + \Delta t_{sep}^{qp} - M^{pq} \tag{4.65}$$

$$RTA^p \geq RTA^q + \Delta t_{sep}^{qp} - \left(RTA_l^q + \Delta t_{sep}^{qp} - RTA_e^p\right) \tag{4.66}$$

$$RTA^p - RTA_e^p (\geq 0) \geq RTA^q - RTA_l^q (\leq 0) \tag{4.67}$$

- Case 4 - Aircraft p and q go through the same approach fix such that $z_{pq} = 1$. Again aircraft p arrives before aircraft q at the vertiport, so $s_{pq} = 1$. This proof also uses the relation for the Big-M scalar (Equation 4.50) and shows the same outcome as in case 3. Equations 4.70 and 4.73 are again always satisfied, which is correct as the aircraft fly in reversed sequence and through a different approach fix.

$$RTA^p(A) \geq RTA^q(A) + \Delta t_{sep}^{qp} - M^{pq} \tag{4.68}$$

$$RTA^p - T_t(A) \geq RTA^q - T_t(A) + \Delta t_{sep}^{qp} - \left(RTA_l^q + \Delta t_{sep}^{qp} - RTA_e^p\right) \tag{4.69}$$

$$RTA^p - RTA_e^p (\geq 0) \geq RTA^q - RTA_l^q (\leq 0) \tag{4.70}$$

$$RTA^p \geq RTA^q + \Delta t_{sep}^{qp} - M^{pq} \tag{4.71}$$

$$RTA^p \geq RTA^q + \Delta t_{sep}^{qp} - \left(RTA_l^q + \Delta t_{sep}^{qp} - RTA_e^p\right) \tag{4.72}$$

$$RTA^p - RTA_e^p (\geq 0) \geq RTA^q - RTA_l^q (\leq 0) \tag{4.73}$$

4.4.3. Variations to eVTOL Arrival Sequencing & Scheduling Model for Single Landing Pad

Without any efficient solver technique or reduction in decision variables, the number of decision variables is calculated using Equation 4.74. As observed, the number of DVs grows rapidly with the number of eVTOLs in the observation period G. This is computationally expensive while arrival sequencing and scheduling cannot be performed in the far future due to the on-demand characteristic of UAM. Furthermore, this on-demand arrival could lead to high peak arrival periods such that delay cannot be absorbed only using shallow descent and approach fix detour anymore. This section, therefore, looks into model variations that 1) increase the computational efficiency by using a simplified formulation without z_{pq}, a branch-and-bound solver and a rolling horizon technique and 2) increase the delay absorption capacity by applying column generation for hover.

$$DV = 3 \cdot G + G^2 + G \cdot (2 \cdot K + 1) \tag{4.74}$$

Simplified Model Formulation

When the two approach fixes are located at an equal distance from the vertiport and one eVTOL type is operated, the proposed model formulation can be simplified to reduce the number of decision variables and constraints. In this case it can be assumed that the travel time from both approach fixes for each eVTOL is equal, such that $T_t^p(A) = T_t^p(B)$ and $T_t^p(A) = T_t^q(A)$. Therefore, eVTOLs are separated already at the approach fix if they are separated at the vertiport. This allows leaving out the constraints that ensure separation at the approach fix, see Equation 4.26 and 4.27 (Section 4.4). Resulting from this, the parameter z_{pq} is unused throughout the model and Equation 4.19 till 4.23 can be left out. This leads to an improved computational efficiency and a formulation as shown in Equation 4.75 till 4.81. To compute the Big-M parameter and RTA^p, Equations 4.82 and 4.83 again apply.

$$
\begin{aligned}
min \quad & \sum_{p \in G} c_e^p \cdot \Delta t_e^p + c_l^p \cdot \Delta t_l^p + c_{l,af}^p \cdot a^p \cdot (\Delta t_{l,A}^p - \Delta t_{l,B}^p) && && (4.75) \\
s.t. \quad & s^{pq} = \{0,1\} && \forall p \in G, q \in [p-K, p+K], p \neq q && (4.76) \\
& a^p = \{0,1\} && \forall p,q \in G && (4.77) \\
& \Delta t_e^p, \Delta t_l^p \geq 0 && \forall p,q \in G && (4.78) \\
& s^{pq} + s^{qp} = 1 && \forall p,q \in G && (4.79) \\
& RTA_e^p \leq RTA^p \leq RTA_l^p && \forall p \in G && (4.80) \\
& RTA^p \geq RTA^q + \Delta t_{sep}^{qp} - M^{pq} \cdot s^{pq} && \forall p,q \in G, p \neq q && (4.81)
\end{aligned}
$$

in which

$$
\begin{aligned}
M^{pq} &= RTA_l^q + \Delta t_{sep}^{qp} - RTA_e^p && (4.82) \\
RTA^p &= ETA^p(B) + T_t^p(B) + a^p \cdot \left(ETA^p(A) + T_t^p(A) - ETA^p(B) - T_t^p(B)\right) + \Delta t_l^p - \Delta t_e^p && (4.83)
\end{aligned}
$$

Branch-and-Bound Solver

The branch-and-bound solver technique is used to solve MILPs for increased computational efficiency [46, 47]. It searches the best solution (bound) of each subproblem (relaxation) while adding integer constraints (branching) to the decision variables during each iteration. The solution to each subproblem is tested based on fathoming tests: 1) the solution is less optimal than the solution to another subproblem ($Z \leq Z^*$), 2) there is no feasible solution ($Z = \emptyset$) and 3) the solution is integer ($Z^* = Z$). If any of the three fathoming tests is true for the observed subproblem, the branching is exited. The following summarises the steps in the branch-and-bound algorithm:

1. *Initialisation* of the model is done by solving the complete MILP without integer constraints (MILP relaxation), e.g. binary decision variables can take any value between 0 and 1. If all fathoming tests are false, this becomes the first subproblem.
2. *Iterations* are executed until optimality is reached:
   (a) *Branching* is then performed on the decision variable with the solution furthest away from integer (e.g. 0.5000), the node. Two new subproblems are created from this node by adding one new constraint to each subproblem which force the node to round towards the lower integer and higher integer, respectively (e.g. ≤ 0 and ≥ 1).
   (b) *Bounding* is done after solving the LP relaxation of the subproblem. The solution Z is the bound for each subproblem, so for each branch.
   (c) *Fathoming* is performed by applying the fathoming tests to each new subproblem, such that suboptimal (1) and infeasible solutions (2) are dismissed or integer solutions are set to the new optimal (Z^*)(3).
3. *Optimality* is reached when no more unfathomed subproblems are available. The optimal integer solution is Z^*.

Rolling Horizon Solver

The main application of the rolling horizon approach in commercial aviation is to solving dynamic scheduling problems in which the planning horizon includes uncertainty. This uncertainty is larger for aircraft further from the airport or further from departure, such that the landing or departure time should be frozen or determined as close to landing or departure as possible. In this eVTOL arrival sequencing and scheduling problem, however, the rolling horizon algorithm will be used to increase the computational efficiency by cutting the problem into smaller pieces. Therefore, an optimisation and influence window as proposed in [22] is used as illustrated in Figure 4.4. This timeline is depicted as an observation from one single eVTOL at the start of the approach phase until the final landing at the vertiport. When an eVTOL is 'flying' in the optimisation window, its arrival time is computed based on all other eVTOLs in the optimisation and influence window. The resulting schedule is thus influenced by the eVTOLs in the influence window.

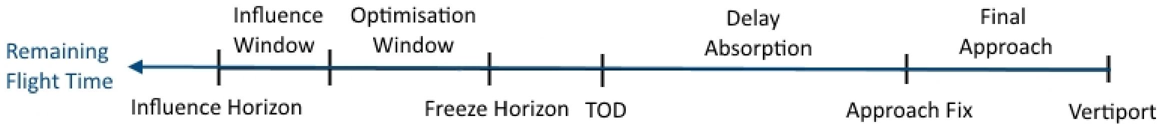

Figure 4.4: Time Horizon for eVTOL Arrival at a Vertiport

Figure 4.5 shows the rolling horizon framework which is obtained and adapted from [65]. Other than Figure 4.4, this image is an observation from the air traffic control perspective. The planning horizon in this observation includes all eVTOLs flying through the optimisation window and influence window, while the planning period contains all eVTOLs in the optimisation window. The freeze horizon for each eVTOL is similar to $T(k+1)$, the time at which the optimisation window for an eVTOL ends and the planning period is moved to the next time step k. The time step $T(k) - T(k+1)$ is set to 15 minutes to allow for optimal sequencing and scheduling for a reasonable computational efficiency. The number of planning periods included in the planning horizon N is set to 2 for this scheduler other than 3 as depicted in this figure [51, 52]. Due to the on-demand service of UAM and the limited delay absorption options, looking further into the future does not change the results from the scheduler when using rolling horizon.

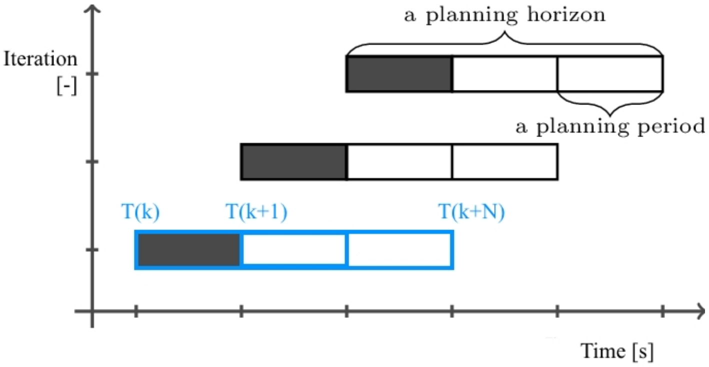

Figure 4.5: Rolling Horizon Framework for eVTOL Arrival Sequencing and Scheduling [65]

To implement the rolling horizon framework into the eVTOL arrival sequencing and scheduling tool, the algorithm in Figure 4.6 is used. This figure also shows that the RTA of the last eVTOL landing in the frozen planning periods RTA_{last} is saved to ensure separation between approaching eVTOL p and the eVTOLs scheduled in the last planning horizon. This is done via $RTA^{p}_{e,RH}$ in the RTA window constraint (repeated in Equation 4.84) using Equations 4.85, 4.86 and 4.87. The earliest landing time of eVTOL p is thus either set according to the last eVTOL landing or to the feasible approach based on flight performance. The remainder of the eVTOL sequencing and scheduling model using a single landing pad is similar to the model explained in Equation 4.12 till 4.31 in the beginning of this section.

$$RTA^{p}_{e} \leq RTA^{p} \leq RTA^{p}_{l} \qquad \forall p \in G \tag{4.84}$$

$$RTA^{p}_{e,RH}(A) = max\left(RTA_{last}(A) + \Delta t^{pq}_{sep}, RTA^{p}_{e}(A)\right) \tag{4.85}$$

$$RTA^{p}_{e,RH}(B) = max\left(RTA_{last}(B) + \Delta t^{pq}_{sep}, RTA^{p}_{e}(B)\right) \tag{4.86}$$

$$RTA^{p}_{e} = min\left(RTA^{p}_{e,RH}(A) + T^{p}_{t}(A), RTA^{p}_{e,RH}(B) + T^{p}_{t}(B)\right) \tag{4.87}$$

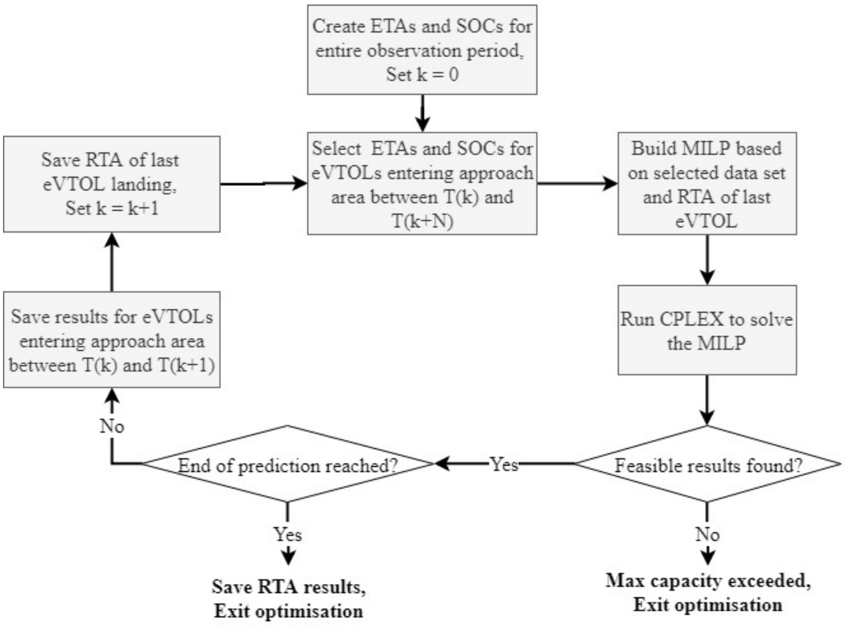

Figure 4.6: Rolling Horizon Algorithm adapted from [51]

Column Generation for Hover

A problem encountered in some eVTOL arrival sets is that it exceeds the maximum capacity of the model and the ConOps. Therefore, two solutions were proposed in Chapter 3: hover at the border of the approach area and usage of a second landing pad. The latter is discussed in more detail in Section 4.5. Only if a data set is infeasible, the hover option is enabled for the eVTOL that has the most remaining battery. Hover is thus added to the current model formulation using column generation. The linear formulation is extended with one decision variable indicating the time waiting in hover $t_{l,h}^p$ on the terminal boundary at cruise altitude. Hover options, thus decision variables, are added until a feasible solution is found or no eVTOLs with sufficient battery power remaining are available. Equation 4.88 till 4.101 shows the model formulation for eVTOL arrival sequencing and scheduling using a single landing pad including hover.

$$min \quad \sum_{p\in G} c_e^p \cdot \Delta t_e^p + c_l^p \cdot \Delta t_l^p + c_{l,af}^p \cdot a^p \cdot (\Delta t_{l,A}^p - \Delta t_{l,B}^p) + c_{l,h}^p \cdot \Delta t_{l,h}^p \tag{4.88}$$

$$s.t. \quad s^{pq} = \{0,1\} \qquad \forall p \in G, q \in [p-K, p+K], p \neq q \tag{4.89}$$

$$z^{pq}, a^p = \{0,1\} \qquad \forall p,q \in G \tag{4.90}$$

$$\Delta t_e^p, \Delta t_l^p, \Delta t_{l,h}^p \geq 0 \qquad \forall p,q \in G \tag{4.91}$$

$$s^{pq} + s^{qp} = 1 \qquad \forall p,q \in G \tag{4.92}$$

$$z^{pq} = z^{qp} \qquad \forall p,q \in G \tag{4.93}$$

$$z^{pq} \geq a^p + a^q - 1 \qquad \forall p,q \in G, p \neq q \tag{4.94}$$

$$z^{pq} \geq -a^p - a^q + 1 \qquad \forall p,q \in G, p \neq q \tag{4.95}$$

$$z^{pq} \leq \frac{1}{2} a^p - \frac{1}{2} a^q + 1 \qquad \forall p,q \in G, p \neq q \tag{4.96}$$

$$z^{pq} \leq -\frac{1}{2} a^p + \frac{1}{2} a^q + 1 \qquad \forall p,q \in G, p \neq q \tag{4.97}$$

$$RTA_e^p \leq RTA^p \leq RTA_l^p \qquad \forall p \in G \tag{4.98}$$

$$RTA^p \geq RTA^q + \Delta t_{sep}^{qp} - M^{pq} \cdot s^{pq} \qquad \forall p,q \in G, p \neq q \tag{4.99}$$

$$RTA^p(A) \geq RTA^q(A) + \Delta t_{sep}^{qp} \cdot z^{qp} - M^{pq} \cdot s^{pq} \qquad \forall p,q \in G, p \neq q \tag{4.100}$$

$$RTA^p(B) \geq RTA^q(B) + \Delta t_{sep}^{qp} \cdot z^{qp} - M^{pq} \cdot s^{pq} \qquad \forall p,q \in G, p \neq q \tag{4.101}$$

The Big-M parameter now also includes the maximum time eVTOL q can spend in hover $\Delta t^{q}_{l,h,max}$ which is shown in Equation 4.102. Besides, the computation of the RTA, RTA(A) and RTA(B) change according to Equation 4.103 to 4.105. This thus affects the RTA window constraint in Equation 4.98 and time separation constraints in Equation 4.99 till 4.101. The constraints can be written in detail with all decision variables as described in Subsection 4.4.2 in which Δt^{p}_{l} and $\Delta t^{p}_{l,h}$ are treated similarly.

$$M^{pq} = RTA^{q}_{l} + \Delta t^{q}_{l,h,max} + \Delta t^{qp}_{sep} - RTA^{p}_{e} \tag{4.102}$$

$$RTA^{p} = ETA^{p}(B) + T^{p}_{t}(B) + a^{p} \cdot \left(ETA^{p}(A) + T^{p}_{t}(A) - ETA^{p}(B) - T^{p}_{t}(B)\right) + \Delta t^{p}_{l} - \Delta t^{p}_{e} + \Delta t^{p}_{l,h} \tag{4.103}$$

$$RTA^{p}(A) = ETA^{p}(A) + \Delta t^{p}_{l} - \Delta t^{p}_{e} + \Delta t^{p}_{l,h} \tag{4.104}$$

$$RTA^{p}(B) = ETA^{p}(B) + \Delta t^{p}_{l} - \Delta t^{p}_{e} + \Delta t^{p}_{l,h} \tag{4.105}$$

The cost of hovering $c^{p}_{l,h}$ is determined similar to the cost of absorbing delay in shallow descent and the cost to fly a detour, thus based on the battery power demand in hover $P_{d,hover}$. To compute this, the flight dynamics from Section 4.2 are again advised. However, the climb, parasite and profile power can be assumed equal to zero in hover. Besides, the induced velocity v_i can be set equal to the induced velocity in hover v_h and the total thrust T to the eVTOL weight W (mass m multiplied by the gravitational acceleration g) in hover. This results in the computations for $P_{r,hover}$ as shown in Equation 4.106 and converted to $P_{d,hover}$ using Equation 4.8 and a SOC demand per second using Equation 4.11, both from Section 4.3. This SOC draw is used to compute $\Delta t^{q}_{l,h,max}$ based on the eVTOL initial SOC and the SOC required for maximum delay absorption in shallow descent or approach fix diversion.

$$P_{r,hover} = 4 \cdot T \cdot v_i = 4 \cdot \frac{1}{4} W \cdot v_h = m \cdot g \sqrt{\frac{T_r}{2\rho\pi R^2}} \tag{4.106}$$

4.5. Module 3 - eVTOL Arrival Sequencing & Scheduling Model for Double Landing Pad

For high demand peaks and low battery cases, the proposed single landing pad ConOps and model formulation including hover still does not provide sufficient delay absorption possibilities. This indicates that the maximum landing capacity is reached and thus an alternative ConOps using two landing pads at one vertiport is used as described in Section 3.2. A second landing funnel is added to allow for a direct landing of an eVTOL at landing pad A if approaching through approach fix A and at landing pad B if approaching through approach fix B. This section describes the eVTOL arrival sequencing and scheduling model for a double landing pad ConOps as depicted in Equation 4.107 till 4.124.

The minimal delay objective function and other constraints in the eVTOL arrival sequencing and scheduling model remain the same compared to the single landing pad model including column generation in hover. Therefore, a detailed explanation can be found in Section 4.4. Again Equation 4.108 includes the CPS for the sequencing parameter and Equations 4.109 to 4.112 ensure a realistic solution. Equation 4.113 to 4.116 define the similarity in the approach fix selection of two eVTOLs. Equation 4.117 defines the feasible arrival window at the selected landing pad based on flight dynamics and battery status and Equations 4.118, 4.119 and 4.120 ensure separation between eVTOLs that are arriving at the same landing pad, via the same approach fix A or via the same approach fix B, respectively. If simplified model conditions apply, see Subsection 4.4.3, separation at the approach fixes is also ensured by this equation. Equation 4.119 and 4.119 separate eVTOLs at the approach fixes, so can be left out, in that case.

The eVTOL arrival trajectory and procedures for a double landing pad are similar to those for a single landing pad except for the horizontal flight phase inside the Final Approach Area. Therefore, only three changes are made to the scheduler. First, the flight time between approach fix and landing pad ($T_t(A)$, $T_t(B)$) is reduced which changes the result of Equation 4.122. Second, only eVTOLs approaching through the same approach fix and thus landing at the same pad need to be separated using Equation 4.118. Third, the RTA is constraint by either the earliest possible RTA at the selected approach fix and landing pad $RTA^{p}_{e,lp}(A)$, $RTA^{p}_{e,lp}(B)$ which is added in Equation 4.117. This also influences the Big-M parameter as depicted in Equation 4.121.

$$min \quad \sum_{p \in G} c_e^p \cdot \Delta t_e^p + c_l^p \cdot \Delta t_l^p + c_{l,af}^p \cdot a^p \cdot (\Delta t_{l,A}^p - \Delta t_{l,B}^p) + c_{l,h}^p \cdot \Delta t_{l,h}^p \tag{4.107}$$

$$s.t. \quad s^{pq} = \{0,1\} \qquad \forall p \in G, q \in [p-K, p+K], p \neq q \tag{4.108}$$

$$z^{pq}, a^p = \{0,1\} \qquad \forall p,q \in G \tag{4.109}$$

$$\Delta t_e^p, \Delta t_l^p, \Delta t_{l,h}^p \geq 0 \qquad \forall p,q \in G \tag{4.110}$$

$$s^{pq} + s^{qp} = 1 \qquad \forall p,q \in G \tag{4.111}$$

$$z^{pq} = z^{qp} \qquad \forall p,q \in G \tag{4.112}$$

$$z^{pq} \geq a^p + a^q - 1 \qquad \forall p,q \in G, p \neq q \tag{4.113}$$

$$z^{pq} \geq -a^p - a^q + 1 \qquad \forall p,q \in G, p \neq q \tag{4.114}$$

$$z^{pq} \leq \frac{1}{2}a^p - \frac{1}{2}a^q + 1 \qquad \forall p,q \in G, p \neq q \tag{4.115}$$

$$z^{pq} \leq -\frac{1}{2}a^p + \frac{1}{2}a^q + 1 \qquad \forall p,q \in G, p \neq q \tag{4.116}$$

$$a^p \cdot RTA_{e,lp}^p(A) + (1-a^p) \cdot RTA_{e,lp}^p(B) \leq RTA^p \leq RTA_l^p \qquad \forall p \in G \tag{4.117}$$

$$RTA^p \geq RTA^q + \Delta t_{sep}^{qp} \cdot z^{qp} - M^{pq} \cdot s^{pq} \qquad \forall p,q \in G, p \neq q \tag{4.118}$$

$$RTA^p(A) \geq RTA^q(A) + \Delta t_{sep}^{qp} \cdot z^{qp} - M^{pq} \cdot s^{pq} \qquad \forall p,q \in G, p \neq q \tag{4.119}$$

$$RTA^p(B) \geq RTA^q(B) + \Delta t_{sep}^{qp} \cdot z^{qp} - M^{pq} \cdot s^{pq} \qquad \forall p,q \in G, p \neq q \tag{4.120}$$

in which

$$M^{pq} = RTA_l^q + \Delta t_{l,h,max}^q + \Delta t_{sep}^{qp} - min\left(RTA_{e,lp}^p(A), RTA_{e,lp}^p(B)\right) \tag{4.121}$$

$$RTA^p = ETA^p(B) + T_t^p(B) + a^p \cdot \left(ETA^p(A) + T_t^p(A) - ETA^p(B) - T_t^p(B)\right) + \Delta t_l^p - \Delta t_e^p + \Delta t_{l,h}^p \tag{4.122}$$

$$RTA^p(A) = ETA^p(A) + \Delta t_l^p - \Delta t_e^p + \Delta t_{l,h}^p \tag{4.123}$$

$$RTA^p(B) = ETA^p(B) + \Delta t_l^p - \Delta t_e^p + \Delta t_{l,h}^p \tag{4.124}$$

Rolling Horizon Solver for Double Landing Pad

A high computational time is needed to solve peak demand cases also for a double landing pad configuration. Therefore, the rolling horizon algorithm from Section 4.4.3 for the single landing pad model is applied to efficiently solve this double landing pad module. Again the RTA of the last eVTOL landing in the frozen planning periods at landing pad A ($RTA_{last,lp}(A)$) and landing pad B ($RTA_{last,lp}(B)$) is saved to ensure separation between approaching eVTOL p and the eVTOLs scheduled in the last planning horizon. Repeatedly, this is done via the RTA window constraint (Equation 4.117) using Equations 4.126 and 4.126. The eVTOL arrival sequencing and scheduling model is similar to the formulation explained above in Equation 4.107 till 4.124.

$$RTA_{e,lp}^p(A) = max\left(RTA_{last,lp}(A) + \Delta t_{sep}^{pq}, RTA_e^p(A) + T_t^p(A)\right) \tag{4.125}$$

$$RTA_{e,lp}^p(B) = max\left(RTA_{last,lp}(B) + \Delta t_{sep}^{pq}, RTA_e^p(B) + T_t^p(B)\right) \tag{4.126}$$

5

eVTOL Arrival Demand Model for Houston

At the time of writing, UAM is still a transportation mode of the future. Therefore, historical data sets are not available to test the proposed arrival eVTOL arrival sequencing and scheduling model from Chapter 4. Figure 4.1 in this chapter describes a demand estimation module, Module 4, to determine the expected arrival and battery status of each eVTOL. This chapter demonstrates how the ETAs of eVTOLs arriving at the vertiport during one day are simulated and how their initial SOC at the Terminal Area boundary is generated in Section 5.1 and Section 5.2, respectively.

5.1. Estimated Time of Arrival Simulation for eVTOL Arrivals at a Vertiport

Before the simulation of ETAs per arriving eVTOL can be performed, an expected arrival demand over a longer period of time is generated. Therefore, the eVTOL arrival demand model from [54] for Houston, TX, USA is advised. It generates a relative demand probability distribution for an entire day of eVTOL arrivals based on a hexagonal vertiport network in Houston, TX, USA, shown in Figure 5.1. The network operates a hub vertiport (vertiport 1) in the middle of the Houston business district and destinations (vertiport 2-7) in suburbs around Houston. Therefore, most arrivals are expected during commuter rush hours and none during night time, leading to the relative demand distribution as shown in Figure 5.2.

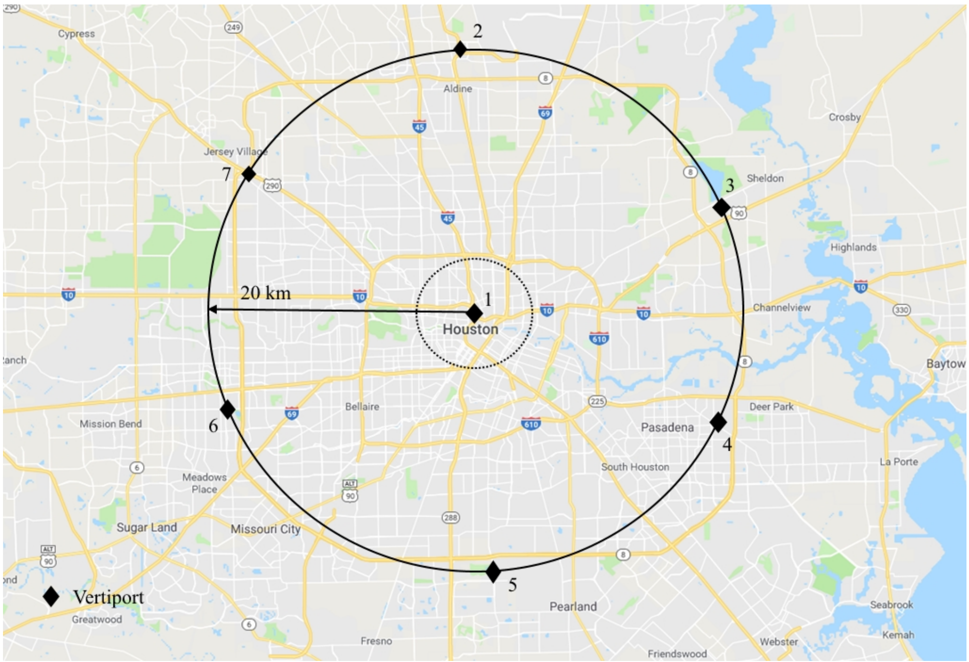

Figure 5.1: Top View of Concept of Operations for UAM in Houston

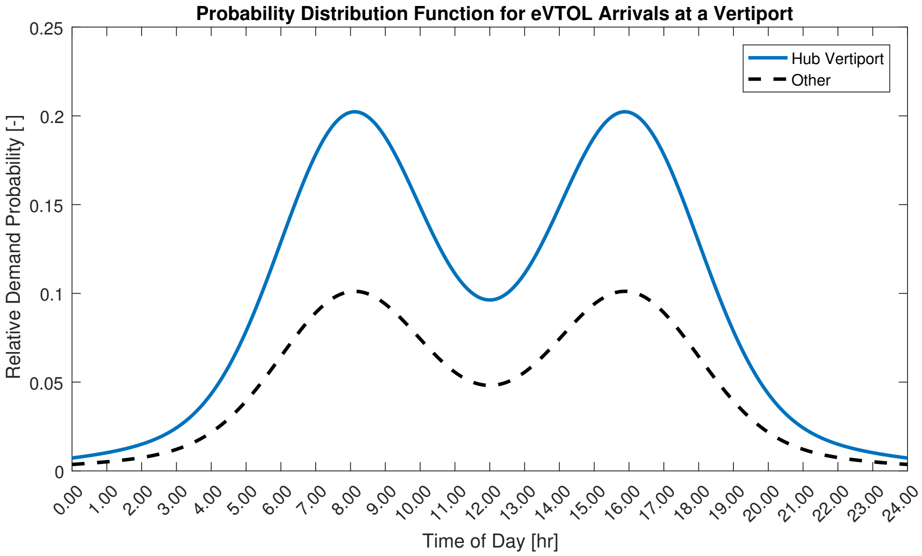

Figure 5.2: Demand Probability Function for eVTOL Arrivals in Houston, TX, USA

The demand distribution $D(t_k)$ in Figure 5.2 consists of the sum of three normal distributions (f_X) described by Equation 5.1. It models the demand for one day of 24 hours in small time steps t_k of 10 seconds. One normal distribution is centered at time step 2880 (8 AM) with a standard deviation of 2 hours $N(8,2)$, another centered at time step 5760 (4 PM) with a standard deviation of 2 hours $N(16,2)$, and a third centered at time step 4320 (noon) with a standard deviation of 6 hours $N(12,6)$. The relative magnitude of each is the same. The curve is normalised such that the cumulative distribution function (F_X) between the start and end of the day adds up to 1. Afterwards, the demand is scaled using $M_4 = 8500$ to obtain a realistic demand [54] as summarised in Equation 5.2. The vertiports in the suburbs (vertiport 2-7) are assumed to receive half of the hub (vertiport 1) demand. As this study considers a high eVTOL landing demand, the focus will be on the hub vertiport arrivals.

A stochastic simulation is performed to obtain the number of arrivals per time step t_k. For each time step of 10 seconds a random number between 0.0 and 1.0 is produced by a uniform random number generator (so $u \sim U(0,1)$). The output is compared to the demand probability function. If the number is lower than or equal to $D(t_k)$, an arrival A occurs at time step t_k as described by Equation 5.3. If the number is higher, nothing happens. The simulated arrivals are added up to obtain the expected eVTOL arrival rate per hour $\lambda(t)$ with Equation 5.4.

$$f_X(t_k) = N(8,2) + N(16,2) + N(12,6) \tag{5.1}$$

$$D(t_k) = \frac{M_4}{F_X(24) - F_X(0)} \cdot (N(8,2) + N(16,2) + N(12,6)) \tag{5.2}$$

$$u \leq D(t_k) \qquad \Rightarrow \qquad A(t_k) = 1 \tag{5.3}$$

$$\lambda(t_{start}, t_{end}) = \frac{1}{t_{end} - t_{start}} \cdot \sum_{t_{start}}^{t_{end}} A(t_k) \tag{5.4}$$

The ETA for each arriving eVTOL within time frame t_{start}, t_{end} can now be generated. The occurrence of an eVTOL arrival can then be modelled as a continuous-time discrete-state Poisson process [66]. A Poisson process considers unit jumps as e.g. an aircraft arrival always considers one entire aircraft. The arrival of eVTOLs at a vertiport is modelled as an inhomogeneous Poisson process, because the rate at which a unit jump occurs ($\lambda(t)$) differs over time. For each arriving eVTOL, an exponential random variable $S \sim exp(\lambda(t))$ is drawn based on the obtained $\lambda(t)$. This random variable indicates the time between each arrival, as depicted in Equation 5.5. If $p = 1$, the ETA is set to the first possible landing time such that the RTA window constraint can be satisfied. The generation of ETAs is terminated when the ETA of the last generation exceeds t_{end}.

$$ETA^p = ETA^{p-1} + S \qquad S \sim exp(\lambda(t)) \tag{5.5}$$

$$ETA^p(A) = ETA^p - T_t + \Delta t^p_{l,A} \tag{5.6}$$

$$ETA^p(B) = ETA^p - T_t + \Delta t^p_{l,B} \tag{5.7}$$

To assign different ETAs to approach fix A and B, the top view of the Terminal Area around vertiport 1 in Figure 5.3a is used in combination with Equations 5.6 and 5.7. The arrival direction that determines the time it takes to divert to a different vertiport $\Delta t^p_{l,AF}$ is simulated using another stochastic simulation. This simulation obtains the origin of each arriving eVTOL assuming that origin vertiport 2 till 7 are equally likely to occur. Therefore, the probability of each origin P_v becomes $\frac{1}{6}$. Using a uniform distributed random variable $w \sim U(0,1)$ draw, the origin is determined as depicted in Table 5.1.

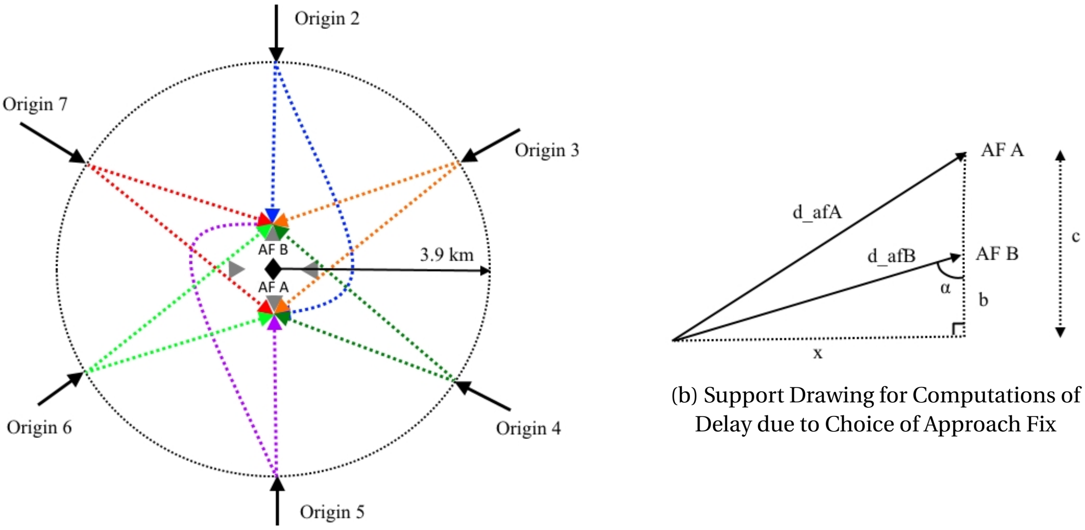

(a) Arrival Procedures for Different Approach Fixes

(b) Support Drawing for Computations of Delay due to Choice of Approach Fix

Figure 5.3: UAM Approach Procedures using Hexagon Vertiport Lay-Out

Each origin corresponds to a delay for either approach fix A or B compared to flying through the closest approach fix. This delay $\Delta t^p_{l,AF}$ is determined using Figure 5.3b and Equations 5.8 till 5.11. The equations are based on an equally divided hexagon configuration such that $\alpha \approx 60\,\text{deg}$ and $d_{afB} \approx 3500m$. Besides, $V_{cruise} = 27.8m/s$ and $R_{FA} = 400m$ can be set using EHANG-184 and the ConOps for the Final Approach Area.

$$x = d_{afB} \cdot \sin\alpha \tag{5.8}$$

$$b = d_{afB} \cdot \cos\alpha \tag{5.9}$$

$$c = b + \sqrt{R_{FA}^2 + R_{FA}^2} \tag{5.10}$$

$$\Delta t_{l,A} = \frac{d_{afA}}{V_{cruise}} = \frac{\sqrt{x^2 + c^2}}{V_{cruise}} \tag{5.11}$$

Table 5.1: Monte Carlo Simulation for Origins in Hexagon Vertiport Lay-Out

Origin	**1**	**2**	**3**	**4**	**5**	**6**	**7**
P_v	-	$\frac{1}{6}$	$\frac{1}{6}$	$\frac{1}{6}$	$\frac{1}{6}$	$\frac{1}{6}$	$\frac{1}{6}$
w	-	$[0,\frac{1}{6}]$	$[\frac{1}{6},\frac{2}{6}]$	$[\frac{2}{6},\frac{3}{6}]$	$[\frac{3}{6},\frac{4}{6}]$	$[\frac{4}{6},\frac{5}{6}]$	$[\frac{5}{6},1]$
$\Delta t^p_{l,A}$	-	0	0	11	30	11	0
$\Delta t^p_{l,B}$	-	30	11	0	0	0	11
$\Delta t^p_{l,AF}$	-	-30	-11	11	30	11	-11

5.2. Initial State of Charge Simulation for eVTOL Arrivals at a Vertiport

This section explains the simulation of the initial SOC of each eVTOL upon their arrival at the vertiport Terminal Area. Because of the usage of a hexagon vertiport lay-out, it is assumed that most eVTOLs arriving at the hub vertiport (vertiport 1) have a similar SOC remaining. However, deviations can occur due to wind, weather and required detours from the geodesic path. A normal distribution is therefore used with a mean μ at the 'plain' remaining SOC that should be remaining without any external influences. A standard deviation σ is assigned to account for these influences. Section 2.3 already describes the lack of a detailed eVTOL battery performance research for different flight profiles. Therefore, it is assumed that in general eVTOLs are able to fly the arrival trajectory relating to the highest delay absorption in shallow descent. The mean μ is thus computed from the arrival trajectory optimisation and the battery prognostics module, Module 1 and 2, in Sections 4.1, 4.2 and 4.3. The standard deviation σ is determined from the most extreme feasible case, such that the eVTOL battery SOC always allows for the most energy-efficient arrival without any delay absorption.

$$SOC_{initial} \sim N(\mu, \sigma^2) \tag{5.12}$$

6

Results

This chapter discusses the results for the eVTOL vertiport arrival ConOps and eVTOL arrival sequencing and scheduling model described in Chapter 3 and 4. The results from Module 1 on eVTOL arrival trajectory optimisation are discussed in Section 6.1. Afterwards, the results for Module 2a and 2b on the flight performance and battery prognostics are depicted in Section 6.2 and 6.3, respectively. Section 6.4 writes about the proof of concept for the eVTOL arrival sequencing and scheduling model using a single landing pad. A more elaborate case study is performed to prove the validity of all eVTOL arrival sequencing and scheduling model variations for single landing pad and double landing pad in Chapter 7.

6.1. Results for Module 1 - eVTOL Arrival Trajectory Optimisation Model

This section discusses the results obtained using the arrival trajectory optimisation model described in Section 4.1 and the concept of operations as proposed in Chapter 3. The results for the ConOps using a single landing pad are described in Subsection 6.1.1. Subsection 6.1.2 discusses the optimal trajectory when using a ConOps with double landing pad.

6.1.1. Results for Module 1 - eVTOL Arrival Trajectory Optimisation Model for Single Landing Pad

The eVTOL arrival trajectory optimisation is solved according to the method in Section 4.1 thus in 4 flight segments split up over two GPOPS-II trajectory optimisation runs. The first run solves the cruise flight between the optimisation at the Terminal Area border to the TOD (N=1) and the shallow descent path from the TOD to the approach fix (AF) (N=2) based on a given RTA input. The second run solves the flight inside the Final Approach Area which consists of a horizontal flight phase (N=3) and a vertical flight phase (N=4). The initial and final conditions and the resulting state and control variables for each flight phase are shown in Table 6.1 for an RTA at the AF of $165s$. The highlighted parameters are results that vary with the required RTA at AF. Tables B.1 to B.4 in Appendix B show the results for each flight phase for another selection of required RTAs at the AF ($300s$, $400s$, $500s$, $525s$).

As the EHANG-184 cruise is designed to take 25 minutes at maximum, the descent phase is set to take 10 minutes at maximum. Therefore, an RTA at the AF of $525s$ is used as the slowest possible arrival trajectory. The RTA input for the flight inside the Final Approach Area is not variable, because this approach is the same for each eVTOL independent of their scheduled RTA. Therefore, the results for flight phase N=3 and N=4 are found by searching for the most energy-efficient RTA input. The results from this manual search are depicted in Table B.5 in Appendix B. The lowest objective relates to the lowest energy consumption such that the time in Final Approach T_t is set to $142s$ for the EHANG-184 characteristics. This is built up from a $69s$ horizontal final approach (N=3) and a $73s$ vertical final approach (N=4) as can also be deducted from Table 6.1. Besides, T_t is assumed to be the same from approach fix A and B to the vertiport, such that $T_t(A) = T_t(B) = 142s$.

Table 6.1: Results of eVTOL Arrival Trajectory Optimisation for RTA at the Approach Fix of 165s

RTA = 165s at AF	t [s]		d [m]		h [m]		V_x [m/s]	V_h [m/s]	θ [rad]	T [N]
	t_0	t_f	d_0	d_f	h_0	h_f				
Cruise till TOD (N=1)	0	**61**	0	**2930**	500	500	0	27.8	0.27	2450
Shallow descent (N=2)	**61**	**165**	**2930**	3500	500	200	**-2.97**	5.88	-0.45	2360
Horizontal FA (N=3)	**165**	**234**	3500	3900	200	200	0	5.88	0.013	2620
Vertical FA (N=4)	**234**	**307**	3900	3900	200	0	-2.87	0	-0.45	2350

The eVTOL trajectory optimisation results are also visually represented in Figure 6.1 to 6.4. The side view and vertical velocity V_x profile for the realised arrival trajectories for the different RTA to AF are presented in Figure 6.1 and 6.2, respectively. It is clearly observed that a higher RTA at the AF input results in a longer and more shallow descent by reducing the vertical speed during the shallow descent phase. Besides, the lowest feasible RTA at AF input and thus fastest possible descent is found to be 165s. This result shows to be constraint by the maximum descent speed of 3.0m/s to prevent the Vortex Ring State.

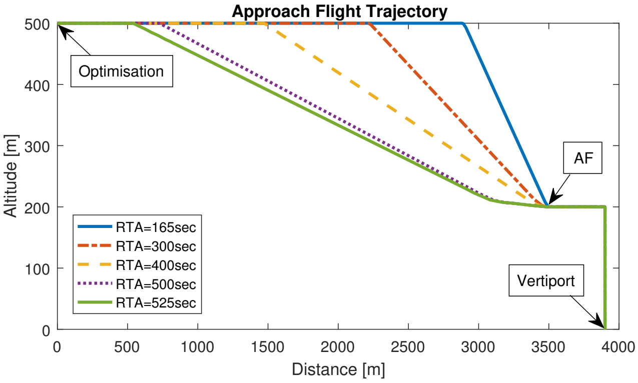

Figure 6.1: Flight Profile of EHANG-184 Energy-Optimal Trajectory Results for ConOps described in Section 3.1

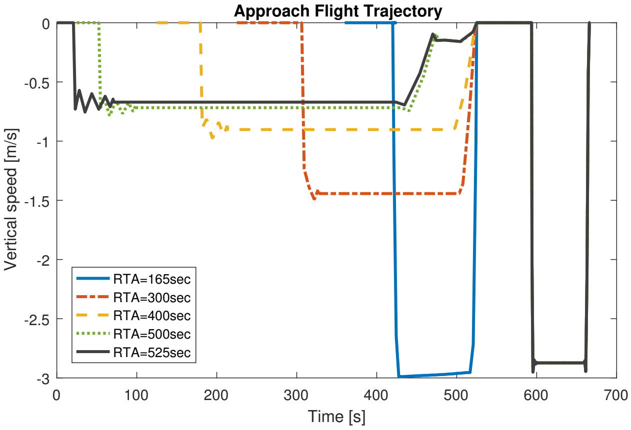

Figure 6.2: Vertical Speed of EHANG-184 Energy-Optimal Trajectory Results for ConOps described in Section 3.1 and for the Different RTA Trajectories in Figure 6.1

Besides, the most energy-optimal thrust control input T for a shallow descent of 165s at the AF is shown in Figure 6.3. Dips or irregularities are observed in the thrust control input during transitions between the four flight phases. These dips are caused by the discontinuity in the GPOPS-II computations and the assumption of the eVTOL being a point-mass [5]. The latter means that e.g. torque is not considered and that it is possible to jump from one control input to another (step changes).

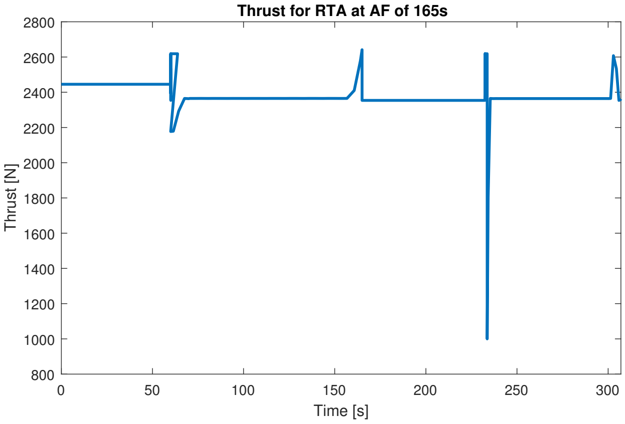

Figure 6.3: Thrust profile of EHANG-184 Energy-Optimal Trajectory Results for ConOps described in Section 3.1 and RTA to Approach Fix of 165 s

The total energy consumption resulting from the GPOPS-II trajectory optimisation for different required RTA at the AF is depicted in Figure 6.4. From this figure, it can be concluded that the fastest, thus most time-efficient, trajectory is also the most energy-efficient trajectory. Therefore, the choice of the target ETA or baseline arrival trajectory for EHANG 184 is set to the earliest possible RTA at the Approach Fix of 165s. Together with a standard Final Approach of 142s, the ETA of each eVTOL without delay is thus 307s from the Terminal Area border. This thus relates to the trajectory as depicted in Table 6.1.

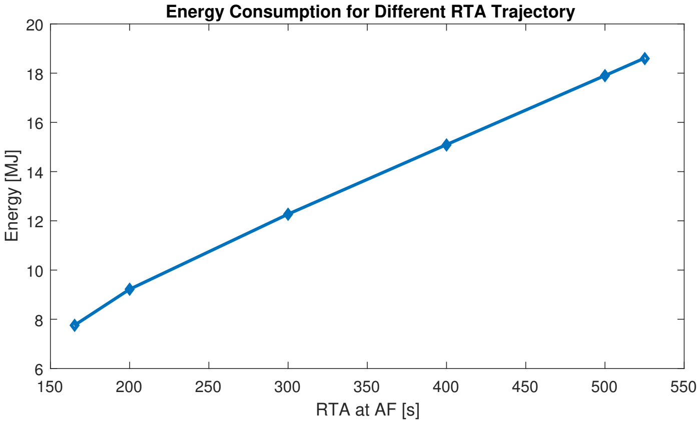

Figure 6.4: Energy Required for EHANG-184 Energy-Optimal Arrival Trajectories for the Different RTA Trajectories in Figure 6.1

6.1.2. Results for Module 1 - eVTOL Arrival Trajectory Optimisation Model for Double Landing Pad

This subsection shortly elaborates on the results for the eVTOL arrival trajectory optimisation module that uses a double landing pad ConOps, which is described in Section 3.2. The eVTOL arrival trajectory for the flight phase until the approach fix (N=1, N=2) and the vertical descent to the selected landing pad (N=4) remain the same as shown in Subsection 6.1.1 using a single landing pad. Only the horizontal flight phase between the approach fix and landing pad is shorter to ensure separation between the two landing pads (see Figure 3.4 in Section 3.2). The horizontal flight inside the Final Approach Area is now 135m, thus 265m shorter compared to a single landing pad approach. The horizontal speed V_h of 5.88m/s from Table 6.1 is used to find a reduction in flight time of 45s. Therefore the new flight time inside the Final Approach Area reduces from 142s for single landing pad to 97s for double landing pad such that $T_t(A) = T_t(B) = 97s$.

6.2. Results for Module 2a - eVTOL Flight Dynamics Model for EHANG-184

After the computation of the most energy-efficient arrival of eVTOLs, the EHANG-184 flight dynamics in Module 2a are advised to find the required power to perform each of the RTA trajectories in Figure 6.1. The results for the required power P_r, induced power P_i, climb power P_c and profile power P_f for an RTA at the AF of 165s is shown in Figure 6.5. This figure shows the same irregularities as observed in Figure 6.3 when switching between each flight phase. This is again caused by the point-mass assumption and discontinuity in the GPOPS-II software that allows for step changes. Furthermore, it is observed that the required power is counterintuitively higher in descent, which is caused by the increased induced velocity that has to be overcome. This also explains that higher RTA, thus a longer descent phase, consumes more energy as seen in Figure 6.4.

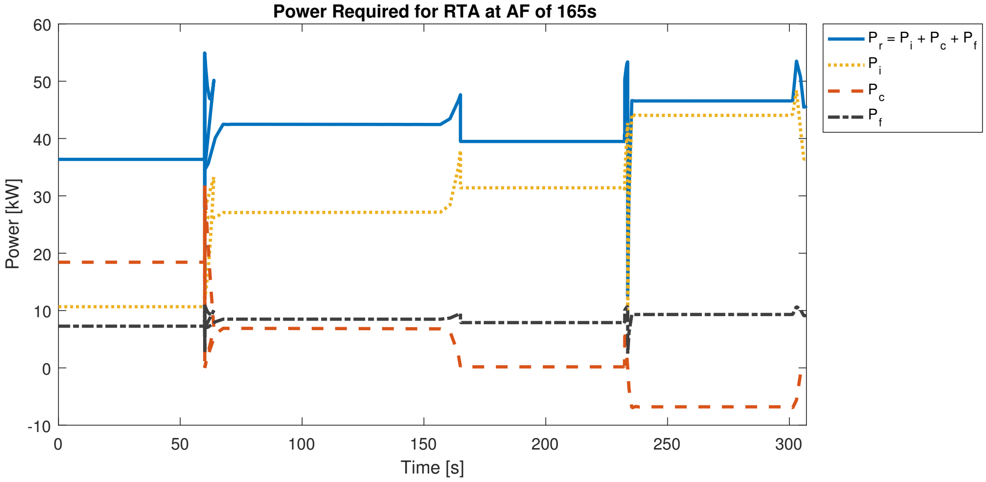

Figure 6.5: Power profile of EHANG-184 Energy-Optimal Trajectory Results for ConOps described in Section 3.1 and RTA to Approach Fix of 165 s

As the instantaneous required power shows to remain stable during each flight phase, Table 6.2 is used to summarise the P_r for different RTA at AF trajectories per flight phase. As observed, only the P_r during shallow descent flight varies with RTA at the AF due to the variation in V_x (see Figure 6.2).

Table 6.2: Results from eVTOL Flight Dynamics Model for EHANG-184 for Different RTA Inputs

Flight Phase [-]	**RTA at AF 165s**	**RTA at AF 300s**	**RTA at AF 400s**	**RTA at AF 500s**	**RTA at AF 525s**
Cruise till TOD (N=1)	36.4	36.4	36.4	36.4	36.4
Shallow descent (N=2)	**42.5**	**40.7**	**40.0**	**40.0**	**40.0**
Horizontal FA (N=3)	39.5	39.5	39.5	39.5	39.5
Vertical FA (N=4)	46.6	46.6	46.6	46.6	46.6

The results from Module 1 and 2a are now also used to find the cost function for the eVTOL arrival sequencing and scheduling tool as shown in Table 6.3. The cost function is, as explained in Subsection 4.4.1, based on the power required to absorb delay by flying shallow descent c_l^p, through a different approach fix $c_{l,af}^p$ or hover $c_{l,h}^p$. Due to the different trajectories flown to absorb delay in shallow descent, c_l^p is computed according to Equation 6.1 using the results from Figure 6.4. The cost for being early c_e^p is not available for EHANG-184, because the ETA is already based on the fastest eVTOL arrival trajectory for an RTA at AF 165s.

$$c_l^p = \frac{\Delta E}{\Delta RTA_{AF}} = \frac{E_{400} - E_{300}}{400 - 300} \tag{6.1}$$

Table 6.3: Cost Function Results from eVTOL Flight Dynamics Model for EHANG-184

Cost Function	c_e^p [-]	c_l^p [-]	$c_{l,af}^p$ [-]	$c_{l,h}^p$ [-]
Value	∅	28	36	42

6.3. Results for Module 2b - eVTOL Battery Prognostics Model

From the power required computed by Module 2a for the eVTOL arrival trajectories computed by Module 1, the required battery State of Charge (SOC) per trajectory is determined by the battery prognostics model in Module 2b. The battery prognostics model is described in Section 4.3 and uses the parameters summarised in Table 6.4.

Table 6.4: Summary of Parameters used in eVTOL Battery Prognostics Model

Battery Parameters	P_f **[% of** P_r]	η_p [-]	η_e [-]	SF [-]	V_{nom} $[V]$	Q $[Ah]$
Value	20	0.7652	0.85	1.5	12	5000

Figure 6.6 shows the resulting SOC demand for the different RTA trajectories from Figure 6.1. The figure is in line with the energy required to perform each trajectory as shown in Figure 6.4. Besides, the SOC demand increases linearly with RTA at the AF, thus with the amount of delay that needs to be absorbed. Therefore, a linear regression is realised between each the RTA and SOC such that the latest possible landing time RTA_l^p can be deducted for each eVTOL based on their battery status or initial SOC. As an example, an initial SOC of 25% is assumed for an eVTOL on top of the deep discharge of 10% that should be avoided. Figure 6.6 shows that this specific eVTOL cannot be scheduled to arrive at the approach fix later than $434s$. Combined with the T_t to a single landing pad of $142s$ or T_t to a double landing pad of $97s$, the RTA_l^p at the vertiport becomes $576s$ or $531s$, which is inserted into the eVTOL arrival sequencing and scheduling model (Module 3) for each arriving eVTOL. This relates to a maximum delay of $269s$ that can be absorbed by this eVTOL.

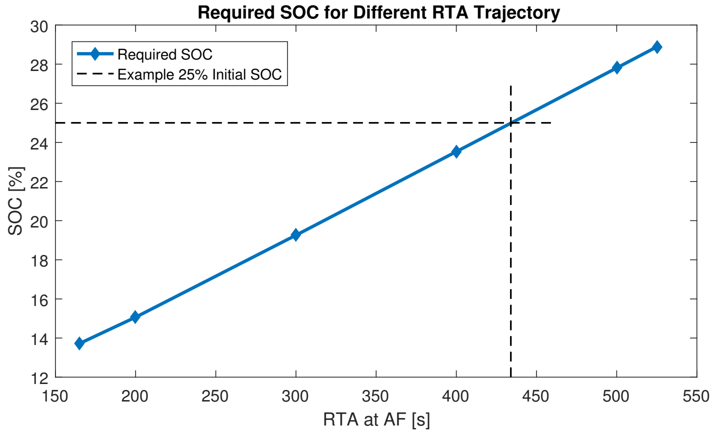

Figure 6.6: SOC Required for EHANG-184 Energy-Optimal Arrival Trajectories for the Different RTA Trajectories in Figure 6.1 with Example 25% SOC and resulting latest RTA at AF of $434s$.

6.4. Proof of Concept for Module 3 - eVTOL Arrival Sequencing & Scheduling Model for Single Landing Pad

All results from Module 1, 2a and 2b come together in Module 3 for the computation of the most optimal eVTOL arrival sequence and schedule regarding minimal delay and constrained by the battery status of the arriving eVTOLs. The input to the proof of concept of Module 3 for the EHANG-184 as discussed in this section is provided in Table 6.5 and the input section of Table 6.6. The latter is manually defined to verify the model, thus to ensure active separation and sequence swapping due to dense arrivals and low initial SOC. The cost function (c_e, c_l) is obtained from [49] for verification purposes, but adapted to the values in Table 6.3 in the case study of Chapter 7. The computation of the time separation requirement Δt_{sep} is discussed in Section 3.1.4, whilst the feasible RTA window for arrival at the approach fix RTA_{AF} and flight time between approach fix and landing pad T_t are described in Section 6.1.

Table 6.5: Summary of Parameters used in the Proof of Concept of eVTOL Arrival Sequencing and Scheduling MILP

MILP Parameters	c_e	c_l	Δt_{sep} [s]	RTA_{AF} [s]	$T_t(A)$ [s]	$T_t(B)$ [s]
Value	20	30	90	[165, 525]	142	142

The results for this proof of concept are presented in Table 6.6 and Figure 6.7. From the RTA schedule output, it can be concluded that the sequence of eVTOL flight 8 and 9 has changed with respect to the FCFS sequence. This is caused by the low battery status of flight 9, constraining it to a direct landing through the most energy-efficient approach. Besides, eVTOL flight 3 and 4 are scheduled to fly via a different approach fix and absorb delay in this way other than choosing for a shallow descent. This results from using the same cost to absorb delay in shallow descent and approach fix divert, showing the significance of the cost function implemented in Table 6.3. The total scheduled delay is depicted by Δt_l of which Δt_{AF} is the delay due to the choice of approach fix and the remainder absorbed in shallow descent $\Delta t_{shallow}$.

Table 6.6: Arrival Sequence and Schedule for Proof of Concept of 10 EHANG-184 eVTOLs

	Input			**Output**				
Flight Nr [-]	**ETA(A)** [s]	**ETA(B)** [s]	**SOC [%]**	**RTA [s]**	**Total** Δt_l [s]	**AF A** [-]	**AF B** [-]	$\Delta t_{l,AF}$ [s]
1	165	180	13	307	0	1	0	0
2	250	250	18	397	5	0	1	0
3	335	325	25	487	20	1	0	**10**
4	420	410	30	577	25	1	0	**10**
5	505	505	18	667	20	1	0	0
6	590	590	13	757	25	1	0	0
7	665	675	25	847	40	1	0	0
8	750	760	25	**1077**	185	1	0	0
9	855	845	**14**	**987**	0	0	1	0
10	930	930	28	1167	95	0	1	0

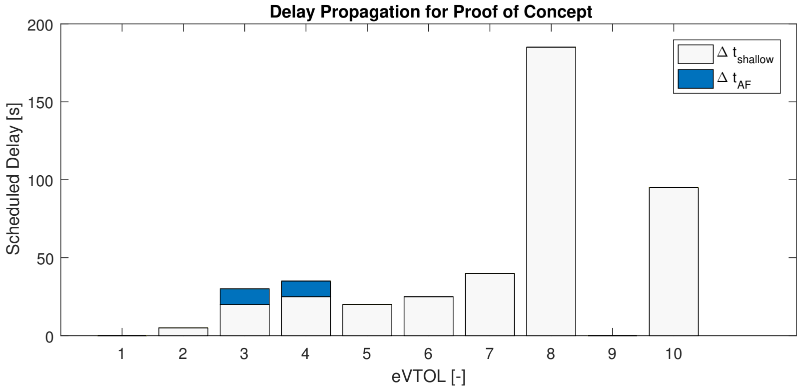

Figure 6.7: eVTOL Delay Propagation at a Vertiport for Proof of Concept

The computational time for this set is found to be around 3s on a laptop with Intel Core i7 processor when using the standard model from Section 4.4.3. If the branch-and-bound algorithm is applied, the computational time increases to over a minute. This is a consequence of the high amount of iterations that the branch-and-bound solver needs to run to end up with an integer solution.

7

Case Study on eVTOL Arrivals in Houston

This chapter discusses the results for the case study on eVTOL arrivals in Houston inspired by [54] to show the validity of the eVTOL arrival ConOps and sequencing and scheduling tool from Chapter 3 and 4. The input to the arrival sequencing and scheduling using EHANG-184 is provided by Table 7.1 and by the demand model for the arrivals at the hub vertiport as described in Chapter 5. The single landing pad model and model variations from Section 4.4 are used to find the results in Section 7.1. The double landing pad model from Section 4.5 resulted in the outcome described in Section 7.2.

Table 7.1: Summary of Parameters used in eVTOL Arrival Sequencing and Scheduling

MILP Parameters	c_e	c_l	$c_{l,af}$	$c_{l,h}$	Δt_{sep} $[s]$	RTA_{AF} $[s]$	$T_t(A,B)$ $[s]$	K [-]	RH [min]
Single Pad	$\emptyset$	28	36	42	90	[165,525]	142	2	2x15min
Double Pad	$\emptyset$	28	36	42	90	[165,525]	97	2	2x15min

7.1. Results for eVTOL Arrivals at a Single Landing Pad in Houston

The results for eVTOL arrival sequencing and scheduling for a single landing pad are depicted in Table 7.2 and based on the input from Table 7.1 and Chapter 5. The model variations from Subsection 4.4.3 are applied to test the improvement of the computational efficiency and scheduled delay results as depicted under 'features'. However, the branch-and-bound algorithm did not improve the computational efficiency of the solver, as discussed in Section 6.4. Therefore, the branch-and-bound solver has not been applied to this case study.

Table 7.2: Overview of Results of eVTOL Arrival Sequencing and Scheduling Model using a Single Landing Pad

Set	**Time of Day**	**Features**	**eVTOL arrivals**	**Comp. time [s]**	**Total delay [s]**	**Max delay [s]**	**Average delay [s]**	**Using divert?**	**Using hover?**
1	11:30-12:30	-	41	720	2279	191	56	No	No
1	11:30-12:30	Simpl. Model	41	10.5	2279	257	56	No	No
1	11:30-12:30	Simpl. Model, Hover, RH	41	0.66	2279	264	56	No	No
2	11:30-12:30	Simpl. Model, Hover	40	26	4105	419	103	No	Yes
2	11:30-12:30	Simpl. Model, Hover, RH	40	2.0	4105	419	103	No	Yes
3	11:30-12:30	Simpl. Model, Hover, RH, Monte Carlo	Fig. C.10	8966	Fig. C.7	Fig. C.4	Fig. C.1	No	Yes/No

It appeared that a single landing pad ConOps, even including hover options, does not provide enough delay absorption and landing facilities to land all eVTOL arrival demand at peak hours (around 8AM and 16PM). Therefore, only off-peak results for the arrival of around 40 eVTOLs around noon are provided in Subsection 7.1.1 till 7.1.4.

7.1.1. Results for Single Landing Pad during Off-Peak without Hover

The first results for set 1 between 11.30 and 12.30 from Table 7.2 compare the use of the simplified model from Subsection 4.4.3 with the standard eVTOL arrival sequencing and scheduling model from Section 4.4. As expected, the computational time of the simplified model is shorter due to the reduced number of decision variables. The results for the total delay and thus for the average delay per eVTOL between 11.30 and 12.30 are similar because both the model with and without z_{pq} use one eVTOL type and the assumption that $T_t(A) = T_t(B)$. However, the maximum scheduled delay is different because the model optimises total delay and can thus find multiple landing sequences that lead to the same total delay. Figure 7.1 shows that the maximum delay is scheduled for eVTOL 38 and 39 using both models depending on the landing sequence, whilst the total delay absorbed by those eVTOLs and thus the objective remains the same.

Neither the standard model nor the simplified model makes use of the ability to divert through a different approach fix. This follows from the higher cost relating to a higher energy consumption compared to flying a shallow descent. Besides, the bottleneck in the arrival sequencing and scheduling is the separation during the last flight phase before arrival at the vertiport. Varying the approach fix selection, therefore, does not reduce the time an eVTOL has to wait before landing, but only provides another method to absorb delay. The detailed eVTOL arrival sequencing and scheduling results obtained from these two model variations for set 1 between 11.30 and 12.30 can be observed in Table C.1 and C.2 in Appendix C.1.

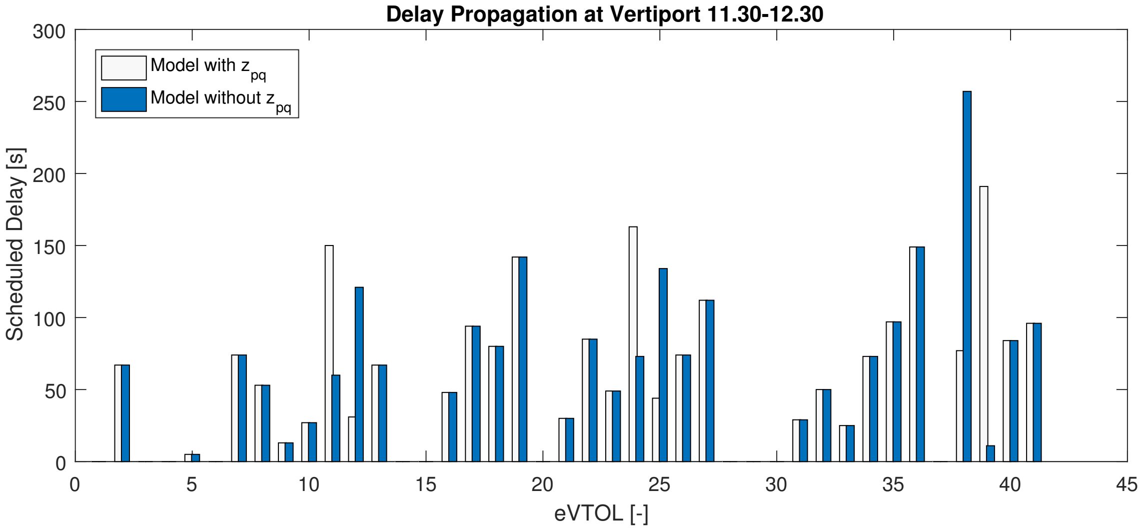

Figure 7.1: Delay Propagation at the Vertiport for Single Landing Pad from Set 1 at 11.30-12.30 (Off-Peak)

7.1.2. Results for Single Landing Pad during Off-Peak using Hover

Where a feasible landing sequence and schedule can be found for set 1 from Table 7.2 without hover, set 2 is infeasible due to a randomly realised combination of a high arrival density and low battery power for a group of eVTOL arrivals. Therefore, the column generation for hover from Section 4.4.3 is enabled to solve set 2. The column generation requires the model to be solved repeatedly for each iteration, which explains the increased computational time in Table 7.7. Figure 7.2 shows that the high arrival density and thus high delay to ensure separation occurs approximately between eVTOL 25 and eVTOL 30. No more than 360s of scheduled delay can be absorbed in shallow descent even if sufficient battery SOC is remaining, such that eVTOL 26 waits 59 extra seconds in hover. The detailed eVTOL arrival sequencing and scheduling results obtained from the hover model variation for set 2 between 11.30 and 12.30 can be observed in Table C.6 in Appendix C.1.

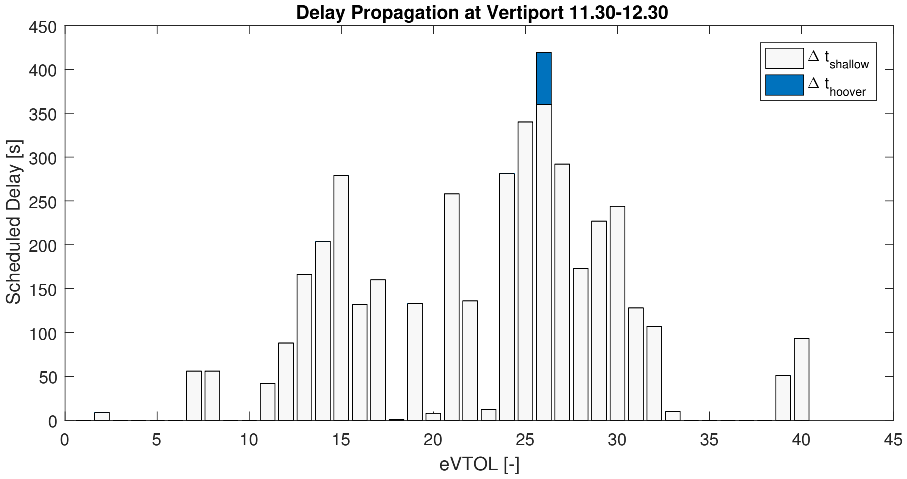

Figure 7.2: Delay Propagation at the Vertiport for Single Landing Pad using Hover from Set 2 at 11.30-12.30 (Off-Peak)

7.1.3. Results for Single Landing Pad during Off-Peak using Hover and Rolling Horizon

When dataset 1 from Table 7.2 is solved using the model formulation with hover and rolling horizon from Section 4.4.3, a similar situation as described in Section 7.1.1 is observed. The total delay remains the same while the maximum delay is slightly different. Also, the diversion through a different approach fix and the hover option both remain unused, because shallow descent flight is more efficient and a feasible solution is already found without hover. The rolling horizon algorithm does increase the computational efficiency further, whilst it does not influence the final total delay solution. This means that the rolling horizon algorithm with a 15 minute planning period can be implemented without losing the ability to find the most optimal solution.

The same is proven by solving dataset 2 from Table 7.2 with the same hover and rolling horizon model. The computational time is improved by over 90% compared to the sequencing and scheduling using hover without the rolling horizon algorithm, while the same total and maximum delay results are found. The detailed eVTOL arrival sequencing and scheduling results obtained from the hover and rolling horizon model variation for set 1 and set 2 between 11.30 and 12.30 can be observed in Appendix C.1 in Table C.3 and C.7, respectively.

7.1.4. Results of Monte Carlo Simulation for Single Landing Pad during Off-Peak using Hover and Rolling Horizon

Subsections 7.1.1 till 7.1.3 described the results for two random off-peak eVTOL arrival demand generations. This section performs a Monte Carlo Simulation with 2000 generations of the ETAs and SOCs for eVTOLs arriving between 11.30 and 12.30 using again the eVTOL arrival demand model for Chapter 5. Each generation is solved using the eVTOL arrival sequencing and scheduling model including hover and rolling horizon from Section 4.4. It was found that only 1227 runs were solved due to random high peak or low battery generations leading to infeasibility of those datasets. The results from the feasible simulations are shown in Table 7.3 till 7.6 and Figure 7.3. The histograms that elaborate on the results for the expected average, maximum and total delay and the expected number of eVTOL arrivals can be found in Appendix C.2 as depicted in Table 7.2.

Table 7.3 shows the expected (μ) average, maximum and total delay for eVTOLs arriving at a vertiport between 11.30 and 12.30 and the standard deviation from this expectation (σ). A high σ relative to the μ, therefore, means that there is a high probability of deviation from the expectation. It shows that the hourly arrivals are likely to be around 33 eVTOLs, while the resulting delays vary more depending on the generated ETAs. From this, it can be concluded that the delay is lower when the eVTOLs arrive equally spread over the hour. Besides, Table 7.4 even shows that there is an 81% chance that at least one eVTOL has to absorb delay equal to double the time separation ($180s$). This means that in most generations, the single landing pad capacity is, even with hover, not sufficient to keep delays to a maximum of the required time separation. Therefore, the results for a double landing pad need to be examined.

Table 7.3 and 7.5 are analysed to check when the eVTOL arrival sequencing and scheduling model benefits from the hover option to increase landing capacity where needed. It shows that one out of five runs is expected to use hover (19%). Besides, at maximum two eVTOLs per hour use hover with a probability of over 99%. This means that hover options are utilised, but only if strictly necessary.

Table 7.3: Results for Monte Carlo Simulation for Single Landing Pad using Hover and Rolling Horizon at 11.30-12.30 (Off-Peak)

	Mean μ	**St. Dev.** σ
Average Delay [*s*]	66	36
Max Delay [*s*]	274	98
Total Delay [*s*]	2260	1388
Hourly Arrivals [-]	33	5
Hourly Hovers [-]	0.19	0.59

Table 7.4: Hourly Delay Expectations for Single Landing Pad using Hover and Rolling Horizon at 11.30-12.30 (Off-Peak)

	Probability [-]
Average delay > 90 *s*	0.24
Max delay > 90 *s*	0.97
Max delay > 180 *s*	0.81
Max delay > 360 *s*	0.13

Table 7.5: Hover Results for Monte Carlo Simulation for Single Landing Pad using Hover and Rolling Horizon at 11.30-12.30 (Off-Peak)

Hourly Hover [-]	0	1	2	>2
Occurrence [-]	1070	109	43	5
Probability [-]	0.84	0.09	0.03	0.00

The results discussed above only cover hourly expectations. Therefore, an analysis is performed on the scheduled delay for each eVTOL in the 1277 feasible Monte Carlo Simulation runs. Figure 7.3 and Table 7.6 show the results for all 15627 eVTOLs arriving between 11.30 and 12.30 at a single landing pad vertiport. It occurs most frequently that eVTOLs have to absorb zero or very low (<20*s*) delay, while only 56% of the eVTOLs arrive with a delay less than 1 minute. Although with decreasing probability, delay is absorbed up to 6 minutes (360*s*). There is a 15% probability that the scheduled delay per eVTOL is over 3 minutes, so more than double the time separation. This indicates again that for some datasets, the single landing pad capacity is not sufficient to provide time- and energy-efficient arrivals.

The chance that an eVTOL has to divert to another approach fix or hover is only 0% and 1%, respectively, which indicates again that delay absorption in shallow descent is preferred over an approach fix divert or hover. The only eVTOLs that absorb more than 6 minutes or 360*s* of scheduled delay in Table 7.6 are the eVTOLs in hover. If the hover option is utilised, it stays at the Terminal Area boundary for at maximum 3 minutes. This adds up to a maximum 9 minute delay.

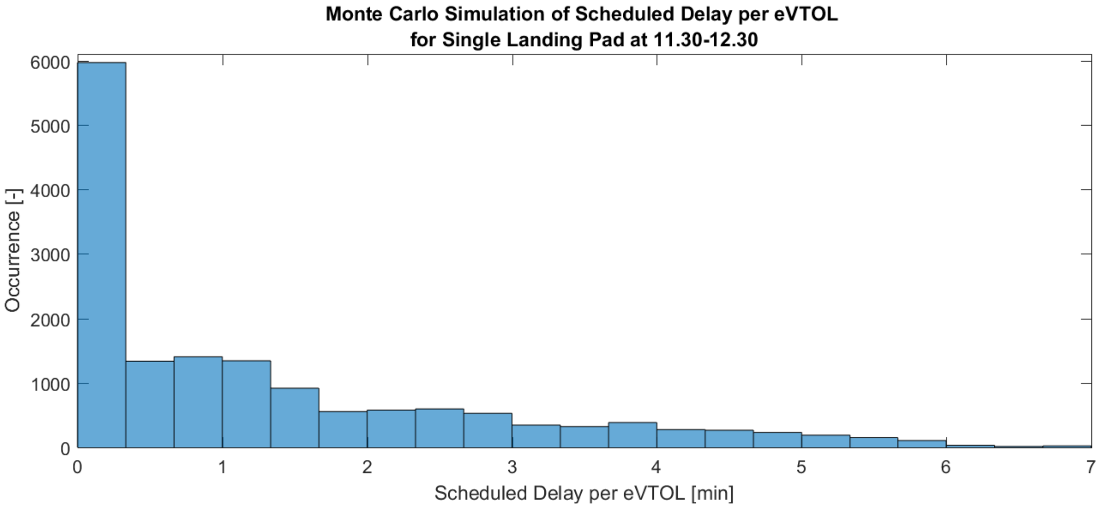

Figure 7.3: Monte Carlo Simulation of Scheduled Delay per eVTOL for Single Landing Pad using Hover and Rolling Horizon at 11.30-12.30 (Off-Peak)

Table 7.6: Delay Expectations per eVTOL arriving at a Single Landing Pad using Hover and Rolling Horizon at 11.30-12.30 (Off-Peak)

Scheduled Delay per eVTOL	**Probability [-]**
$\Delta t_l < 1$ min	0.56
$\Delta t_l < 2$ min	0.74
$\Delta t_l < 3$ min	0.85
$\Delta t_l < 4$ min	0.91
$\Delta t_l < 5$ min	0.96
$\Delta t_l < 6$ min	0.99
$\Delta t_l < 9$ min	1.00
$\Delta t_{l,h} > 0\ s$	0.01
$\Delta t_{l,af} > 0\ s$	0.00

7.2. Results for eVTOL Arrivals at a Double Landing Pad in Houston

The results for eVTOL arrival sequencing and scheduling for a double landing pad are depicted in Table 7.7 and based on the input from Table 7.1 and Chapter 5. The vertiport landing capacity of a double landing pad ConOps is higher compared to a single landing pad ConOps which allows for solving the eVTOL arrival demand for off-peak arrivals between 11.30 and 12.30, peak arrivals between e.g. 7.30 and 8.30 and an entire 24 hour day. Each of the resulting datasets is solved using the eVTOL arrival sequencing and scheduling model for double landing pad using hover as described in Section 4.5, mostly using the rolling horizon algorithm to keep the computational time as low as possible.

The results for the same off-peak datasets as discussed in Section 7.1 for a single landing pad are described in Subsections 7.2.1 and 7.2.2. A peak dataset is generated and analysed in Subsection 7.2.3. The Monte Carlo Simulations for both off-peak and peak eVTOL arrival demand are discussed in Subsection 7.2.4, after which the eVTOL arrival sequence and schedule for an entire day is described in Subsection 7.2.5.

Table 7.7: Overview of Results of eVTOL Arrival Sequencing and Scheduling Model using a Double Landing Pad

Set	Time of Day	Features	eVTOL Arrivals	Comp. Time [s]	Total Delay [s]	Max Delay [s]	Average Delay [s]	Using Divert?	Using Hover?
1	11:30-12.30	Hover	41	374	162	30	4	Yes	No
1	11:30-12.30	Hover, RH	41	10	162	30	4	Yes	No
2	11:30-12.30	Hover	40	1872	674	139	17	Yes	No
2	11:30-12.30	Hover, RH	40	218	674	104	17	Yes	No
3	11:30-12.30	Hover, RH, Monte Carlo	Fig. C.12	15523	Fig. C.9	Fig. C.6	Fig. C.3	Yes	No
4	7:30-8.30	Hover, RH	69	569	625	76	9	Yes	No
5	7:30-8.30	Hover, RH, Monte Carlo	Fig. C.11	83572	Fig.C.8	Fig.C.5	Fig. C.2	Yes	No
6	0:00-24.00	Hover, RH	715	18477	15932	309	22	Yes	No

7.2.1. Results for Double Landing Pad during Off-Peak using Hover

This subsection presents the results for set 1 in Table 7.7 for eVTOL arrivals between 11.30 and 12.30 at a double landing pad using the model in Section 4.5. The same set has been solved for a single landing pad in Section 7.1. Both schedules have been visualised in Figure 7.4. Again the hover option is not utilised for this dataset 1, because the landing pad capacity is sufficient without hover.

Figure 7.4 clearly shows that the increase in landing pad capacity greatly reduces the scheduled eVTOL arrival delay. Besides, the double landing pad model regularly benefits from the approach fix divert, where the single landing pad model never showed to divert eVTOLs as it is a less energy-efficient delay absorption method. From this, it is concluded that a shorter waiting time outweighs the detour through a further approach fix and landing at a further landing pad. The total delay of $162s$ and maximum delay of $30s$ are thus also much lower for a double landing pad ConOps compared to the total delay of $2279s$ and maximum delay of $264s$ for a single landing pad. Furthermore, the computational time is shorter, because the sequencing and scheduling is less challenging.

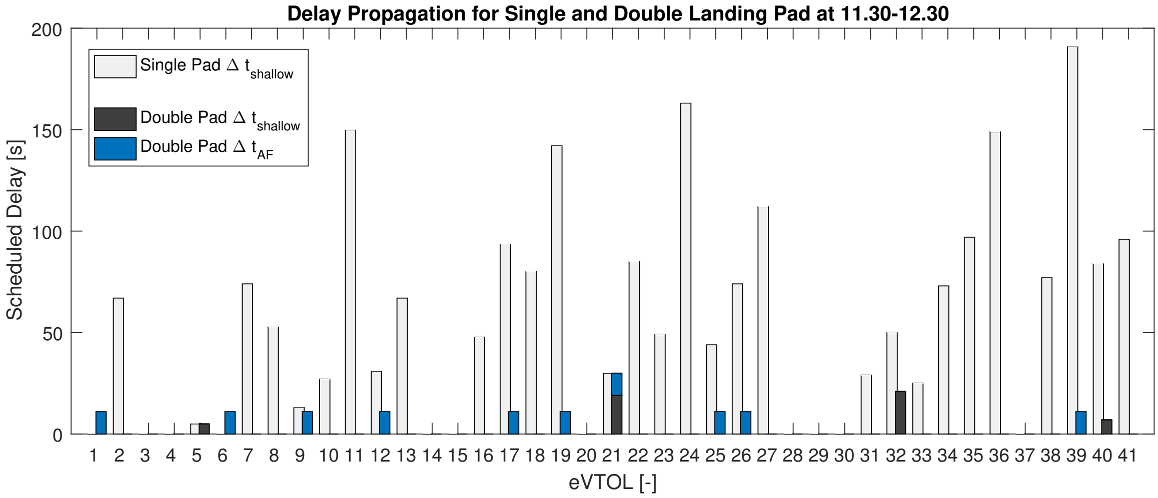

Figure 7.4: Delay Propagation at the Vertiport for Double Landing Pad using Hover at 11.30-12.30 (Off-Peak)

Set 2 from Table 7.7 is also solved for both a single and a double landing pad configuration. Again a large reduction in total, maximum and average delay can be observed in the double landing pad solution. Where the single landing pad solution includes a hovering eVTOL, the double landing pad model provides sufficient landing capacity without hovering. The detailed eVTOL arrival sequencing and scheduling results obtained from the double landing pad model with hover for set 1 and set 2 between 11.30 and 12.30 can be observed in Appendix C.1 in Table C.4 and C.8, respectively.

7.2.2. Results for Double Landing Pad during Off-Peak using Hover and Rolling Horizon

The eVTOL arrival sequencing and scheduling results obtained with the double landing pad model from Section 4.5 including hover and rolling horizon show similar delay results as for that model without rolling horizon described in Subsection 7.2.1. However, the maximum delay varies for the same minimum total delay solution as also explained in Subsection 7.1.3 for a single landing pad including hover and rolling horizon. The computational time for set 1 and 2 are however reduced for the same optimal solution, such that the remainder of this section only shows results obtained with the rolling horizon algorithm. The detailed eVTOL arrival sequencing and scheduling results obtained from the double landing pad model with hover and rolling horizon for set 1 and set 2 between 11.30 and 12.30 can be observed in Appendix C.1 in Table C.5 and C.9, respectively.

7.2.3. Results for Double Landing Pad during Peak using Hover and Rolling Horizon

As observed from Figure 7.4 in Subsection 7.2.1, the delay decreases and capacity of the eVTOL arrival sequencer and scheduler increases for a double compared to a single landing pad configuration. Therefore, a simulation is performed on a high demand case during the rush hour between 7.30 and 8.30 as described in Chapter 5 and solved using the model from Section 4.5 with rolling horizon. Even though the eVTOL arrival rate is computed to be 69 (see again Table 7.7), only the first 45 eVTOLs are expected to arrive between 7.30 and 8.30 for which the scheduled delay per eVTOL is shown in Figure 7.5. The maximum delay is found to be only $76s$ again resulting from efficient usage of the approach fix and thus landing pad selection. Mostly, eVTOLs that can easily choose between two approach fixes are diverted ($\Delta t_{AF} = 11s$), except for eVTOL 23 that has to fly a 180° detour ($\Delta t_{AF} = 30s$) which should be avoided as much as possible to reduce interference with departing traffic. The detailed eVTOL arrival sequencing and scheduling results discussed in this subsection can be observed in Appendix C.1 in Table C.10.

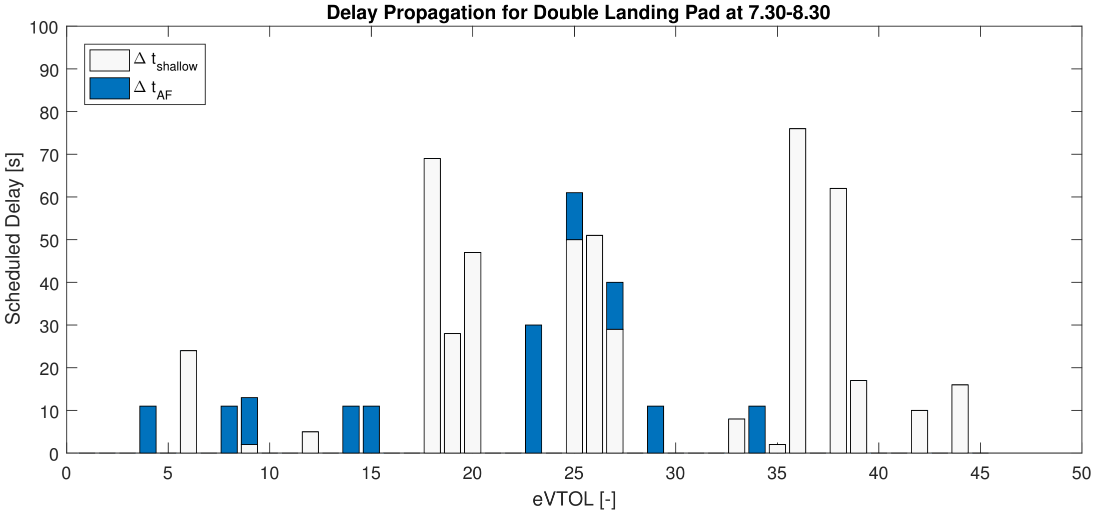

Figure 7.5: Delay Propagation at the Vertiport for Double Landing Pad
using Hover and Rolling Horizon at 7.30-8.30 (Peak)

7.2.4. Results of Monte Carlo Simulation for Double Landing Pad during Peak and Off-Peak using Hover and Rolling Horizon

Subsections 7.2.1 till 7.2.3 describe the results for random off-peak and peak eVTOL arrival demand generations. This section, therefore, performs a Monte Carlo Simulation with 100 arrival demand generations between 11.30 and 12.30 and 100 runs of which 90 feasible between 7.30 and 8.30. Each generation is then solved by the eVTOL arrival sequencing and scheduling for double landing pad using hover and rolling horizon from Section 4.4. The results from all feasible runs are presented for the double landing pad and repeated for the single landing pad Monte Carlo Simulations in Table 7.8, 7.9 and 7.10 and Figures 7.6 and 7.7. The histograms that elaborate on the results for the expected average, maximum and total delay and the expected number of eVTOL arrivals can be found in Appendix C.2 as depicted in Table 7.7.

Table 7.8 and 7.9 clearly show again that the arrival capacity for a double landing pad ConOps is larger than for the single landing pad ConOps resulting in lower average, maximum and total delay. Also, the expected total delay for peak arrivals at a double landing pad is comparable to the expected total delay for off-peak arrivals at a single landing pad while a double number of eVTOL arrivals occur during peak. From this it can be concluded that doubling the number of landing pads results in 1) the ability to host a double amount of eVTOL arrivals for a similar total delay and 2) an 85% reduction of the expected total delay for the same amount of eVTOL arrivals. The latter is also observed in Table 7.9 where the maximum delay is highly unlikely (2%) compared to highly likely (97%) to reach above the time separation requirement of 90s during off-peak arrivals. Besides, even during peak hours, the delay scheduled for arrival at a double landing pad vertiport never reaches above 180s where this is likely (81%) to occur off-peak at a single landing pad.

Table 7.8: Results for Monte Carlo Simulation for eVTOLs arriving at a Single or Double Landing Pad using Hover and Rolling Horizon at 7.30-8.30 (Peak) and 11.30-12.30 (Off-Peak)

	Double Pad, Peak		**Double Pad, Off-Peak**		**Single Pad, Off-Peak**	
	Mean μ	**St. Dev. σ**	**Mean μ**	**St. Dev. σ**	**Mean μ**	**St. Dev. σ**
Average Delay [s]	37	22	9	7	66	36
Max Delay [s]	189	67	74	45	274	98
Total Delay [s]	2776	1858	356	299	2260	1388
Hourly Arrivals [-]	73	8	36	6	33	5
Hourly Hovers [-]	0	0	0	0	0.19	0.59

Table 7.9: Hourly Delay Expectations for eVTOLs arriving at a Single or Double Landing Pad using Hover and Rolling Horizon at 7.30-8.30 (Peak) and 11.30-12.30 (Off-Peak)

	Double Pad, Peak **Probability** [-]	**Double Pad, Off-Peak** **Probability** [-]	**Single Pad, Off-Peak** **Probability** [-]
Average delay > 90 s	0.03	0	0.24
Max delay > 90 s	0.46	0.02	0.97
Max delay > 180 s	0	0	0.81
Max delay > 360 s	0	0	0.13

The tables above only present the results on the hourly expectations. Therefore, the scheduled delay for all 2364 eVTOLs arriving during peak demand and all 1426 eVTOLs arriving during off-peak is analysed using Figure 7.6 and 7.7, respectively. From those figures, the expected scheduled delay per eVTOL is computed in Table 7.10 based on their arrival time. As also observed in Table 7.3, eVTOLs do not use the option to hover when a double landing pad ConOps is applied.

Besides, it can again be recognised that the scheduled delay is larger during peak than during off-peak hours and for a single landing pad than for a double landing pad ConOps. Where delay larger than 6 minutes can occur for eVTOLs arriving at a single landing pad around noon, the scheduled eVTOL delay is likely to stay within 1 minute (94%) or 3 minutes (96%) when arriving at a double landing pad around noon or 8AM, respectively.

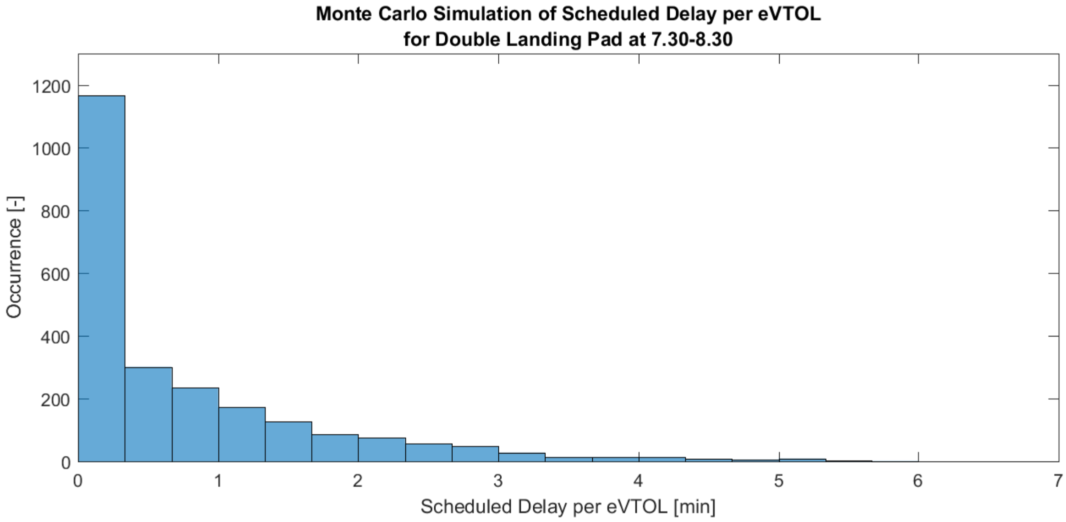

Figure 7.6: Monte Carlo Simulation of Scheduled Delay per eVTOL for Double Landing Pad using Hover and Rolling Horizon at 7.30-8.30 (Peak)

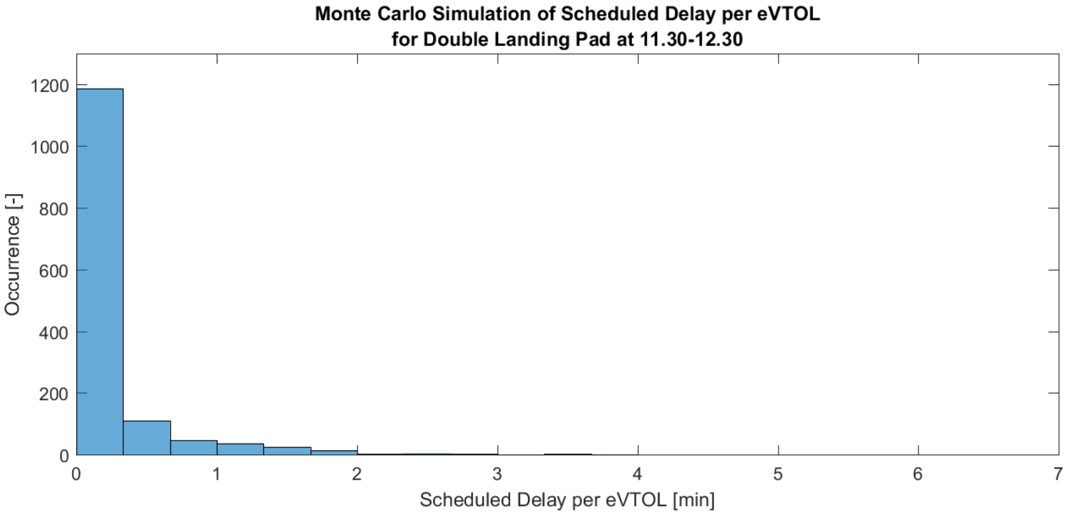

Figure 7.7: Monte Carlo Simulation of Scheduled Delay per eVTOL for Double Landing Pad using Hover and Rolling Horizon at 11.30-12.30 (Off-Peak)

Table 7.10: Delay Expectations per eVTOL arriving at a Single or Double Landing Pad using Hover and Rolling Horizon at 7.30-8.30 (Peak) and 11.30-12.30 (Off-Peak)

Scheduled Delay per eVTOL	**Double Pad, Peak Probability** [-]	**Double Pad, Off-Peak Probability** [-]	**Single Pad, Off-Peak Probability** [-]
$\Delta t_l < 30\ s$	0.55	0.86	0.42
$\Delta t_l < 1$ min	0.72	0.94	0.56
$\Delta t_l < 2$ min	0.88	1.00	0.74
$\Delta t_l < 3$ min	0.96	1.00	0.85
$\Delta t_l < 4$ min	0.98	1.00	0.91
$\Delta t_l < 5$ min	1.00	1.00	0.96
$\Delta t_l < 6$ min	1.00	1.00	0.99
$\Delta t_{l,h} > 0\ s$	0	0	0.01

7.2.5. Results of Day Simulation for Double Landing Pad using Hover and Rolling Horizon

This chapter has so far focused on the results obtained for eVTOL arrivals either between 7.30 and 8.30 or 11.30 and 12.30. Therefore, the entire daily eVTOL arrival demand model from Figure 5.2 in Chapter 5 is used to generate eVTOL arrivals and the corresponding arrival sequence and schedule for an entire day in this section. The outcome is shown in Figure 7.8 till 7.11 and again obtained from the eVTOL arrival sequencing and scheduling model for a double landing pad including rolling horizon from Section 4.5.

Figure 7.8 shows two main peaks in the arrivals of eVTOLs per hour as expected from the high demand during the commuter rush hours (see again Figure 5.2). Due to the on-demand service in UAM, the number of eVTOL arrivals differs every day even when an indication of the demand is available, as proven by the generation for one day in Figure 7.8. A higher amount of arrivals is realised between 13.00 and 14.00 where fewer arrivals occur between 14.00 and 15.00 compared to the expectation. The delay results obtained for this hourly eVTOL arrival distribution are presented in Figure 7.9, 7.10 and 7.11 and in detail in Table C.11 in Appendix C.1.

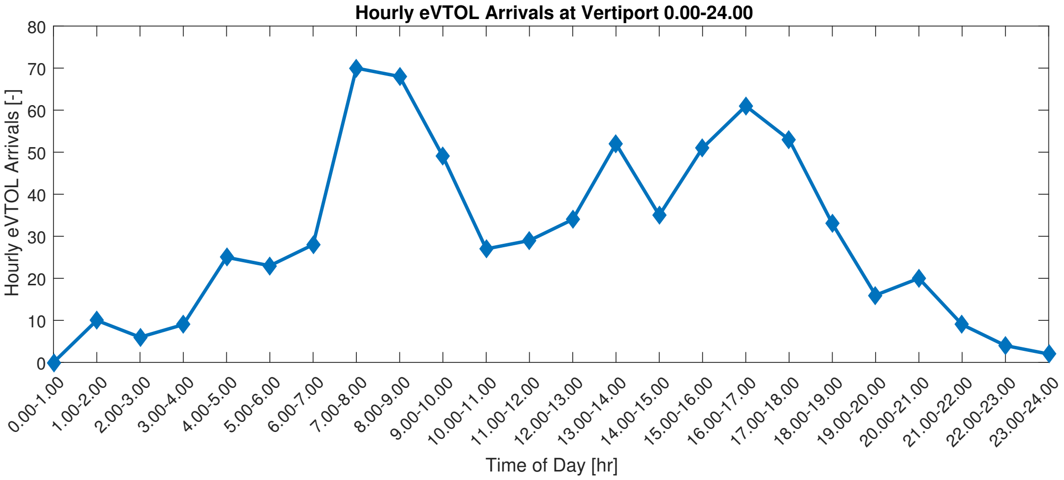

Figure 7.8: Hourly eVTOL Arrivals at a Vertiport for Double Landing Pad using Hover and Rolling Horizon over One Day

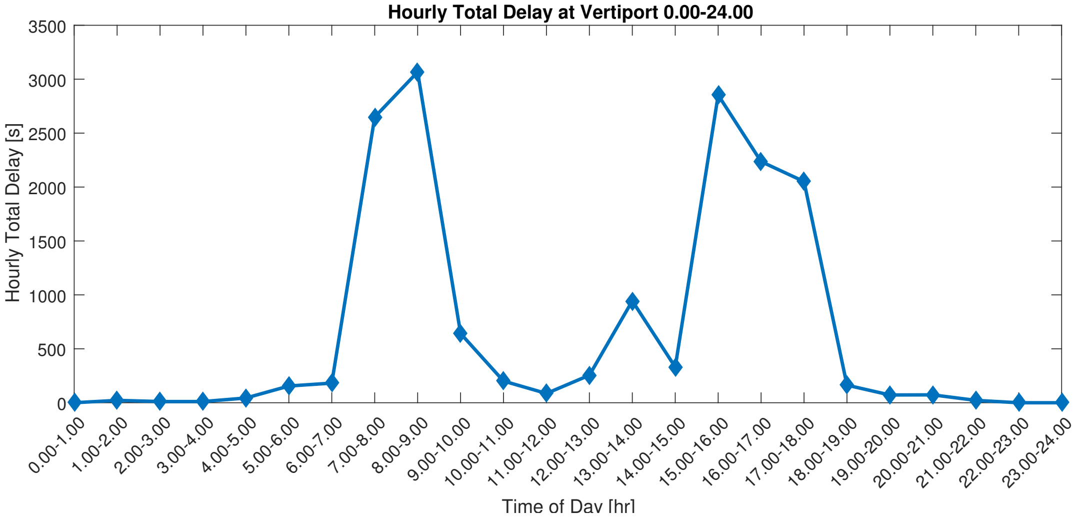

Figure 7.9: Hourly Total Delay at a Vertiport for Double Landing Pad using Hover and Rolling Horizon and Hourly eVTOL Arrivals from Figure 7.8

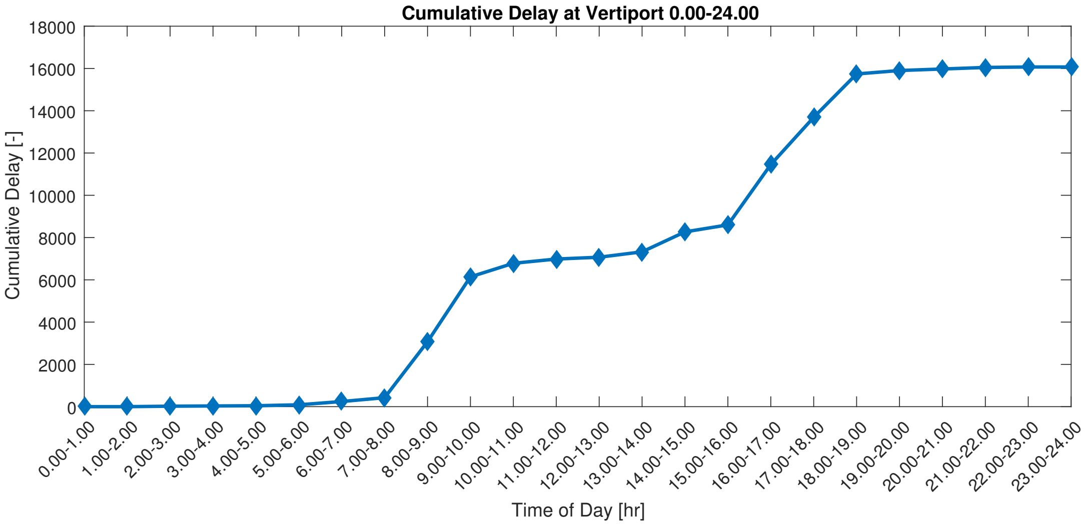

Figure 7.10: Cumulative Delay at a Vertiport for Double Landing Pad using Hover and Rolling Horizon and Hourly eVTOL Arrivals from Figure 7.8

Figure 7.9 and 7.10 depict the total delay for each hour of eVTOL arrivals and the cumulative delay over the entire day based on the generation from Figure 7.8. It is clearly observed that a higher amount of eVTOLs leads to a higher delay and that most daily delay is created during the rush hour peaks around 8.00 and 16.00 o'clock. Besides, the hourly total delay remains below 1000s for the arrival of approx. 50 eVTOLs, where this same delay rises to around 3000s for the arrival of approx. 70 eVTOLs. An increase of only 20 arrivals per hour thus already leads to a tripling of the hourly total delay results. This suggests that the maximum hourly arrival capacity is reached around 60 eVTOLs/hr if delays should not be common. Also, it indicates that spreading the high peak eVTOL arrival demand over time can significantly reduce the cumulative delay outcome.

This behaviour is observed less obviously in Figure 7.11. The hourly maximum delay does in general increase with an increase in eVTOL arrivals, but the peak in the hourly maximum delay between 15.00 and 16.00 (309s) and between 8.00 and 9.00 (175s) differs significantly while they both host around 70 eVTOL arrivals. This again proofs that the maximum delay depends on the spread of the ETAs in the dataset as only the total delay is optimised.

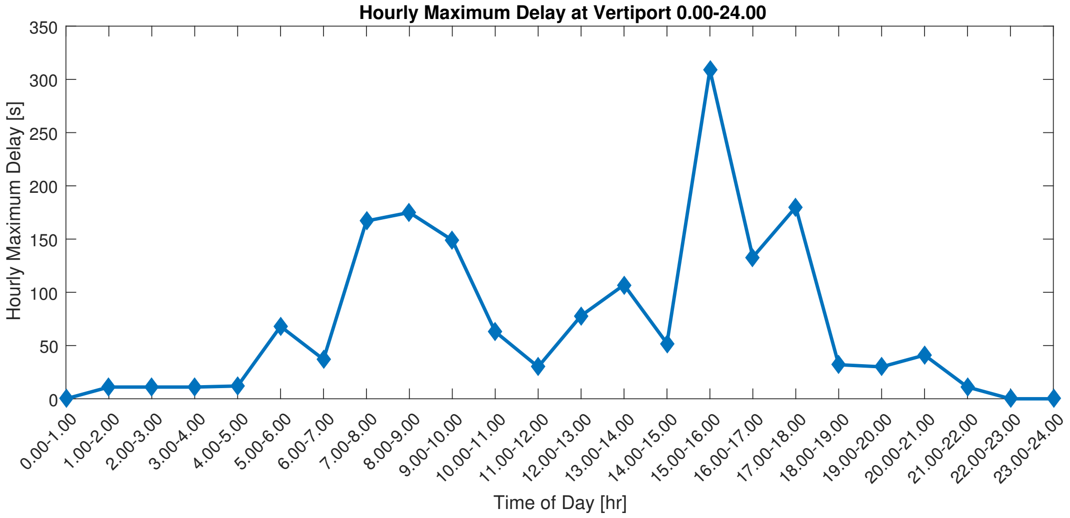

Figure 7.11: Hourly Maximum Delay at a Vertiport for Double Landing Pad using Hover and Rolling Horizon and Hourly eVTOL Arrivals from Figure 7.8

8

Sensitivity Analysis

This chapter discusses a sensitivity analysis to assess the eVTOL arrival sequencing and scheduling model specifications and thus the flexibility of the model and the strength of the conclusions drawn in Chapter 7. Three model parameters are discussed, namely the number of position shifts in the Constrained Position Shifting, the time separation between eVTOL arrivals, the rolling horizon period length and the battery state of charge input in Section 8.1, 8.2, 8.3 and 8.4, respectively. All results have been generated using the eVTOL arrival sequencing and scheduling model for a double landing pad ConOps (Section 3.2) using the model in Section 4.5 and a realisation of the demand model in Chapter 5 for an entire day. The outcome of each sensitivity analysis is compared to the baseline results discussed in Section 7.2.5, which relates to the hourly eVTOL arrivals at a vertiport as again presented in Figure 8.1.

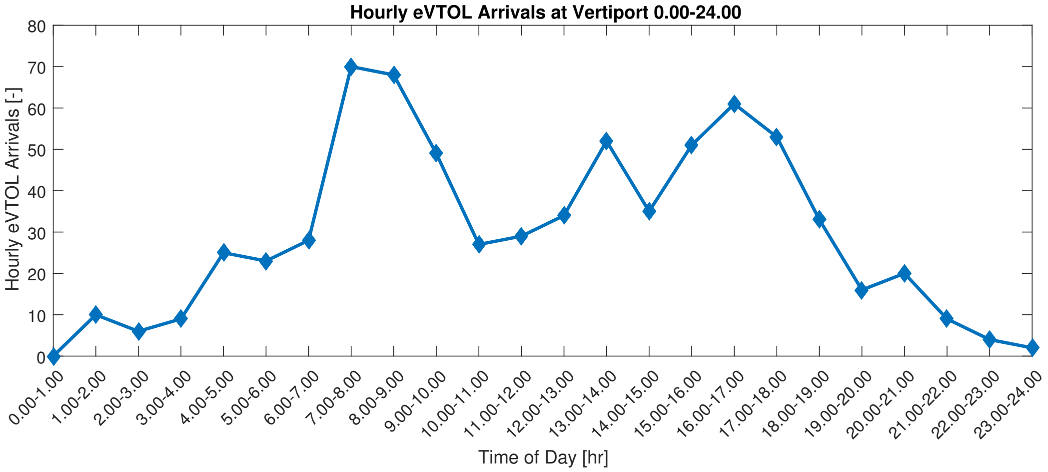

Figure 8.1: Hourly eVTOL Arrivals at a Vertiport with Double Landing Pad using Hover and Rolling Horizon over One Day

8.1. Influence of Constrained Position Shifting

The Constrained Position Shifting (CPS) requirement reduces the number of sequence positions an eVTOL can shift from the FCFS sequence, denoted by parameter K as discussed in Section 4.4.2. A maximum position shift of $K = 2$ is assumed during the case study on Houston in Chapter 7 because it was observed that in general no more than 2 position shifts are used without this constraint and thus the computational time can be increased. This section analyses the influence of a lower (K=1) and higher (K=3) CPS requirement regarding the resulting eVTOL arrival delay and the required computational time. The results are shown in Table 8.1.

The computational time for different CPS constraints in Table 8.1 shows that the chosen baseline value is most computationally efficient. For CPS $K = 3$ the high required time to solve the problem is explained by the in-

Table 8.1: Results for Constrained Position Shifting Sensitivity using a Double Landing Pad with Hover and Rolling Horizon

Time of Day	**Requirement**	**G**	**Comp. Time [s]**	**Total Delay [s]**	**Max Delay [s]**	**Average Delay [s]**	**Using Divert?**	**Using Hover?**
0:00-24:00	CPS K=1	715	20501	15910	251	22	Yes	No
0:00-24:00	Baseline CPS K=2	715	18477	15932	309	22	Yes	No
0:00-24:00	CPS K=3	715	22127	16672	263	23	Yes	No

creased number of decision variables in the optimisation (approx. 1500 more). However, for CPS $K = 1$ the number of decision variables is reduced compared to the baseline model. The increased computational time here results from the bigger challenge for the scheduler to actually find a feasible solution, mostly during the peak arrival demand. It does find a slightly more optimal solution regarding delay due to the reduced number of decision variables, such that the maximum number of nodes in the CPLEX solver is reached at a later computational time and thus further into the optimisation.

This behaviour is also observed in Figures 8.2, 8.3 and 8.4 showing the results for the arrival demand in Figure 8.1 at a double landing pad using hover and rolling horizon for different CPS requirements. The hourly maximum delay in Figure 8.2 shows that an increased CPS K leads to slightly higher hourly maximum delay only during peak hours. The reversed is expected because more efficient sequencing is possible for higher CPS K. Now if the eVTOL arrivals are dense and the scheduling is critical, an increased number of decision variables leads to a similar or less optimal solution because the maximum number of nodes in the iteration is reached earlier. Besides, the scheduler optimises the total delay, such that differences in maximum delay can occur for the same total delay. This also explains why the hourly and daily maximum delay is highest for CPS $K = 2$ (realised between 15.00-16.00). The scheduler swapped an eVTOL 2 positions aft to allow 2 other eVTOLs for a faster landing and thus for a total minimal delay, while this is not possible for CPS $K = 1$ and less optimal for CPS $K = 3$.

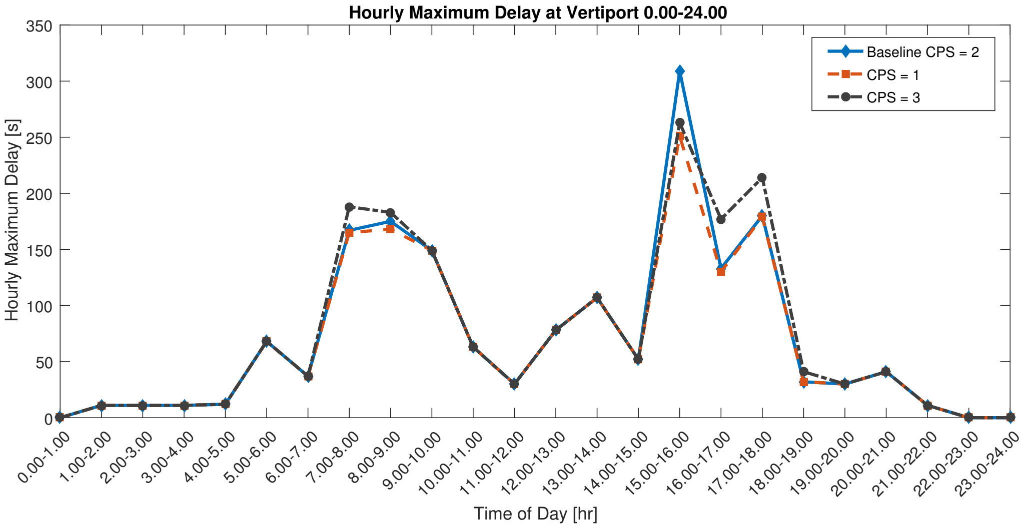

Figure 8.2: Sensitivity of Hourly Maximum Delay at a Vertiport with Double Landing Pad using Hover and Rolling Horizon over One Day to Constrained Position Shifting

The hourly total delay and the cumulative delay in Figure 8.3 and 8.4 show similar behaviour. Again, the results for different CPS constraints only differ during peak hours and thus for critical scheduling. Where CPS $K = 1$ and $K = 2$ show similar results, the increased number of decision variables of CPS $K = 3$ again leads to a slightly less optimal sequencing and scheduling result. From this analysis, it can be concluded that a CPS $K = 2$ is the optimal eVTOL arrival sequencing and scheduling model input considering minimal total delay and minimal computational time.

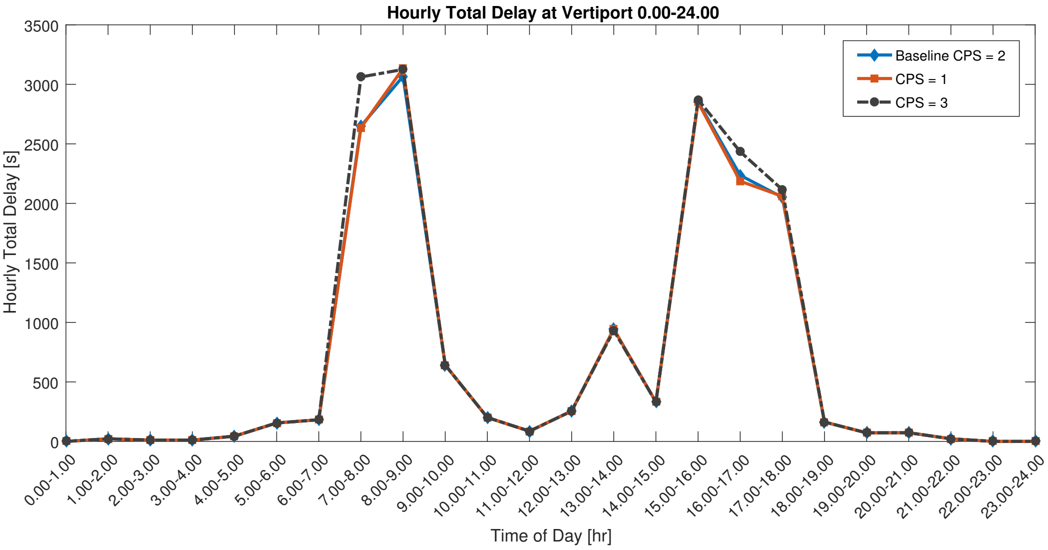

Figure 8.3: Sensitivity of Hourly Total Delay at a Vertiport with Double Landing Pad using Hover and Rolling Horizon over One Day to Constrained Position Shifting

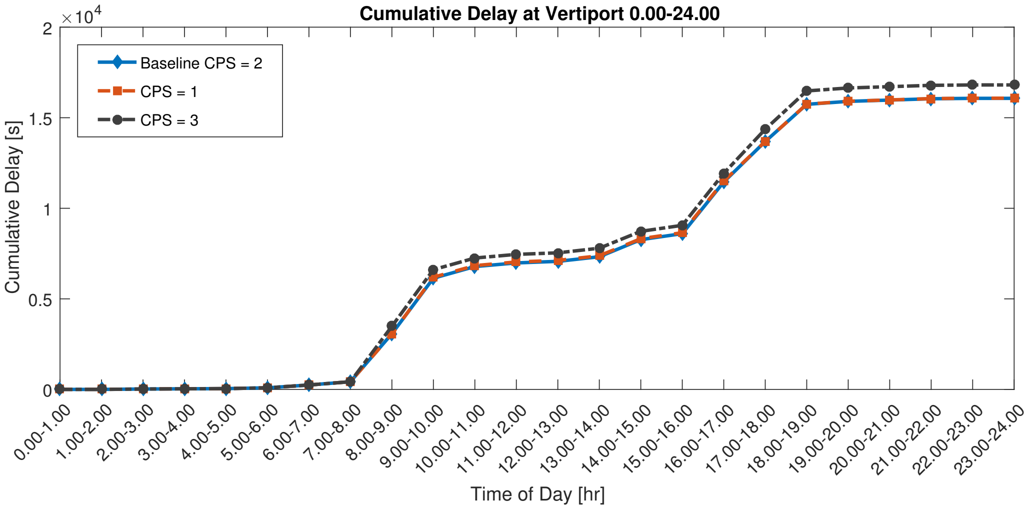

Figure 8.4: Sensitivity of Hourly Cumulative Delay at a Vertiport with Double Landing Pad using Hover and Rolling Horizon over One Day to Constrained Position Shifting

8.2. Influence of Time Separation

The time separation requirement ensures sufficient separation between the arriving eVTOLs (see Section 4.4.2) based on the rotor wake interactions, down-wash interactions and availability of the landing pad. The baseline results for the eVTOL arrival sequencing and scheduling of daily eVTOL arrivals in Houston at a double landing pad using hover and rolling horizon are obtained for a time separation requirement of $90s$ as explained in Subsection 3.1.4. This section analysis the results using the same input and model for different time separation Δt_{sep} requirements, because research is yet to be performed on required eVTOL separation in final approach. The results are shown in Table 8.2.

Table 8.2: Results for Time Separation Sensitivity using a Double Landing Pad with Hover and Rolling Horizon

Time of Day	Requirement	G	Comp. Time [s]	Total Delay [s]	Max Delay [s]	Average Delay [s]	Using Divert?	Using Hover?
0:00-24:00	$\Delta t_{sep} = 60s$	715	7867	450	117	6	Yes	No
0:00-24:00	$\Delta t_{sep} = 80s$	715	19359	10520	191	15	Yes	No
0:00-24:00	Baseline $\Delta t_{sep} = 90s$	715	18477	15932	309	22	Yes	No
0:00-24:00	$\Delta t_{sep} = 100s$	715	38490	25562	279	36	Yes	Yes (3x)

Although the number of decision variables does not change with a different time separation input, an increase in computational time is observed for an increasing Δt_{sep}. Like described in Section 8.1, this results from an increasing challenge to find a feasible and optimal eVTOL arrival sequence and schedule. A $60s$ separation is already ensured in low to mid arrival demand and thus easy and fast to solve, while a $100s$ time separation is close to infeasibility during high peak arrival demand. The latter also results in a need to assign hover to 3 eVTOLs to ensure landing of all eVTOLs according to the requirements. This results in higher computational time due to column generation iterations.

For the daily eVTOL arrivals shown in Figure 8.1, the hover is performed during the morning peak hour (8.00-9.00) which results in a high hourly maximum delay as observed in Figure 8.5. This figure also shows that the maximum delay per hour is highly influenced by increasing the time separation requirements, which is expected as eVTOLs have to absorb more delay to fulfil the requirements. The highest maximum delay is however observed for $\Delta t_{sep} = 90s$. This results from optimising for a minimum total delay, such that in some cases a sequence swap and thus absorption of high delay by one eVTOL is in total more beneficial than spreading delay over multiple eVTOLs.

A similar delay spread is observed in Figures 8.6 and 8.7 showing the total delay results for the arrival demand in Figure 8.1 at a double landing pad for different time separation requirements. As expected, more delay needs to be absorbed if more time between each eVTOL arrival is required. For a Δt_{sep} increase of $20s$ (80-$100s$), the delay even increases by more than 100%. Therefore, thorough research on the exact time separation needs for each eVTOL type is required. In this way, unnecessary and redundant time separation can be avoided, such that the delay per eVTOL can be decreased. Depending on maximum arrival delay standards, the vertiport landing capacity can then be increased to its maximum.

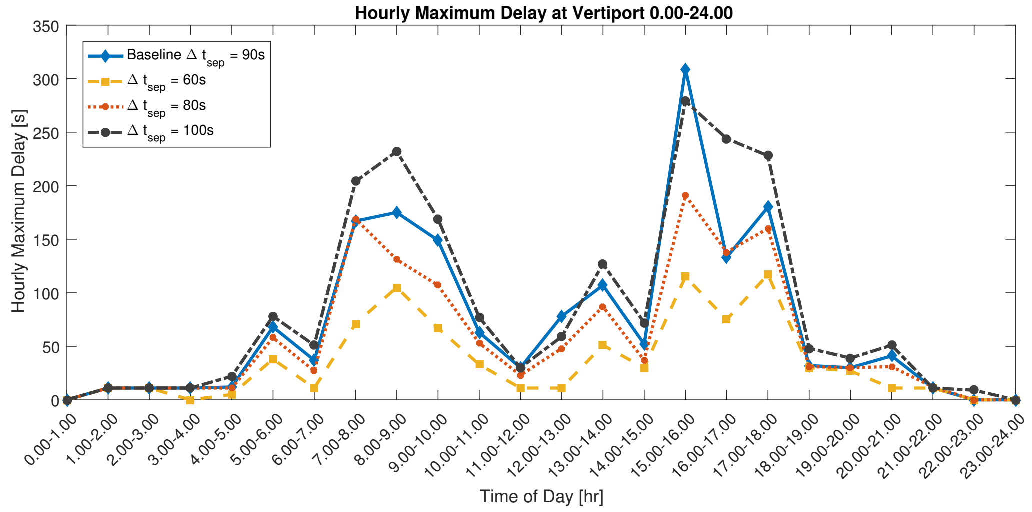

Figure 8.5: Sensitivity of Hourly Maximum Delay at a Vertiport with Double Landing Pad using Hover and Rolling Horizon over One Day to Time Separation Requirement

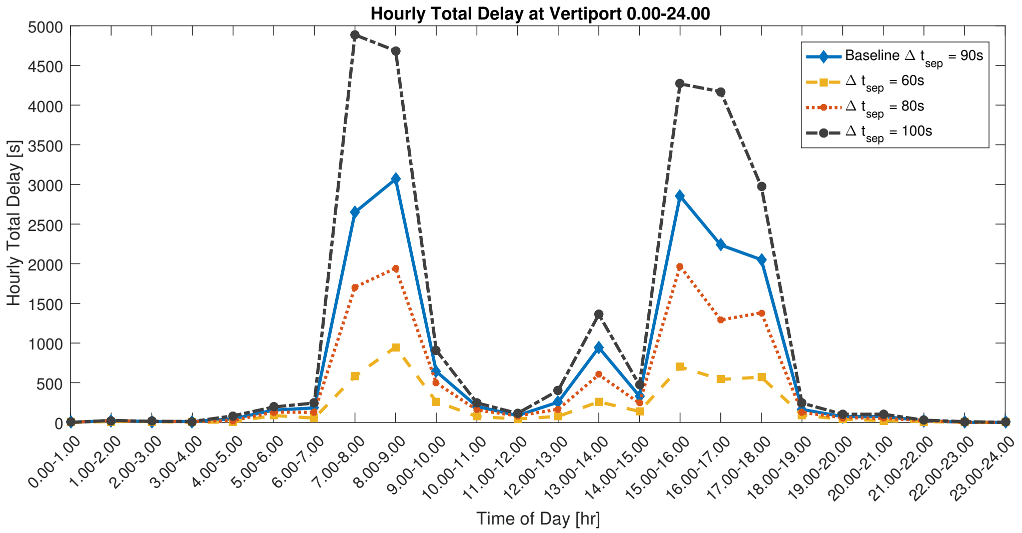

Figure 8.6: Sensitivity of Hourly Total Delay at a Vertiport with Double Landing Pad using Hover and Rolling Horizon over One Day to Time Separation Requirement

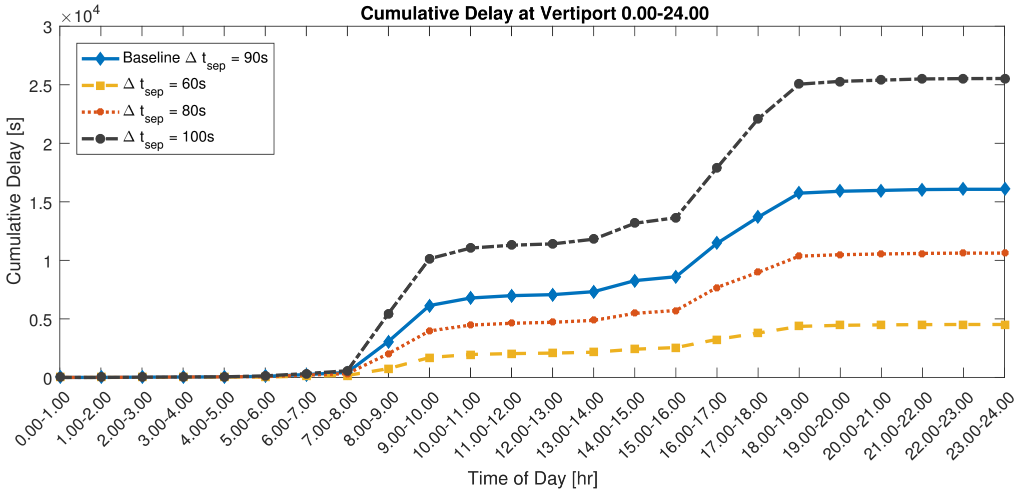

Figure 8.7: Sensitivity of Cumulative Delay at a Vertiport with Double Landing Pad using Hover and Rolling Horizon over One Day to Time Separation Requirement

8.3. Influence of Rolling Horizon Period Length

The rolling horizon (RH) algorithm is applied to solve the eVTOL arrival sequencing and scheduling problem for a higher computational efficiency as explained in Section 4.4.3. Using a shorter rolling horizon period,

Table 8.3: Results for Rolling Horizon Period Sensitivity using a Double Landing Pad with Hover and Rolling Horizon

Time of Day	Rolling Horizon	G	Comp. Time [s]	Total Delay [s]	Max Delay [s]	Average Delay [s]	Using Divert?	Using Hover?
0:00-24:00	RH = $5min$	715	1653	15965	252	22	Yes	No
0:00-24:00	RH = $10min$	715	10813	16751	263	23	Yes	No
0:00-24:00	Baseline RH = $15min$	715	18477	15932	309	22	Yes	No
0:00-24:00	RH = $20min$	715	36495	16423	252	23	Yes	No

defined in Figure 4.5, means that fewer eVTOLs are considered per arrival sequencing and scheduling optimisation. Therefore, the number of decision variables is lower per optimisation and thus the total computational time. This is clearly observed in the results in Table 8.3 and Figure 8.8.

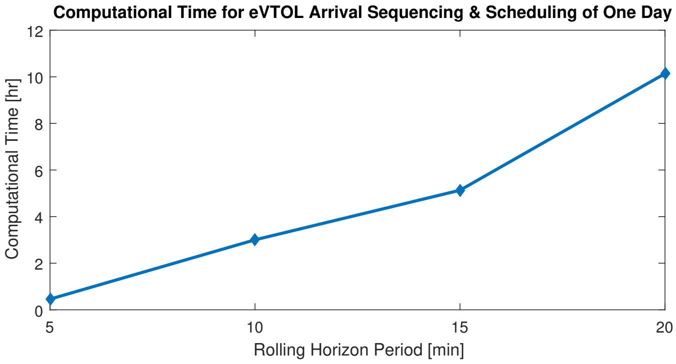

Figure 8.8: Sensitivity of Computational Time required to solve Double Landing Pad using Hover and Rolling Horizon over One Day to Rolling Horizon Period

On the other hand, the eVTOL delay is expected to increase slightly for a shorter rolling horizon period due to the reduction of the possibilities to minimise delay, e.g. sequencing swapping and landing pad choice compared to the other eVTOL arrivals. This behaviour is observed for $RH = 5$min and $RH = 10$min, but the reversed is true for $RH = 20$min as observed in Table 8.3 and Figures 8.9 and 8.10. The difference between the hourly maximum and total delay results is only observed during the high arrival demand at peak hours, while the maximum and total delay off-peak are similar for different RH period lengths. Also the cumulative delay over an entire day is similar for each rolling horizon period length as observed in Figure 8.11.

The slight differences in maximum and total delay during peak for the short RH periods (5min, 10min) are caused by the short optimisation window that reduces the options of the scheduler. For the longer RH period (20min), the higher hourly maximum delay is a result of the higher amount of decision variables such that the maximum amount of nodes is reached before the best solution is found. Besides, it can be caused by the increased sequence swapping and landing pad choice options, such that e.g. one eVTOL might absorb a high delay to prioritise other eVTOLs and add to the same total delay.

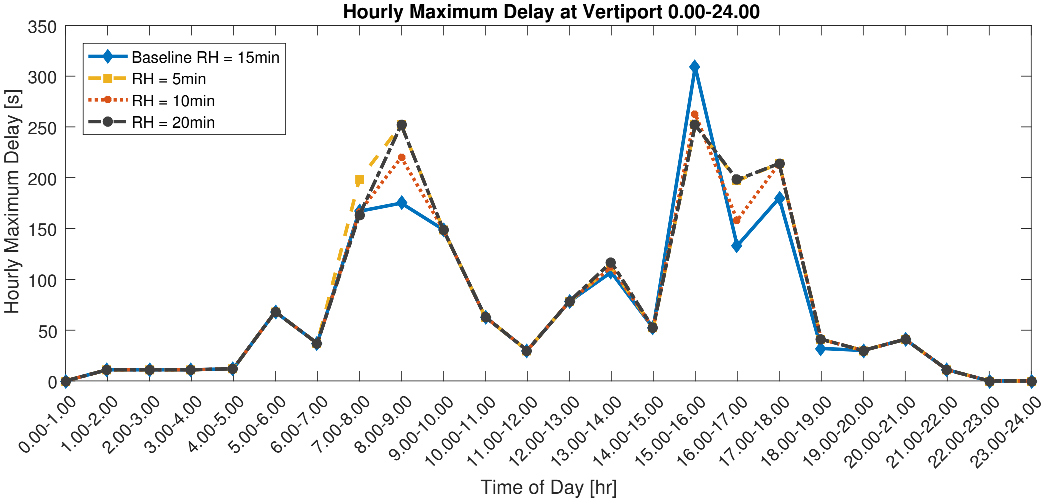

Figure 8.9: Sensitivity of Hourly Maximum Delay at a Vertiport with Double Landing Pad using Hover and Rolling Horizon over One Day to Rolling Horizon Period

Although the maximum delay for an RH period of 5min is higher during peak hours compared to the baseline results, it is most beneficial with respect to computational efficiency and does not significantly affect the hourly total delay and daily cumulative delay. Therefore, it is possible and recommended to solve the on-demand eVTOL arrival sequencing and scheduling for a low computational time using a short RH period length. This is also in line with the short on-demand eVTOL arrival interval compared to commercial aviation, where the baseline 15min is obtained from.

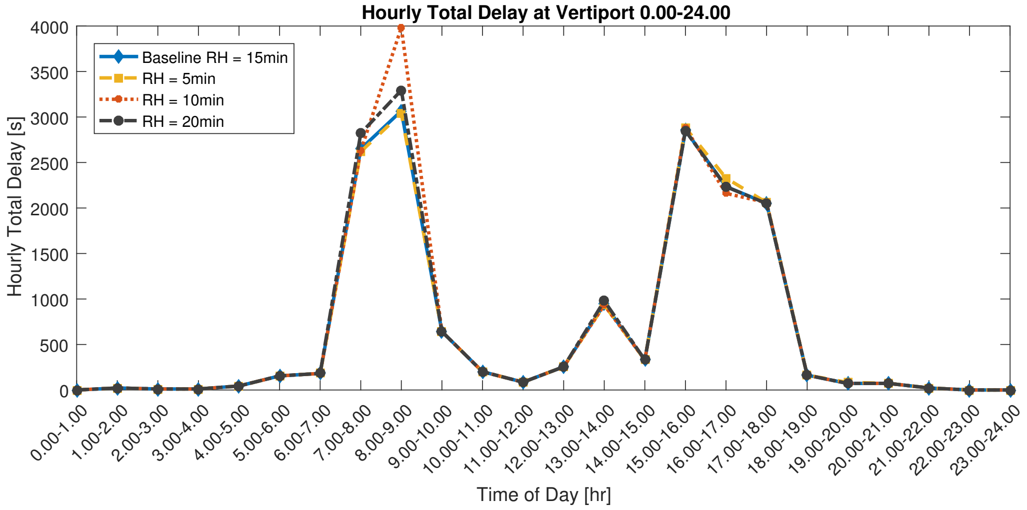

Figure 8.10: Sensitivity of Hourly Total Delay at a Vertiport with Double Landing Pad using Hover and Rolling Horizon over One Day to Rolling Horizon Period

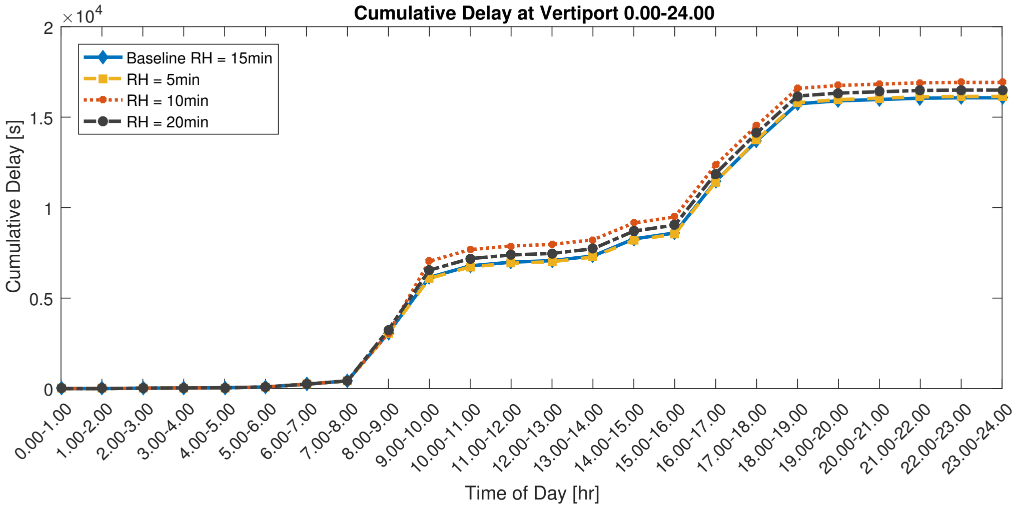

Figure 8.11: Sensitivity of Cumulative Delay at a Vertiport with Double Landing Pad using Hover and Rolling Horizon over One Day to Rolling Horizon Period

8.4. Influence of Battery State of Charge Input

This section discusses the sensitivity of the eVTOL arrival sequencing and scheduling model to the initial battery SOC input by changing the mean μ of its normal distribution. Table 8.4 shows similar behaviour for the computational time as for the CPS sensitivity analysis. The computational time increases due to an increased complexity to find a solution and a required column generation for hover as seen for $\mu = 25\%$.

Table 8.4: Results for Battery SOC Sensitivity using a Double Landing Pad with Hover and Rolling Horizon

Time of Day	Requirement	G	Comp. Time [s]	Total Delay [s]	Max Delay [s]	Average Delay [s]	Using Divert?	Using Hover?
0:00-24:00	SOC $\mu = 25\%$	715	23586	16037	251	22	Yes	Yes (1x)
0:00-24:00	Baseline SOC $\mu = 30\%$	715	18477	15932	309	22	Yes	No
0:00-24:00	SOC $\mu = 35\%$	715	26470	16459	244	23	Yes	No

The maximum delay in Table 8.4 and Figure 8.12 shows to be impacted by the SOC, but a clear trend cannot be distinguished. Again, the solver optimises the total delay, so several optimal total delay solutions can lead to different delay distributions over the eVTOLs. However, the table presents that hover is needed once compared to never for higher SOC values. This indicates that an eVTOL with critical SOC has required another eVTOL to wait in hover.

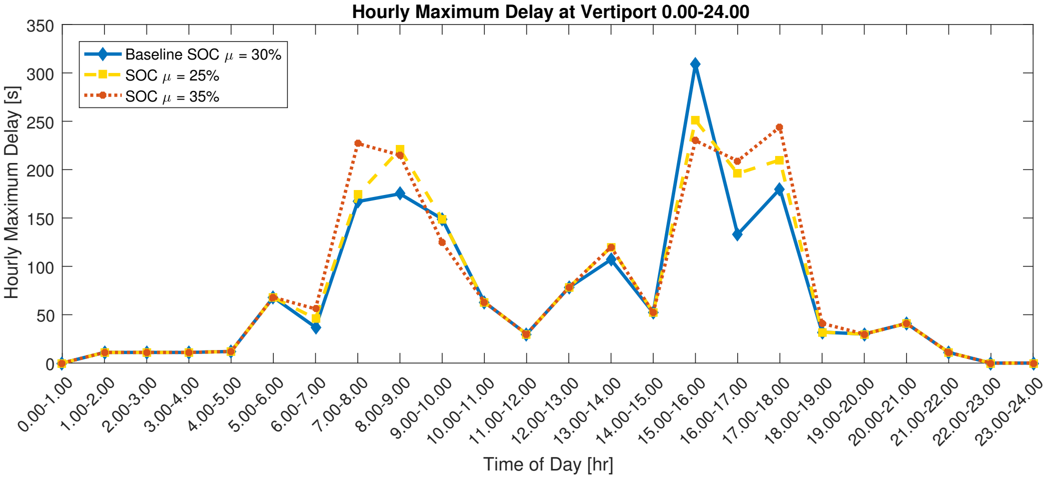

Figure 8.12: Sensitivity of Hourly Maximum Delay at a Vertiport with Double Landing Pad using Hover and Rolling Horizon over One Day to Battery SOC Input

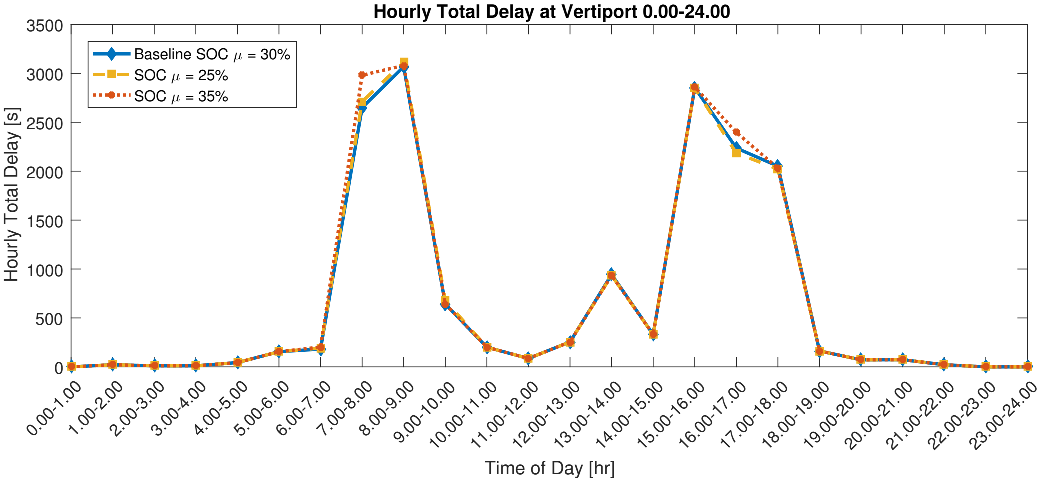

Figure 8.13: Sensitivity of Hourly Total Delay at a Vertiport with Double Landing Pad using Hover and Rolling Horizon over One Day to Battery SOC Input

On the other hand, the total and cumulative delay are only slightly impacted by different SOC values as shown in Figure 8.13 and 8.14. The cumulative delay for a SOC of $\mu = 35\%$ is higher because there are more feasible solutions available such that the maximum number of nodes in the optimisation is reached earlier. From this, it can be concluded that the SOC mainly influences the distribution of the delay over the eVTOLs.

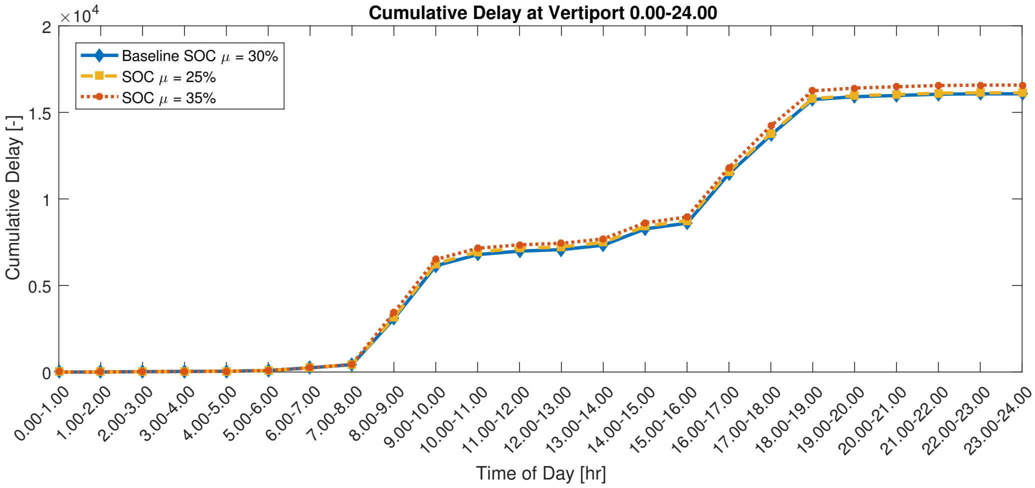

Figure 8.14: Sensitivity of Cumulative Delay at a Vertiport with Double Landing Pad using Hover and Rolling Horizon over One Day to Battery SOC Input

9

Verification and Validation

To ensure that the eVTOL arrival sequencing and scheduling model as discussed in Chapter 4 performs the computations correctly, verification is done. Also, model validation is performed to check if the model correctly represents and solves the real-life situation. The eVTOL arrival sequencing and scheduling model verification and validation are described in Section 9.1 and 9.2, respectively.

9.1. Verification

The results for the eVTOL arrival trajectory optimisation in Module 1 are obtained from an existing model [5] and commercially available GPOPS-II, which are both already verified throughout the design process. Besides, all output is checked to comply with the initial and final conditions for the time, state and control variables. Also, all output needs to be realistic, e.g. no extremely high velocities, negative time, positive vertical speed in descent, etc.

The eVTOL flight dynamics computations from Module 2a are verified with the outcome of the arrival trajectory optimisation. The results for the power required P_r can be converted to the energy E output of the trajectory optimisation using the approximation of the integration in Equation 9.1 for each flight phase N. Besides, the flight dynamics computations are performed for one arrival trajectory by hand and compared with the results from MATLAB. Module 2b on battery prognostics are verified in the same way and checked for a realistic result with other battery research publications.

$$E = \int P_r(t)dt = \sum_{n=1}^{N} P_r(t_n) \cdot t_n \tag{9.1}$$
$$E = P_r(N=1) \cdot t_{N=1} + P_r(N=2) \cdot t_{N=2} + P_r(N=3) \cdot t_{N=3} + P_r(N=4) \cdot t_{N=4}$$

The final eVTOL arrival sequencing and scheduling in Module 3 is verified throughout the stages of development. The first version of the mixed-integer linear program is simulated and checked using the formulation and test set in [49]. Afterwards, the model is extended for eVTOL arrivals specifically such that the proof of concept as presented in Section 6.4 is obtained. Those results are verified by manually checking all constraints, such that times are non-negative, the choice of sequence and approach fix coincides with the RTA and z_{pq} outcome and the RTA results comply with the RTA window of each eVTOL and the separation requirements. The compliance with the RTA window also proofs that eVTOLs with a low battery status were prioritised. The eVTOL arrival sequencing and scheduling model extensions that are created after the proof of concept, are verified with the results of the previous models as also described in Sections 7.1 and 7.2. Besides, each model is equipped with three functions that automatically check the results for each eVTOL regarding the compliance with the RTA window, sufficient time separation from all other eVTOLs that land at the same landing pad and the coincidence of the approach fix selection and z_{pq} parameter.

At last, the eVTOL arrival demand model in Module 4 has been verified using the research that proposes the demand distribution [54].

9.2. Validation

Because eVTOL operations in UAM are yet a principle of the future, no historical datasets or flight tests can be performed to validate the eVTOL arrival sequencing and scheduling model. Therefore, the eVTOL arrival concept of operations and arrival trajectories are validated by talking to experts that work on the development of UAM or eVTOL designs [20]. Also, valuable feedback on the feasibility of the concept and trajectories was obtained after presenting the first part of this research at the Digital Aviation Systems Conference in London in September 2018 [67]. The battery prognostics model is also discussed with experts in the field of electric aircraft propulsion [62, 68].

The total eVTOL arrival sequencing and scheduling model is validated with the case study in Chapter 7 on the expected eVTOL arrivals in Houston, TX, USA as published in [54] and by the sensitivity analysis in Chapter 8, respectively. The application of the rolling horizon algorithm was also validated at the Digital Aviation Systems Conference. Besides, the type of arrival sequencing and scheduling model as presented in this research has already been validated for commercial aviation.

10

Conclusions and Recommendations

10.1. Conclusion

Urban Air Mobility (UAM) is a principle that uses electric Vertical Take-Off and Landing (eVTOL) vehicles to reduce ground traffic congestion by enabling rapid flight between vertiports on demand of the passenger. The eVTOL vertiport arrival phase is found to be the most safety-critical flight phase with high air traffic density and limited battery energy. Therefore, the research question for this thesis has been defined as: *How can on-demand eVTOL aircraft arriving at a vertiport be sequenced and scheduled for minimum delay considering limited battery power?*

The answer to the research question has been found in two main steps. Firstly, a concept of operations for the airspace design around a vertiport with a single or double landing pad has been proposed based on the EHANG-184 multi-rotor eVTOL. A final approach area with a standard eVTOL arrival trajectory and two arrival metering fixes has been introduced. Outside of the final approach area, the scheduled delay is absorbed in the corresponding shallow descent, by selecting an approach fix divert or, only if necessary, in hover on the terminal area boundary. The time separation requirement between eVTOLs has been determined at $90s$ to avoid flying into the vertical landing funnel at the same time and guarantee landing pad clearance.

Secondly, a novel eVTOL arrival sequencing and scheduling model has been created that determines the landing time and sequence for eVTOLs arriving at a vertiport. The proposed mixed-integer linear program ensures eVTOL separation and selects the arrival route and corresponding landing pad for minimum total delay. It uses the input of an energy-efficient arrival trajectory optimisation and battery prediction framework to determine the feasibility of each landing time per eVTOL regarding flight performance and battery status. A column generation algorithm has been applied to enable delay absorption in hover. Besides, a position shifting constraint with respect to the first-come-first-serve sequence and a rolling horizon algorithm have been implemented to reduce the computational time of the model.

The eVTOL arrival concept of operations and sequencing and scheduling model have been validated using a case study on eVTOL arrivals in the envisioned hexagonal vertiport network of Houston, TX, USA. The corresponding eVTOL arrival demand model showed high peaks at the commuter rush hours and low demand at night and was solved for the network centre hub. It has been concluded that the double landing pad concept has a higher capacity than the single landing pad vertiport, also when hover is applied. Delay larger than 6 minutes can occur for eVTOLs arriving at a single landing pad during off-peak periods around noon, while peak periods cannot be served. At a double landing pad, the scheduled eVTOL delay is likely to stay within 1 minute (94%) or 3 minutes (96%) when arriving during peak or off-peak, respectively. It has been concluded that the maximum eVTOL arrival capacity at a double landing pad vertiport is approximately 60 eVTOLs/hr.

From the sensitivity analysis, it has been concluded that reducing or increasing the allowed position shifts did not significantly influence the computational time nor the delay results. The rolling horizon period length of

15 minutes has been chosen as a baseline, where a 5 minute period has shown to be 10 times more computationally efficient for a similar daily cumulative delay result. A period of 5 minutes represents the on-demand service of UAM and allows each set of arrivals to be solved real-time. The arrival sequencing and scheduling results and computational time have also shown to be negatively impacted by increasing the time separation requirement. For a time separation increase of $20s$ (80-$100s$), the daily cumulative delay increases by more than 100% and the computational time doubles. Changing the initial battery eVTOL state of charge presented similar computational efficiency and cumulative delay, thus mainly impacted the distribution of the delay over the eVTOLs.

The proposed concept of operations and eVTOL arrival sequencing and scheduling algorithm provide a potential solution framework to support safe and efficient on-demand arrivals in UAM. Besides, this algorithm and the delay forecasts can be used as a baseline for future research on optimal UAM arrival scheduling and airspace design.

10.2. Recommendations

To use the presented eVTOL arrival sequencing and scheduling model optimally in further research, the following is recommended for each module. First of all, the accuracy of the eVTOL arrival trajectory optimisation and the battery prognostics model can be increased by eVTOL flight testing to check all assumptions made and to calibrate the models. Besides, adding an objective that considers noise abatement and the privacy of citizens would make the trajectory optimisation more attractive to the challenging UAM market. A double landing pad concept with a constraint position shift of 2 and a rolling horizon period of 5 minutes is recommended to benefit from a maximum arrival capacity, minimal delay and lowest computational time. The time separation requirement should be accurately determined from flight testing eVTOLs, such that only minimal required delay is scheduled.

Then, it is recommended to further validate the presented eVTOL arrival sequencing and scheduling model. Other eVTOL types than the EHANG-184, such as tilt wing eVTOLs, and their flight dynamics characteristics should be entered into the trajectory optimisation and battery prognostics modules. Besides, it is advised to find the arrival schedule for eVTOL arrival demand models for different vertiport networks, e.g. in which the hub is not centred or there is one main arrival route.

The following is suggested to extend the eVTOL arrival sequencing and scheduling model. Stochastic influences should be incorporated, e.g. weather and wind conditions, sudden vertiport closure and unexpected airspace intruders. At last, the algorithm should be incorporated with other departure scheduling and conflict detection and resolution models to reach the highest efficiency in Urban Air Mobility and enable autonomous flight.

Bibliography

[1] INRIX. INRIX global traffic scorecard. `http://inrix.com/scorecard/`. Accessed on June-2018.

[2] Uber Elevate. Fast-forwarding to a future of on-demand urban air transportation. Technical report, Uber Elevate Whitepaper, 2016.

[3] V. Chibuogu Nneji, A. Stimpson, M. Cummings, and K. Goodrich. Exploring concepts of operations for on-demand passenger air transportation. In *Proceedings of 17th AIAA Aviation Technology, Integration, and Operations Conference*, pages 1–12, 2017.

[4] P. Vascik and J. Hansman. Constraint identification in on-demand mobility for aviation through an exploratory case study of los angeles. In *Proceedings of 17th AIAA Aviation Technology, Integration, and Operations Conference*, pages 1–25, 2017.

[5] P. Pradeep and P. Wei. Energy efficient arrival with RTA constraint for urban eVTOL operations. In *Proceedings of 2018 AIAA Aerospace Sciences Meeting*, pages 1–13, 2018.

[6] NASA. Small Business Innovation Research (SBIR) & Small Business Technology Transfer (STTR). Technical report, NASA, California, USA, 2018.

[7] I.C. Kleinbekman. Literature study for on-demand arrival traffic sequencing and scheduling in urban air mobility using eVTOL aircraft. Technical report, Delft University of Technology, the Netherlands, 2018.

[8] I. Matamoros. Lilium. Faculty Lunch Lecture Presentation.

[9] EHANG184. EHANG184 autonomous aerial vehicle specs. `http://www.ehang.com/ehang184/specs/`. Accessed on March-2018.

[10] Vertical Flight Society. News on electric vertical take-off and landing (eVTOL) concepts. `http://evtol.news/`. Accessed on June-2018.

[11] Drone Industry Insights. Flying cars, air-taxis, passenger drones – an industry snapshot. `https://www.droneii.com/flying-cars-an-industry-snapshot`. Last updated on May-2018.

[12] K. Dalamagkidis, K.P. Valavanis, and L.A. Piegl. *On Integrating Unmanned Aircraft Systems into the National Airspace System*. Springer, 2^{nd} edition, 2012.

[13] P. Kopardekar, J. Rios, T. Prevot, M. Johnson, J. Jung, and J. Robinson. Unmanned aircraft system traffic management (UTM) concept of operations. In *Proceedings of 16th AIAA Aviation Technology, Integration, and Operations Conference*, pages 1–16, 2016.

[14] C. Bosson and T.A. Lauderdale. Simulation evaluations of an autonomous urban air mobility network management and separation service. In *Proceedings of 2018 Aviation Technology, Integration, and Operations Conference*, page 3365, 2018.

[15] M.A. Patterson and A.V. Rao. GPOPS-II: A MATLAB software for solving multiple-phase optimal control problems using hp-adaptive gaussian quadrature collocation methods and sparse nonlinear programming. *ACM Transactions on Mathematical Software (TOMS)*, 41(1):1:1–1:37, 2014.

[16] G. Cuong Chi, B. Bole, E. Hogge, S. Vazquez, M. Daigle, J. Celaya, A. Weber, and K. Goebel. Battery charge depletion prediction on an electric aircraft. In *Proceedings of Annual Conference of the Prognostics and Health Management Society 2013*, pages 1–11, 2013.

[17] B. Bole, C. Teubert, Q. Cuong Chi, E. Hogge, S. Vazquez, K. Goebel, and G. Vachtsevanos. SIL/HIL replication of electric aircraft powertrain dynamics and inner-loop control for V&V of system health management routines. In *Proceedings of Annual Conference of the Prognostics and Health Management Society 2013*, 2013.

[18] B. Bole, M. Daigle, and G. Gorospe. Online prediction of battery discharge and estimation of parasitic loads for an electric aircraft. *ESC*, 2:5S2P, 2014.

[19] A.H. Alnaqeb, Y. Li, Y. Lui, P. Pradeep, J. Wallin, C. Hu, S. Hu, and P. Wei. Online prediction of battery discharge and flight mission assessment for electrical rotorcraft. In *Proceedings of 2018 AIAA Aerospace Sciences Meeting*, page 2005, 2018.

[20] H. Hilaire and M. Ausman. Airbus A^3 Vahana company visit. Personal communication on 21-May-2018.

[21] G.L. Plett. *Equivalent-Circuit Methods*, volume II of *Battery Management Systems*. Artech House, 2016.

[22] H. Erzberger and E. Itoh. Design principles and algorithms for air traffic arrival scheduling. Technical report, NASA Ames Research Center, California and Electronic Navigation Research Institute, Tokyo, Japan, 2014.

[23] R. de Neufville and A.R. Odoni. *Airport Systems: Planning, Design and Management*. McGraw-Hill Education LLC, 2^{nd} edition, 2003.

[24] Y. Cao, T. Kotegawa, and J. Post. Evaluation of continuous descent approach as a standard terminal airspace operation. In *Proceedings of 9th USA/Europe Air Traffic Management R&D Seminar*, 2011.

[25] J. Hoekstra and J. Ellerbroek. AE4321 Air Traffic Management - lecture 2 structure of airspaces. Lecture slides, 2017.

[26] D. Ivanescu, C. Shaw, C. Tamvaclis, and T. Kettunen. Models of air traffic merging techniques: Evaluating performance of point merge. In *Proceedings of 9th Aviation Technology, Integration, and Operations Conference (ATIO)*, pages 1–10, 2009.

[27] L. Boursier, B. Favennec, E. Hoffman, A. Trzmiel, F. Vergne, and K. Zeghal. Merging arrival flows without heading instructions. In *Proceedings of USA/Europe Air Traffic Management Research and Development Seminar*, pages 1–8, 2007.

[28] P. Pradeep and P. Wei. Energy optimal speed profile for arrival of tandem tilt-wing eVTOL aircraft with RTA constraint. In *Submitted to 2018 IEEE CSAA Guidance, Navigation and Control Conference*, pages 1–6, 2018.

[29] SKYbrary. Vortex ring. `https://www.skybrary.aero/index.php/Vortex_Ring`. Last updated on May-2018.

[30] M. Nolan. *Fundamentals of Air Traffic Control*. Cengage Learning, 2010.

[31] J.E. Beasley, J. Sonander, and P. Havelock. Scheduling aircraft landings at London Heathrow using a population heuristic. *Journal of the Operational Research Society*, 52(5):483–493, 2001.

[32] J. Desai and R. Prakash. Flight sequencing and scheduling: A data-driven approach. In *Proceedings of Industrial and Systems Engineering Research Conference*, pages 764–769, 2016.

[33] J.E. Beasley, M. Krishnamoorthy, Y.M. Sharaiha, and D. Abramson. Scheduling aircraft landings - the static case. *Transportation Science*, 34(2):180–197, 2000.

[34] C. Potts and J. Benell. A review of airport runway optimization. Technical report, School of Management, University of Southampton, UK supported by EUROCONTROL, 2009.

[35] B. Chandran and H. Balakrishnan. A dynamic programming algorithm for robust runway scheduling. In *Proceedings of 2007 American Control Conference*, pages 1161–1166, July 2007.

[36] G. Sölveling, S. Solak, J.P. Clarke, and E.L. Johnson. Scheduling of runway operations for reduced environmental impact. *Transportation Research Part D: Transport and Environment*, 16(2):110 – 120, 2011.

[37] M. Mesgarpour, C.N. Potts, and J. A. Bennell. Models for aircraft landing optimization. In *Proceedings of the 4th International Conference on Research in Air Transportation*, pages 1–4, 2010.

[38] I. Anagnostakis, J.P. Clarke, D. Böhme, and U. Völckers. Runway operations planning and control: Sequencing and scheduling. *Journal of Aircraft*, 38(6):988–996, 2001.

[39] G. C. Carr, H. Erzberger, and F. Neuman. Fast-time study of airline-influenced arrival sequencing and scheduling. *Journal of Guidance, Control, and Dynamics*, 23(3):526–531, 2000.

[40] A. Pawelek, P. Lichota, R. Dalmau, and X. Prats. Arrival traffic synchronisation with required time of arrivals for fuel-efficient trajectory. In *Proceedings of the 17th ATIO-AIAA Aviation Technology, Integration, and Operations Conference*, pages 1–14, 2017.

[41] P. Belobaba, A. Odoni, and C. Barnhart. *The Global Airline Industry*. John Wiley & Sons, 2009.

[42] SKYbrary. Wake vortex generation by helicopters. `https://www.skybrary.aero/index.php/Wake_Vortex_Generation_by_Helicopters`. Last updated on Aug-2017.

[43] K.H. Goodrich and B. Barmore. Exploratory analysis of the airspace throughput and sensitivities of an urban air mobility system. In *Proceedings of 2018 Aviation Technology, Integration, and Operations Conference*, page 3364, 2018.

[44] Y. Hong, B. Choi, and Y. Kim. Two-stage stochastic programming based on particle swarm optimization for aircraft sequencing and scheduling. In *Proceedings of IEEE Intelligent Transportation Systems Transactions*, pages 1–11, 2017.

[45] G. De Maere, J.A.D. Atkin, and E.K. Burke. Pruning rules for optimal runway sequencing. *Transportation Science*, 0(0):1–19, 0.

[46] F.S. Hillier and G.J. Lieberman. *Introduction to Operations Research*. McGraw-Hill International Edition, 10^{th} edition, 2015.

[47] M. Wen. Algorithms of scheduling aircraft landing problem. Technical report, Technical University of Denmark, 2005.

[48] R. Prakash and J. Desai. A data-splitting algorithm for flight sequencing and scheduling on two runways. In *Proceedings of IIE Annual Conference*, pages 764–769, 2017.

[49] C. Guérert, C. Prins, and M. Sevaux. *Applications of optimization with XPress-MP*. Dash Optimization Ltd., 2000.

[50] C.N. Potts and M. Mesgarpour. A review of airport runway optimization. Technical report, University of Southampton, Southampton, UK, 2009.

[51] D'Ariano A. Samà, M. and D. Pacciarelli. Optimal aircraft traffic flow management at a terminal control area during disturbances. *Procedia - Social and Behavioral Sciences*, 54(1):460–469, 2014.

[52] X.B. Hu and W.H. Chen. Genetic algorithm based on receding horizon control for arrival sequencing and scheduling. *Engineering Applications of Artificial Intelligence*, 18(5):633–642, 2005.

[53] J.J. Alonso, H.M. Arneson, J.E. Melton, M. Vegh, C. Walker, and L.A. Young. System-of-systems considerations in the notional development of a metropolitan aerial transportation system. Technical report, Stanford University and NASA Ames Research Center, 2017.

[54] L.W. Kohlman and M.D. Patterson. System-level urban air mobility transportation modeling and determination of energy-related constraints. In *Proceedings of 2018 Aviation Technology, Integration, and Operations Conference*, page 3677, 2018.

[55] J.C. Smith, K. Viken, N.M. Guerreiro, S.M. Dollyhigh, J.W. Fenbert, C.L. Hartmann, and T. Kwa. Projected demand and potential impacts to the national airspace system of autonomous, electric, on-demand small aircraft. In *Proceedings of 12th AIAA Aviation Technology, Integration, and Operations (ATIO) Conference and 14th AIAA/ISSM*, 2012.

[56] G.C. Carr, H. Erzberger, and F. Neuman. Fast-time study of airline-influenced arrival sequencing and scheduling. *Journal of Guidance, Control and Dynamics*, 23(3):526–531, 2000.

[57] G. Solveling. Stochastic programming methods for scheduling of airport runway operations under uncertainty. Technical report, Georgia Institute of Technology, 2012.

[58] A. Rodriguez-Diaz, B. Adenso-Diaz, and P.L. Gonzalez-Torre. Minimizing deviation from scheduled times in a single mixed-operation runway. *Compututers & Operations Research*, 78:193–202, 2017.

[59] W. Johnson. *Rotorcraft Aeromechanics*. Cambridge University Press, 2013.

[60] W. Johnson. *Helicopter Theory*. Courier Corporation, 2012.

[61] The MathWorks. MATLAB and Statistics Toolbox Release 2016a. `https://www.mathworks.com/`. Computer Software, Retrieved on Sep-2016.

[62] F. Oliviero. Flight Performance and Propulsion department meeting on battery prognostics. Personal communication on 8-Nov-2018.

[63] Drone Aviation. Learn module 6 battery. `https://www.dronaaviation.com/learn-module-6-battery/`. Accessed on Aug-2018.

[64] IBM Analytics. CPLEX Optimizer, high-performance mathematical programming solver for linear programming, mixed integer programming, and quadratic program. `www.ibm.com/analytics/data-science/prescriptive-analytics/cplex-optimizer`. Computer Software, Retrieved on Nov-2016.

[65] X. Wang and H. Kopfer. Dynamic collaborative transportation planning: A rolling horizon planning approach. In *Proceedings of Computational Logistics: 4th International Conference*, pages 128–142, 2013.

[66] M. Mitici. AE4466 Monte Carlo simulation of stochastic processes II - lecture 5 poisson process. Lecture slides, 2017.

[67] I.C. Kleinbekman, M.A. Mitici, and P. Wei. eVTOL arrival sequencing and scheduling for on-demand urban air mobility. 2018.

[68] A.H. Alnaqeb. Online prediction of battery discharge and flight mission assessment for electrical rotorcraft. Technical report, Iowa State University, 2017.

A

Guide for MATLAB Code Modules

This appendix shortly describes the MATLAB code modules created specifically for the research on eVTOL arrival sequencing and scheduling by I.C. Kleinbekman.

Trajectory
This module converts and scales the output from the GPOPS-II trajectory optimisation (developed by the authors of [5, 28], see Section 4.1) such that it can be used for visualisation and further computations.

Trajectory Visualisation
This module is used to visualise the results from the GPOPS-II trajectory optimisation.

Power Required
This module uses the eVTOL flight dynamics from Section 4.2 to find the power required to perform each RTA flight trajectory.

SOC Cost
This module uses the power required module and battery computations from Section 4.3 to find the state of charge required to perform each RTA flight trajectory.

Generate Input, Generate Input Day
These functions produce the input for the Houston case study using the demand model in Chapter 5 based on a state and time of the day input, or for the entire day.

RTA SOC
This function computes the latest possible RTA for each eVTOL based on their initial SOC and the results from the SOC Cost module.

LocationK and LocationZ
These functions define the location of decision variables in the MILP tableau (matrix A) for the standard arrival sequencing model and for the simplified model without z_{pq}, respectively.

Branch and Bound, Test Integer
The branch-and-bound function is used to test if the arrival sequencing and scheduling MILP can be solved more efficiently using branch-and-bound. It uses the TestInteger module to determine the new node in the branching tree by determining the non-integer solution with the highest deviation from the closest integer.

Main
This module combines all other modules and builds and solves the arrival sequencing and scheduling MILP. It calls CPLEX [64] linear solver to solve the linear programming problem. Besides, some versions use column generation for hover or rolling horizon algorithm to solve the problems efficiently. Different main module versions are thus available:

- V11 - Single Landing Pad with z_{pq} as in Section 4.4
- V13 - Single Landing Pad without z_{pq} as in Section 4.4.3
- V14 - Single Landing Pad without z_{pq} with hover as in Section 4.4.3
- V15 - Double Landing Pad with hover as in Section 4.5
- V18 - Single Landing Pad with hover and rolling horizon as in Section 4.4.3
- V17 - Double Landing Pad with hover and rolling horizon as in Section 4.5
- VDAY - Double Landing Pad with hover and rolling horizon solving for the entire day (running V17 for the input of an entire day)
- VMC-single - Single Landing Pad with hover and rolling horizon solving the Monte Carlo simulation (running V18 multiple times for different input generations)
- VMC-double - Double Landing Pad with hover and rolling horizon solving the Monte Carlo simulation (running V17 multiple times for different input generations)

Verification RTA window, Z, time separation
These functions are used to verify the results from the main arrival sequencing and scheduling module as described in Section 9.1 automatically.

RTA Visualisation
This module visualises the results from the main arrival sequencing and scheduling module.

B

Detailed Results for eVTOL Arrival Trajectory Optimisation

Table B.1: Results of eVTOL Arrival Trajectory Optimisation for RTA at the Approach Fix of 300s

RTA = 300s at AF	t $[s]$		d $[m]$		h $[m]$		V_x $[m/s]$	V_h $[m/s]$	θ $[rad]$	T $[N]$
	t_0	t_f	d_0	d_f	h_0	h_f				
Cruise till TOD (N=1)	0	**79**	0	**2310**	500	500	0	27.8	0.27	2450
Shallow descent (N=2)	**79**	**300**	**2310**	3500	500	200	**-1.44**	5.88	-0.45	2360
Horizontal FA (N=3)	**300**	**369**	3500	3900	200	200	0	5.88	0.013	2620
Vertical FA (N=4)	**369**	**442**	3900	3900	200	0	2.87	0	-0.45	2350

Table B.2: Results of eVTOL Arrival Trajectory Optimisation for RTA at the Approach Fix of 400s

RTA = 400s at AF	t $[s]$		d $[m]$		h $[m]$		V_x $[m/s]$	V_h $[m/s]$	θ $[rad]$	T $[N]$
	t_0	t_f	d_0	d_f	h_0	h_f				
Cruise till TOD (N=1)	0	**55**	0	**1480**	500	500	0	27.8	0.27	2450
Shallow descent (N=2)	**55**	**400**	**1480**	3500	500	200	**-0.90**	5.88	-0.45	2360
Horizontal FA (N=3)	**400**	**469**	3500	3900	200	200	0	5.88	0.013	2620
Vertical FA (N=4)	**469**	**542**	3900	3900	200	0	2.87	0	-0.45	2350

Table B.3: Results of eVTOL Arrival Trajectory Optimisation for RTA at the Approach Fix of 500s

RTA = 500s at AF	t $[s]$		d $[m]$		h $[m]$		V_x $[m/s]$	V_h $[m/s]$	θ $[rad]$	T $[N]$
	t_0	t_f	d_0	d_f	h_0	h_f				
Cruise till TOD (N=1)	0	**28**	0	**734**	500	500	0	27.8	0.27	2450
Shallow descent (N=2)	**28**	**500**	**734**	3500	500	200	**-0.72**	5.88	-0.45	2360
Horizontal FA (N=3)	**500**	**569**	3500	3900	200	200	0	5.88	0.013	2620
Vertical FA (N=4)	**569**	**642**	3900	3900	200	0	2.87	0	-0.45	2350

Table B.4: Results of eVTOL Arrival Trajectory Optimisation for RTA at the Approach Fix of 525s

RTA = 525s at AF	t [s]		d [m]		h [m]		V_x [m/s]	V_h [m/s]	θ [rad]	T [N]
	t_0	t_f	d_0	d_f	h_0	h_f				
Cruise till TOD (N=1)	0	**21**	0	**550**	500	500	0	27.8	0.27	2450
Shallow descent (N=2)	**21**	**525**	**550**	3500	500	200	**-0.67**	5.88	-0.45	2360
Horizontal FA (N=3)	**525**	**594**	3500	3900	200	200	0	5.88	0.013	2620
Vertical FA (N=4)	**594**	**667**	3900	3900	200	0	2.87	0	-0.45	2350

Table B.5: Optimal eVTOL Arrival Trajectory Results for Different RTA Values inside the Final Approach Area

RTA [s]	**Objective Horizontal Flight Phase** [-]	**Objective Vertical Flight Phase** [-]	**Objective Total Final Approach** [-]
150	11.91	0.7818	12.69
145	11.91	0.6916	12.60
142	**11.91**	**0.6521**	**12.56**
141	11.91	0.6678	12.58
143	11.91	0.6580	12.57

C

Detailed Results for eVTOL Arrival Sequencing & Scheduling

C.1. Detailed Results for eVTOL Arrival Sequencing & Scheduling per eVTOL

Table C.1: Detailed Schedule Results for Input Set 1 Single Landing Pad using z_{pq} at 11.30-12.30 (Off-Peak)

Input Set 1 at 11.30-12.30					**Results for Single Landing Pad using z_{pq}**				
Flight	Origin	ETA$_A$ [s]	ETA$_B$ [s]	SOC$_{init}$ [%]	RTA [s]	$\Delta t_{shallow}$ [s]	$\Delta t_{l,af}$ [s]	AF [-]	Δt_l [s]
1	7	231	220	30.51401	362	0	0	0	0
2	2	273	243	40.64061	452	67	0	0	67
3	3	497	486	19.90593	628	0	0	0	0
4	6	614	625	34.19625	756	0	0	1	0
5	6	699	710	36.22335	846	5	0	1	5
6	3	846	835	28.55853	977	0	0	0	0
7	2	881	851	36.48354	1067	74	0	0	74
8	4	962	973	38.68509	1157	53	0	1	53
9	3	1103	1092	30.13649	1247	13	0	0	13
10	7	1179	1168	24.12815	1337	27	0	0	27
11	4	1225	1236	25.38067	1517	150	0	1	150
12	4	1254	1265	27.99329	1427	31	0	1	31
13	5	1398	1428	23.96314	1607	67	0	1	67
14	7	1587	1576	29.49554	1718	0	0	0	0
15	2	1708	1678	33.35738	1820	0	0	0	0
16	4	1720	1731	29.53667	1910	48	0	1	48
17	6	1764	1775	20.60132	2000	94	0	1	94
18	3	1879	1868	26.04102	2090	80	0	0	80
19	3	1907	1896	26.42322	2180	142	0	0	142
20	5	2147	2177	31.08276	2289	0	0	1	0
21	3	2218	2207	26.23935	2379	30	0	0	30
22	2	2272	2242	24.53318	2469	85	0	0	85
23	3	2379	2368	22.44434	2559	49	0	0	49
24	6	2434	2445	31.6651	2739	163	0	1	163
25	4	2463	2474	28.05997	2649	44	0	1	44
26	7	2624	2613	24.44761	2829	74	0	0	74
27	3	2676	2665	29.57793	2919	112	0	0	112
28	7	2941	2930	26.38107	3072	0	0	0	0
29	2	3130	3100	33.36325	3242	0	0	0	0
30	7	3392	3381	28.95563	3523	0	0	0	0
31	4	3442	3453	36.27844	3613	29	0	1	29
32	5	3511	3541	29.79057	3703	50	0	1	50
33	5	3626	3656	31.1817	3793	25	0	1	25
34	2	3698	3668	27.71068	3883	73	0	0	73
35	5	3734	3764	30.49446	3973	97	0	1	97
36	7	3783	3772	29.68826	4063	149	0	0	149
37	4	4059	4070	28.65655	4201	0	0	1	0
38	3	4083	4072	32.39124	4291	77	0	0	77
39	3	4149	4138	31.23076	4471	191	0	0	191
40	3	4166	4155	31.95871	4381	84	0	0	84
41	7	4334	4323	27.00929	4561	96	0	0	96

Table C.2: Detailed Schedule Results for Input Set 1 Single Landing Pad at 11.30-12.30 (Off-Peak)

Input Set 1 at 11.30-12.30					**Results for Single Landing Pad**				
Flight	Origin	ETA$_A$ [s]	ETA$_B$ [s]	SOC$_{init}$ [%]	RTA [s]	$\Delta t_{shallow}$ [s]	$\Delta t_{l,af}$ [s]	AF [-]	Δt_l [s]
1	7	231	220	30.51401	362	0	0	0	0
2	2	273	243	40.64061	452	67	0	0	67
3	3	497	486	19.90593	628	0	0	0	0
4	6	614	625	34.19625	756	0	0	1	0
5	6	699	710	36.22335	846	5	0	1	5
6	3	846	835	28.55853	977	0	0	0	0
7	2	881	851	36.48354	1067	74	0	0	74
8	4	962	973	38.68509	1157	53	0	1	53
9	3	1103	1092	30.13649	1247	13	0	0	13
10	7	1179	1168	24.12815	1337	27	0	0	27
11	4	1225	1236	25.38067	1427	60	0	1	60
12	4	1254	1265	27.99329	1517	121	0	1	121
13	5	1398	1428	23.96314	1607	67	0	1	67
14	7	1587	1576	29.49554	1718	0	0	0	0
15	2	1708	1678	33.35738	1820	0	0	0	0
16	4	1720	1731	29.53667	1910	48	0	1	48
17	6	1764	1775	20.60132	2000	94	0	1	94
18	3	1879	1868	26.04102	2090	80	0	0	80
19	3	1907	1896	26.42322	2180	142	0	0	142
20	5	2147	2177	31.08276	2289	0	0	1	0
21	3	2218	2207	26.23935	2379	30	0	0	30
22	2	2272	2242	24.53318	2469	85	0	0	85
23	3	2379	2368	22.44434	2559	49	0	0	49
24	6	2434	2445	31.6651	2649	73	0	1	73
25	4	2463	2474	28.05997	2739	134	0	1	134
26	7	2624	2613	24.44761	2829	74	0	0	74
27	3	2676	2665	29.57793	2919	112	0	0	112
28	7	2941	2930	26.38107	3072	0	0	0	0
29	2	3130	3100	33.36325	3242	0	0	0	0
30	7	3392	3381	28.95563	3523	0	0	0	0
31	4	3442	3453	36.27844	3613	29	0	1	29
32	5	3511	3541	29.79057	3703	50	0	1	50
33	5	3626	3656	31.1817	3793	25	0	1	25
34	2	3698	3668	27.71068	3883	73	0	0	73
35	5	3734	3764	30.49446	3973	97	0	1	97
36	7	3783	3772	29.68826	4063	149	0	0	149
37	4	4059	4070	28.65655	4201	0	0	1	0
38	3	4083	4072	32.39124	4471	257	0	0	257
39	3	4149	4138	31.23076	4291	11	0	0	11
40	3	4166	4155	31.95871	4381	84	0	0	84
41	7	4334	4323	27.00929	4561	96	0	0	96

Table C.3: Detailed Schedule Results for Input Set 1 Single Landing Pad at 11.30-12.30 using Rolling Horizon (Off-Peak)

Input Set 1 at 11.30-12.30					**Results for Single Landing Pad. RH**				
Flight	Origin	ETA$_A$ [s]	ETA$_B$ [s]	SOC$_{init}$ [%]	RTA [s]	$\Delta t_{shallow}$ [s]	$\Delta t_{l,af}$ [s]	AF [-]	Δt_l [s]
1	7	231	220	30.51401	362	0	0	0	0
2	2	273	243	40.64061	452	67	0	0	67
3	3	497	486	19.90593	628	0	0	0	0
4	6	614	625	34.19625	756	0	0	1	0
5	6	699	710	36.22335	846	5	0	1	5
6	3	846	835	28.55853	977	0	0	0	0
7	2	881	851	36.48354	1067	74	0	0	74
8	4	962	973	38.68509	1157	53	0	1	53
9	3	1103	1092	30.13649	1247	13	0	0	13
10	7	1179	1168	24.12815	1337	27	0	0	27
11	4	1225	1236	25.38067	1517	150	0	1	150
12	4	1254	1265	27.99329	1427	31	0	1	31
13	5	1398	1428	23.96314	1607	67	0	1	67
14	7	1587	1576	29.49554	1718	0	0	0	0
15	2	1708	1678	33.35738	1820	0	0	0	0
16	4	1720	1731	29.53667	2000	138	0	1	138
17	6	1764	1775	20.60132	1910	4	0	1	4
18	3	1879	1868	26.04102	2090	80	0	0	80
19	3	1907	1896	26.42322	2180	142	0	0	142
20	5	2147	2177	31.08276	2289	0	0	1	0
21	3	2218	2207	26.23935	2379	30	0	0	30
22	2	2272	2242	24.53318	2469	85	0	0	85
23	3	2379	2368	22.44434	2559	49	0	0	49
24	6	2434	2445	31.6651	2649	73	0	1	73
25	4	2463	2474	28.05997	2739	134	0	1	134
26	7	2624	2613	24.44761	2919	164	0	0	164
27	3	2676	2665	29.57793	2829	22	0	0	22
28	7	2941	2930	26.38107	3072	0	0	0	0
29	2	3130	3100	33.36325	3242	0	0	0	0
30	7	3392	3381	28.95563	3523	0	0	0	0
31	4	3442	3453	36.27844	3613	29	0	1	29
32	5	3511	3541	29.79057	3703	50	0	1	50
33	5	3626	3656	31.1817	3793	25	0	1	25
34	2	3698	3668	27.71068	3883	73	0	0	73
35	5	3734	3764	30.49446	3973	97	0	1	97
36	7	3783	3772	29.68826	4063	149	0	0	149
37	4	4059	4070	28.65655	4201	0	0	1	0
38	3	4083	4072	32.39124	4381	167	0	0	167
39	3	4149	4138	31.23076	4291	11	0	0	11
40	3	4166	4155	31.95871	4561	264	0	0	264
41	7	4334	4323	27.00929	4471	6	0	0	6

Table C.4: Detailed Schedule Results for Input Set 1 Double Landing Pad using Hover at 11.30-12.30 (Off-Peak)

Input Set 1 at 11.30-12.30					**Results for Double Landing Pad, Hoover**							
Flight	Origin	ETA$_A$ [s]	ETA$_B$ [s]	SOC$_{init}$ [%]	RTA [s]	$\Delta t_{shallow}$ [s]	$\Delta t_{l,af}$ [s]	AF [-]	$\Delta t_{l,h}$ [s]	Δt_l [s]	RTA$_A$ [s]	RTA$_B$ [s]
1	7	231	220	30.51401	328	0	11	1	0	11	328	0
2	2	273	243	40.64061	340	0	0	0	0	0	0	340
3	3	497	486	19.90593	583	0	0	0	0	0	0	583
4	6	614	625	34.19625	711	0	0	1	0	0	711	0
5	6	699	710	36.22335	801	5	0	1	0	5	801	0
6	3	846	835	28.55853	943	0	11	1	0	11	943	0
7	2	881	851	36.48354	948	0	0	0	0	0	0	948
8	4	962	973	38.68509	1059	0	0	1	0	0	1059	0
9	3	1103	1092	30.13649	1200	0	11	1	0	11	1200	0
10	7	1179	1168	24.12815	1265	0	0	0	0	0	0	1265
11	4	1225	1236	25.38067	1322	0	0	1	0	0	1322	0
12	4	1254	1265	27.99329	1362	0	11	0	0	11	0	1362
13	5	1398	1428	23.96314	1495	0	0	1	0	0	1495	0
14	7	1587	1576	29.49554	1673	0	0	0	0	0	0	1673
15	2	1708	1678	33.35738	1775	0	0	0	0	0	0	1775
16	4	1720	1731	29.53667	1817	0	0	1	0	0	1817	0
17	6	1764	1775	20.60132	1872	0	11	0	0	11	0	1872
18	3	1879	1868	26.04102	1965	0	0	0	0	0	0	1965
19	3	1907	1896	26.42322	2004	0	11	1	0	11	2004	0
20	5	2147	2177	31.08276	2244	0	0	1	0	0	2244	0
21	3	2218	2207	26.23935	2334	19	11	1	0	30	2334	0
22	2	2272	2242	24.53318	2339	0	0	0	0	0	0	2339
23	3	2379	2368	22.44434	2465	0	0	0	0	0	0	2465
24	6	2434	2445	31.6651	2531	0	0	1	0	0	2531	0
25	4	2463	2474	28.05997	2571	0	11	0	0	11	0	2571
26	7	2624	2613	24.44761	2721	0	11	1	0	11	2721	0
27	3	2676	2665	29.57793	2762	0	0	0	0	0	0	2762
28	7	2941	2930	26.38107	3027	0	0	0	0	0	0	3027
29	2	3130	3100	33.36325	3197	0	0	0	0	0	0	3197
30	7	3392	3381	28.95563	3478	0	0	0	0	0	0	3478
31	4	3442	3453	36.27844	3539	0	0	1	0	0	3539	0
32	5	3511	3541	29.79057	3629	21	0	1	0	21	3629	0
33	5	3626	3656	31.1817	3723	0	0	1	0	0	3723	0
34	2	3698	3668	27.71068	3765	0	0	0	0	0	0	3765
35	5	3734	3764	30.49446	3831	0	0	1	0	0	3831	0
36	7	3783	3772	29.68826	3869	0	0	0	0	0	0	3869
37	4	4059	4070	28.65655	4156	0	0	1	0	0	4156	0
38	3	4083	4072	32.39124	4169	0	0	0	0	0	0	4169
39	3	4149	4138	31.23076	4246	0	11	1	0	11	4246	0
40	3	4166	4155	31.95871	4259	7	0	0	0	7	0	4259

Table C.5: Detailed Schedule Results for Input Set 1 Double Landing Pad using Hover and Rolling Horizon at 11.30-12.30 (Off-Peak)

Input Set 1 at 11.30-12.30					**Results for Double Landing Pad, Hover, RH**							
Flight	Origin	ETA$_A$ [s]	ETA$_B$ [s]	SOC$_{init}$ [%]	RTA [s]	$\Delta t_{shallow}$ [s]	$\Delta t_{l,af}$ [s]	AF [-]	$\Delta t_{l,h}$ [s]	Δt_l [s]	RTA$_A$ [s]	RTA$_B$ [s]
1	7	231	220	30.51401	328	0	11	1	0	11	328	0
2	2	273	243	40.64061	340	0	0	0	0	0	0	340
3	3	497	486	19.90593	583	0	0	0	0	0	0	583
4	6	614	625	34.19625	711	0	0	1	0	0	711	0
5	6	699	710	36.22335	801	5	0	1	0	5	801	0
6	3	846	835	28.55853	943	0	11	1	0	11	943	0
7	2	881	851	36.48354	948	0	0	0	0	0	0	948
8	4	962	973	38.68509	1059	0	0	1	0	0	1059	0
9	3	1103	1092	30.13649	1200	0	11	1	0	11	1200	0
10	7	1179	1168	24.12815	1265	0	0	0	0	0	0	1265
11	4	1225	1236	25.38067	1322	0	0	1	0	0	1322	0
12	4	1254	1265	27.99329	1362	0	11	0	0	11	0	1362
13	5	1398	1428	23.96314	1495	0	0	1	0	0	1495	0
14	7	1587	1576	29.49554	1673	0	0	0	0	0	0	1673
15	2	1708	1678	33.35738	1775	0	0	0	0	0	0	1775
16	4	1720	1731	29.53667	1817	0	0	1	0	0	1817	0
17	6	1764	1775	20.60132	1872	0	11	0	0	11	0	1872
18	3	1879	1868	26.04102	1965	0	0	0	0	0	0	1965
19	3	1907	1896	26.42322	2004	0	11	1	0	11	2004	0
20	5	2147	2177	31.08276	2244	0	0	1	0	0	2244	0
21	3	2218	2207	26.23935	2334	19	11	1	0	30	2334	0
22	2	2272	2242	24.53318	2339	0	0	0	0	0	0	2339
23	3	2379	2368	22.44434	2465	0	0	0	0	0	0	2465
24	6	2434	2445	31.6651	2531	0	0	1	0	0	2531	0
25	4	2463	2474	28.05997	2571	0	11	0	0	11	0	2571
26	7	2624	2613	24.44761	2721	0	11	1	0	11	2721	0
27	3	2676	2665	29.57793	2762	0	0	0	0	0	0	2762
28	7	2941	2930	26.38107	3027	0	0	0	0	0	0	3027
29	2	3130	3100	33.36325	3197	0	0	0	0	0	0	3197
30	7	3392	3381	28.95563	3478	0	0	0	0	0	0	3478
31	4	3442	3453	36.27844	3539	0	0	1	0	0	3539	0
32	5	3511	3541	29.79057	3629	21	0	1	0	21	3629	0
33	5	3626	3656	31.1817	3723	0	0	1	0	0	3723	0
34	2	3698	3668	27.71068	3765	0	0	0	0	0	0	3765
35	5	3734	3764	30.49446	3831	0	0	1	0	0	3831	0
36	7	3783	3772	29.68826	3869	0	0	0	0	0	0	3869
37	4	4059	4070	28.65655	4156	0	0	1	0	0	4156	0
38	3	4083	4072	32.39124	4169	0	0	0	0	0	0	4169
39	3	4149	4138	31.23076	4246	0	11	1	0	11	4246	0
40	3	4166	4155	31.95871	4259	7	0	0	0	7	0	4259

Table C.6: Detailed Schedule Results for Input Set 2 Single Landing Pad using Hover at 11.30-12.30 (Off-Peak)

Input Set 2 at 11.30-12.30					**Results for Single Landing Pad, Hover**					
Flight	Origin	ETA_A [s]	ETA_B [s]	SOC_{init} [%]	RTA [s]	$\Delta t_{shallow}$ [s]	$\Delta t_{l,af}$ [s]	AF [-]	$\Delta t_{l,h}$ [s]	Δt_l [s]
1	6	190	201	29.07511	332	0	0	1	0	0
2	6	271	282	27.95393	422	9	0	1	0	9
3	3	385	374	29.18883	516	0	0	0	0	0
4	5	548	578	33.66835	690	0	0	1	0	0
5	2	785	755	29.33468	897	0	0	0	0	0
6	2	950	920	30.28804	1062	0	0	0	0	0
7	2	984	954	35.14168	1152	56	0	0	0	56
8	7	1055	1044	28.12016	1242	56	0	0	0	56
9	5	1238	1268	29.32939	1380	0	0	1	0	0
10	2	1418	1388	38.7242	1530	0	0	0	0	0
11	2	1466	1436	24.39587	1620	42	0	0	0	42
12	7	1491	1480	29.29364	1710	88	0	0	0	88
13	3	1503	1492	36.62371	1800	166	0	0	0	166
14	7	1555	1544	35.27774	1890	204	0	0	0	204
15	4	1559	1570	31.4848	1980	279	0	1	0	279
16	5	1796	1826	37.26391	2070	132	0	1	0	132
17	2	1978	1948	29.42248	2250	160	0	0	0	160
18	2	2047	2017	37.6324	2160	1	0	0	0	1
19	2	2095	2065	37.30973	2340	133	0	0	0	133
20	6	2280	2291	30.98516	2430	8	0	1	0	8
21	6	2300	2311	27.24367	2700	258	0	1	0	258
22	7	2343	2332	30.36141	2610	136	0	0	0	136
23	4	2366	2377	29.78687	2520	12	0	1	0	12
24	7	2378	2367	27.51442	2790	281	0	0	0	281
25	5	2398	2428	28.66347	2880	340	0	1	0	340
26	7	2510	2499	35.87959	3060	360	0	0	59	419
27	7	2547	2536	30.20033	2970	292	0	0	0	292
28	4	2835	2846	34.02383	3150	173	0	1	0	173
29	6	2871	2882	31.87545	3240	227	0	1	0	227
30	6	3034	3045	27.40086	3420	244	0	1	0	244
31	7	3071	3060	30.52485	3330	128	0	0	0	128
32	7	3272	3261	28.05893	3510	107	0	0	0	107
33	2	3478	3448	19.7181	3600	10	0	0	0	10
34	6	3830	3841	37.79807	3972	0	0	1	0	0
35	4	4049	4060	29.29059	4191	0	0	1	0	0
36	3	4154	4143	34.92426	4285	0	0	0	0	0
37	3	4269	4258	34.30861	4400	0	0	0	0	0
38	3	4460	4449	33.62472	4591	0	0	0	0	0
39	2	4518	4488	32.77398	4681	51	0	0	0	51
40	3	4547	4536	20.3767	4771	93	0	0	0	93

Table C.7: Detailed Schedule Results for Input Set 2 Single Landing Pad using Hover and Rolling Horizon at 11.30-12.30 (Off-Peak)

Input Set 2 at 11.30-12.30					**Results for Single Landing Pad, Hover, RH**					
Flight	Origin	ETA_A [s]	ETA_B [s]	SOC_{init} [%]	RTA [s]	$\Delta t_{shallow}$ [s]	$\Delta t_{l,af}$ [s]	AF [-]	$\Delta t_{l,h}$ [s]	Δt_l [s]
1	6	190	201	29.07511	332	0	0	1	0	0
2	6	271	282	27.95393	422	9	0	1	0	9
3	3	385	374	29.18883	516	0	0	0	0	0
4	5	548	578	33.66835	690	0	0	1	0	0
5	2	785	755	29.33468	897	0	0	0	0	0
6	2	950	920	30.28804	1062	0	0	0	0	0
7	2	984	954	35.14168	1152	56	0	0	0	56
8	7	1055	1044	28.12016	1242	56	0	0	0	56
9	5	1238	1268	29.32939	1380	0	0	1	0	0
10	2	1418	1388	38.7242	1530	0	0	0	0	0
11	2	1466	1436	24.39587	1620	42	0	0	0	42
12	7	1491	1480	29.29364	1710	88	0	0	0	88
13	3	1503	1492	36.62371	1800	166	0	0	0	166
14	7	1555	1544	35.27774	1890	204	0	0	0	204
15	4	1559	1570	31.4848	1980	279	0	1	0	279
16	5	1796	1826	37.26391	2070	132	0	1	0	132
17	2	1978	1948	29.42248	2160	70	0	0	0	70
18	2	2047	2017	37.6324	2250	91	0	0	0	91
19	2	2095	2065	37.30973	2340	133	0	0	0	133
20	6	2280	2291	30.98516	2430	8	0	1	0	8
21	6	2300	2311	27.24367	2610	168	0	1	0	168
22	7	2343	2332	30.36141	2790	316	0	0	0	316
23	4	2366	2377	29.78687	2520	12	0	1	0	12
24	7	2378	2367	27.51442	2700	191	0	0	0	191
25	5	2398	2428	28.66347	2880	340	0	1	0	340
26	7	2510	2499	35.87959	3060	360	0	0	59	419
27	7	2547	2536	30.20033	2970	292	0	0	0	292
28	4	2835	2846	34.02383	3150	173	0	1	0	173
29	6	2871	2882	31.87545	3330	317	0	1	0	317
30	6	3034	3045	27.40086	3240	64	0	1	0	64
31	7	3071	3060	30.52485	3510	308	0	0	0	308
32	7	3272	3261	28.05893	3420	17	0	0	0	17
33	2	3478	3448	19.7181	3600	10	0	0	0	10
34	6	3830	3841	37.79807	3972	0	0	1	0	0
35	4	4049	4060	29.29059	4191	0	0	1	0	0
36	3	4154	4143	34.92426	4285	0	0	0	0	0
37	3	4269	4258	34.30861	4400	0	0	0	0	0
38	3	4460	4449	33.62472	4591	0	0	0	0	0
39	2	4518	4488	32.77398	4681	51	0	0	0	51
40	3	4547	4536	20.3767	4771	93	0	0	0	93

Table C.8: Detailed Schedule Results for Input Set 2 Double Landing Pad using Hover at 11.30-12.30 (Off-Peak)

Input Set 2 at 11.30-12.30					**Results for Double Landing Pad, Hover**							
Flight	Origin	ETA$_A$ [s]	ETA$_B$ [s]	SOC$_{init}$ [%]	RTA [s]	$\Delta t_{shallow}$ [s]	$\Delta t_{l,af}$ [s]	AF [-]	$\Delta t_{l,h}$ [s]	Δt_l [s]	RTA$_A$ [s]	RTA$_B$ [s]
1	6	190	201	29.07511	287	0	0	1	0	0	287	0
2	6	271	282	27.95393	377	9	0	1	0	9	377	0
3	3	385	374	29.18883	471	0	0	0	0	0	0	471
4	5	548	578	33.66835	645	0	0	1	0	0	645	0
5	2	785	755	29.33468	852	0	0	0	0	0	0	852
6	2	950	920	30.28804	1017	0	0	0	0	0	0	1017
7	2	984	954	35.14168	1081	0	30	1	0	30	1081	0
8	7	1055	1044	28.12016	1141	0	0	0	0	0	0	1141
9	5	1238	1268	29.32939	1335	0	0	1	0	0	1335	0
10	2	1418	1388	38.7242	1515	0	30	1	0	30	1515	0
11	2	1466	1436	24.39587	1533	0	0	0	0	0	0	1533
12	7	1491	1480	29.29364	1623	46	0	0	0	46	0	1623
13	3	1503	1492	36.62371	1605	5	11	1	0	16	1605	0
14	7	1555	1544	35.27774	1713	72	0	0	0	72	0	1713
15	4	1559	1570	31.4848	1695	39	0	1	0	39	1695	0
16	5	1796	1826	37.26391	1893	0	0	1	0	0	1893	0
17	2	1978	1948	29.42248	2045	0	0	0	0	0	0	2045
18	2	2047	2017	37.6324	2144	0	30	1	0	30	2144	0
19	2	2095	2065	37.30973	2162	0	0	0	0	0	0	2162
20	6	2280	2291	30.98516	2388	0	11	0	0	11	0	2388
21	6	2300	2311	27.24367	2397	0	0	1	0	0	2397	0
22	7	2343	2332	30.36141	2568	139	0	0	0	139	0	2568
23	4	2366	2377	29.78687	2487	24	0	1	0	24	2487	0
24	7	2378	2367	27.51442	2478	14	0	0	0	14	0	2478
25	5	2398	2428	28.66347	2577	82	0	1	0	82	2577	0
26	7	2510	2499	35.87959	2667	60	11	1	0	71	2667	0
27	7	2547	2536	30.20033	2658	25	0	0	0	25	0	2658
28	4	2835	2846	34.02383	2932	0	0	1	0	0	2932	0
29	6	2871	2882	31.87545	2979	0	11	0	0	11	0	2979
30	6	3034	3045	27.40086	3131	0	0	1	0	0	3131	0
31	7	3071	3060	30.52485	3157	0	0	0	0	0	0	3157
32	7	3272	3261	28.05893	3358	0	0	0	0	0	0	3358
33	2	3478	3448	19.7181	3545	0	0	0	0	0	0	3545
34	6	3830	3841	37.79807	3927	0	0	1	0	0	3927	0
35	4	4049	4060	29.29059	4146	0	0	1	0	0	4146	0
36	3	4154	4143	34.92426	4240	0	0	0	0	0	0	4240
37	3	4269	4258	34.30861	4355	0	0	0	0	0	0	4355
38	3	4460	4449	33.62472	4557	0	11	1	0	11	4557	0
39	2	4518	4488	32.77398	4585	0	0	0	0	0	0	4585
40	3	4547	4536	20.3767	4647	3	11	1	0	14	4647	0

Table C.9: Detailed Schedule Results for Input Set 2 Double Landing Pad using Hover and Rolling Horizon at 11.30-12.30 (Off-Peak)

Input Set 2 at 11.30-12.30					**Results for Double Landing Pad, Hover, RH**							
Flight	Origin	ETA$_A$ [s]	ETA$_B$ [s]	SOC$_{init}$ [%]	RTA [s]	$\Delta t_{shallow}$ [s]	$\Delta t_{l,af}$ [s]	AF [-]	$\Delta t_{l,h}$ [s]	Δt_l [s]	RTA$_A$ [s]	RTA$_B$ [s]
1	6	190	201	29.07511	287	0	0	1	0	0	287	0
2	6	271	282	27.95393	377	9	0	1	0	9	377	0
3	3	385	374	29.18883	471	0	0	0	0	0	0	471
4	5	548	578	33.66835	645	0	0	1	0	0	645	0
5	2	785	755	29.33468	852	0	0	0	0	0	0	852
6	2	950	920	30.28804	1017	0	0	0	0	0	0	1017
7	2	984	954	35.14168	1081	0	30	1	0	30	1081	0
8	7	1055	1044	28.12016	1141	0	0	0	0	0	0	1141
9	5	1238	1268	29.32939	1335	0	0	1	0	0	1335	0
10	2	1418	1388	38.7242	1515	0	30	1	0	30	1515	0
11	2	1466	1436	24.39587	1533	0	0	0	0	0	0	1533
12	7	1491	1480	29.29364	1605	17	11	1	0	28	1605	0
13	3	1503	1492	36.62371	1623	34	0	0	0	34	0	1623
14	7	1555	1544	35.27774	1713	72	0	0	0	72	0	1713
15	4	1559	1570	31.4848	1695	39	0	1	0	39	1695	0
16	5	1796	1826	37.26391	1893	0	0	1	0	0	1893	0
17	2	1978	1948	29.42248	2045	0	0	0	0	0	0	2045
18	2	2047	2017	37.6324	2144	0	30	1	0	30	2144	0
19	2	2095	2065	37.30973	2162	0	0	0	0	0	0	2162
20	6	2280	2291	30.98516	2388	0	11	0	0	11	0	2388
21	6	2300	2311	27.24367	2397	0	0	1	0	0	2397	0
22	7	2343	2332	30.36141	2478	49	0	0	0	49	0	2478
23	4	2366	2377	29.78687	2487	24	0	1	0	24	2487	0
24	7	2378	2367	27.51442	2568	104	0	0	0	104	0	2568
25	5	2398	2428	28.66347	2577	82	0	1	0	82	2577	0
26	7	2510	2499	35.87959	2667	60	11	1	0	71	2667	0
27	7	2547	2536	30.20033	2658	25	0	0	0	25	0	2658
28	4	2835	2846	34.02383	2943	0	11	0	0	11	0	2943
29	6	2871	2882	31.87545	2968	0	0	1	0	0	2968	0
30	6	3034	3045	27.40086	3131	0	0	1	0	0	3131	0
31	7	3071	3060	30.52485	3157	0	0	0	0	0	0	3157
32	7	3272	3261	28.05893	3358	0	0	0	0	0	0	3358
33	2	3478	3448	19.7181	3545	0	0	0	0	0	0	3545
34	6	3830	3841	37.79807	3927	0	0	1	0	0	3927	0
35	4	4049	4060	29.29059	4146	0	0	1	0	0	4146	0
36	3	4154	4143	34.92426	4240	0	0	0	0	0	0	4240
37	3	4269	4258	34.30861	4355	0	0	0	0	0	0	4355
38	3	4460	4449	33.62472	4557	0	11	1	0	11	4557	0
39	2	4518	4488	32.77398	4585	0	0	0	0	0	0	4585
40	3	4547	4536	20.3767	4647	3	11	1	0	14	4647	0

Table C.10: Detailed Schedule Results for Input Set 3 Double Landing Pad using Hover and Rolling Horizon at 7.30-8.30 (Peak)

Input Set 3 at 7.30-8.30					**Results for Double Landing Pad, Hover, RH**							
Flight	Origin	ETA$_A$ [s]	ETA$_B$ [s]	SOC$_{init}$ [%]	RTA [s]	$\Delta t_{shallow}$ [s]	$\Delta t_{l,af}$ [s]	AF [-]	$\Delta t_{l,h}$ [s]	Δt_l [s]	RTA$_A$ [s]	RTA$_B$ [s]
1	7	375	364	28.58987	461	0	0	0	0	0	0	461
2	4	382	393	31.74034	479	0	0	1	0	0	479	0
3	5	476	506	37.30611	573	0	0	1	0	0	573	0
4	4	543	554	34.4514	651	0	11	0	0	11	0	651
5	4	616	627	30.36875	713	0	0	1	0	0	713	0
6	2	650	620	38.77603	741	24	0	0	0	24	0	741
7	5	781	811	30.40599	878	0	0	1	0	0	878	0
8	4	838	849	23.56181	946	0	11	0	0	11	0	946
9	3	869	858	28.79306	968	2	11	1	0	13	968	0
10	3	974	963	34.12977	1060	0	0	0	0	0	0	1060
11	4	1003	1014	34.18891	1100	0	0	1	0	0	1100	0
12	3	1059	1048	35.08152	1150	5	0	0	0	5	0	1150
13	4	1285	1296	35.88057	1382	0	0	1	0	0	1382	0
14	6	1311	1322	26.1905	1419	0	11	0	0	11	0	1419
15	7	1377	1366	35.52142	1474	0	11	1	0	11	1474	0
16	7	1469	1458	27.22207	1555	0	0	0	0	0	0	1555
17	4	1470	1481	38.21727	1567	0	0	1	0	0	1567	0
18	7	1490	1479	35.39908	1645	69	0	0	0	69	0	1645
19	5	1532	1562	25.48025	1657	28	0	1	0	28	1657	0
20	7	1602	1591	38.74822	1735	47	0	0	0	47	0	1735
21	2	1854	1824	28.97735	1921	0	0	0	0	0	0	1921
22	6	1871	1882	32.71523	1968	0	0	1	0	0	1968	0
23	5	1940	1970	25.26487	2067	0	30	0	0	30	0	2067
24	5	1975	2005	38.23011	2072	0	0	1	0	0	2072	0
25	6	1999	2010	25.91683	2157	50	11	0	0	61	0	2157
26	6	2014	2025	29.55309	2162	51	0	1	0	51	2162	0
27	6	2110	2121	23.76183	2247	29	11	0	0	40	0	2247
28	4	2235	2246	34.06003	2332	0	0	1	0	0	2332	0
29	4	2248	2259	26.65689	2356	0	11	0	0	11	0	2356
30	5	2403	2433	28.87785	2500	0	0	1	0	0	2500	0
31	2	2480	2450	27.37409	2547	0	0	0	0	0	0	2547
32	6	2653	2664	26.8829	2750	0	0	1	0	0	2750	0
33	5	2735	2765	26.27976	2840	8	0	1	0	8	2840	0
34	4	2822	2833	35.56473	2930	0	11	0	0	11	0	2930
35	5	2831	2861	30.88788	2930	2	0	1	0	2	2930	0
36	7	2858	2847	36.36542	3020	76	0	0	0	76	0	3020
37	6	2931	2942	17.46463	3028	0	0	1	0	0	3028	0
38	5	2959	2989	31.21941	3118	62	0	1	0	62	3118	0
39	3	3007	2996	21.60195	3110	17	0	0	0	17	0	3110
40	7	3143	3132	24.91445	3229	0	0	0	0	0	0	3229
41	4	3197	3208	28.81186	3294	0	0	1	0	0	3294	0
42	7	3223	3212	31.8104	3319	10	0	0	0	10	0	3319
43	5	3330	3360	37.19306	3427	0	0	1	0	0	3427	0
44	6	3404	3415	31.58724	3517	16	0	1	0	16	3517	0
45	7	3469	3458	15.95705	3555	0	0	0	0	0	0	3555

The remainder of the flights was expected to arrived outside the scope of the rolling horizon and is thus not solved until next period.

Table C.11: Detailed Schedule Results of Day Simulation for Double Landing Pad using Hover and Rolling Horizon

Time of Day	λ **[1/hr]**	**Arrivals [-]**	**Max delay [s]**	**Total delay [s]**	**Average delay [s]**
0.00-1.00	5	0	0	0	0
1.00-2.00	10	10	11	22	2
2.00-3.00	6	6	11	11	2
3.00-4.00	12	9	11	11	1
4.00-5.00	30	25	12	44	1
5.00-6.00	30	23	68	155	5
6.00-7.00	44	28	37	182	4
7.00-8.00	72	70	167	2649	37
8.00-9.00	69	68	175	3067	44
9.00-10.00	62	49	149	642	10
10.00-11.00	41	27	63	201	5
11.00-12.00	33	29	30	86	3
12.00-13.00	34	34	78	255	8
13.00-14.00	53	52	107	944	18
14.00-15.00	45	35	52	331	7
15.00-16.00	74	51	309	2853	39
16.00-17.00	61	61	133	2236	37
17.00-18.00	59	53	180	2051	35
18.00-19.00	33	33	32	163	5
19.00-20.00	28	16	30	72	3
20.00-21.00	20	20	41	73	4
21.00-22.00	9	9	11	22	2
22.00-23.00	5	4	0	0	0
23.00-24.00	2	2	0	0	0
Daily	837	714	309	16070	23

C.2. Monte Carlo Simulations for eVTOL Arrival Sequencing & Scheduling

C.2.1. Monte Carlo Simulation of Hourly Average Delay

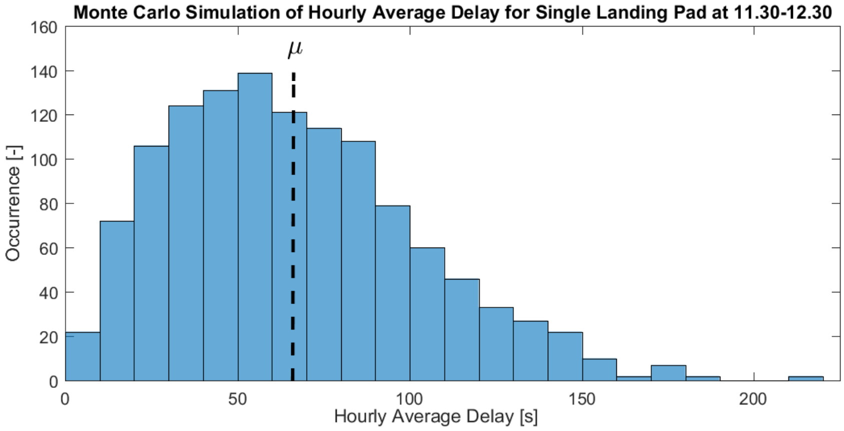

Figure C.1: Monte Carlo Simulation of Hourly Average Delay for Single Landing Pad using Hover and Rolling Horizon at 11.30-12.30

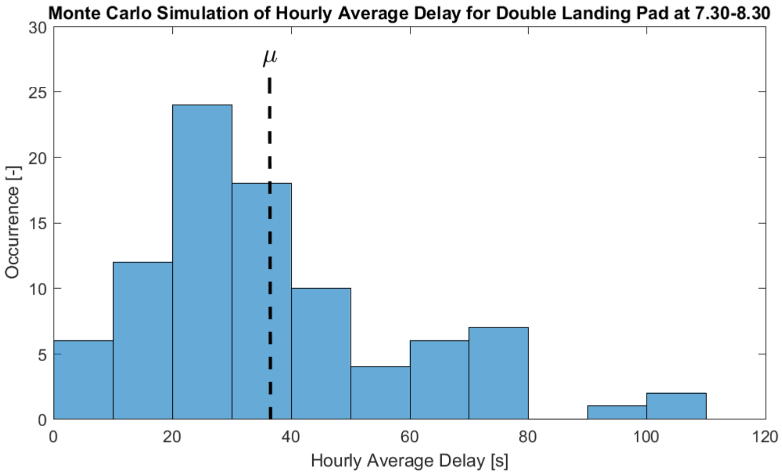

Figure C.2: Monte Carlo Simulation of Hourly Average Delay for Double Landing Pad using Hover and Rolling Horizon at 7.30-8.30

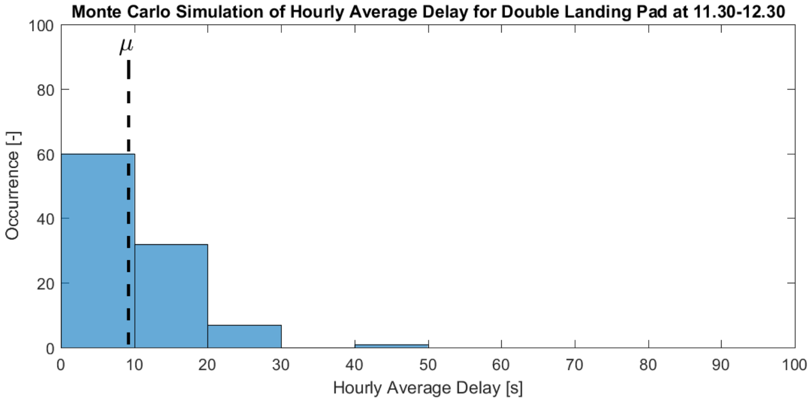

Figure C.3: Monte Carlo Simulation of Hourly Average Delay for Double Landing Pad using Hover and Rolling Horizon at 11.30-12.30

C.2.2. Monte Carlo Simulation of Hourly Maximum Delay

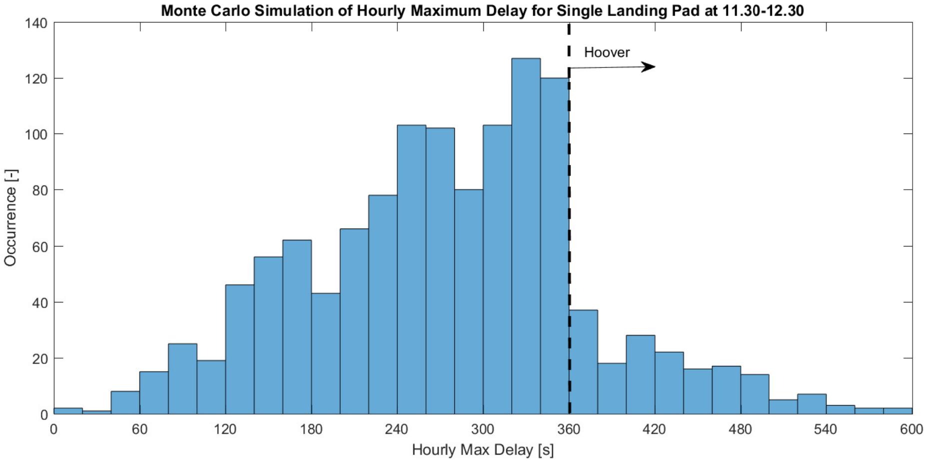

Figure C.4: Monte Carlo Simulation of Hourly Maximum Delay for Single Landing Pad using Hover and Rolling Horizon at 11.30-12.30

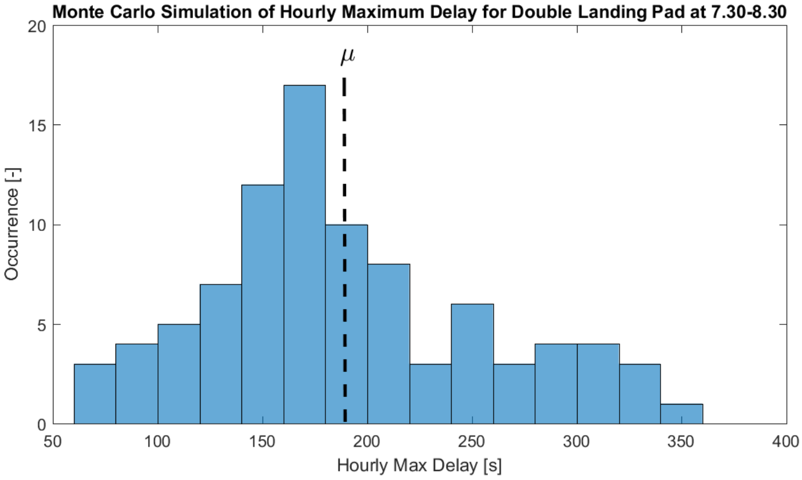

Figure C.5: Monte Carlo Simulation of Hourly Maximum Delay for Double Landing Pad using Hover and Rolling Horizon at 7.30-8.30

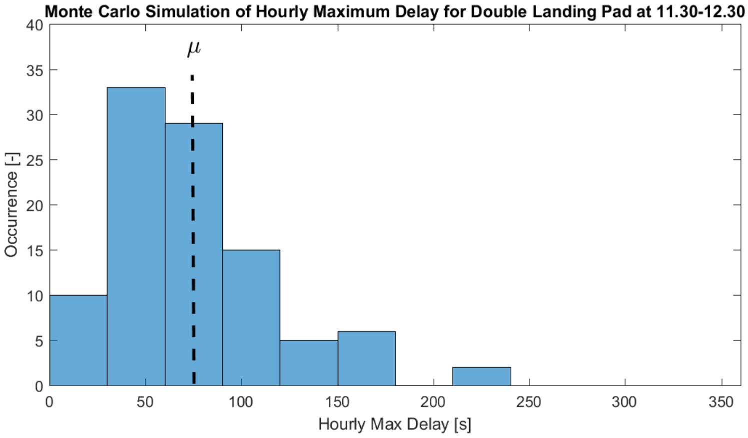

Figure C.6: Monte Carlo Simulation of Hourly Maximum Delay for Double Landing Pad using Hover and Rolling Horizon at 11.30-12.30

C.2.3. Monte Carlo Simulation of Hourly Total Delay

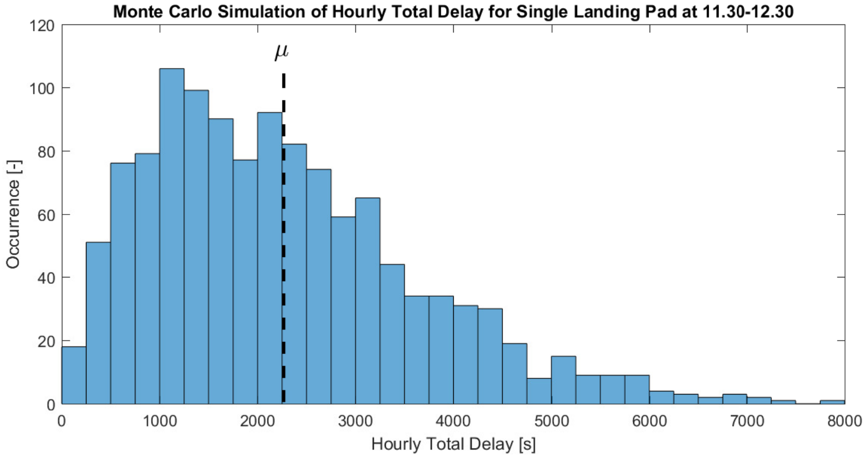

Figure C.7: Monte Carlo Simulation of Hourly Total Delay for Single Landing Pad using Hover and Rolling Horizon at 11.30-12.30

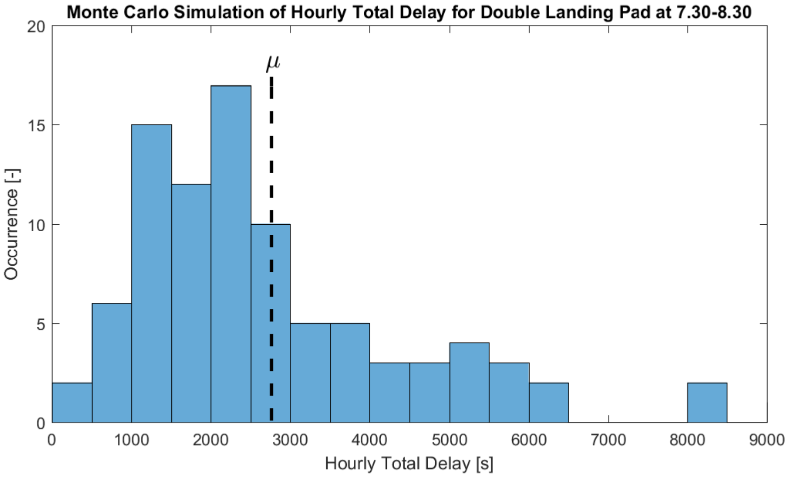

Figure C.8: Monte Carlo Simulation of Hourly Total Delay for Double Landing Pad using Hover and Rolling Horizon at 7.30-8.30

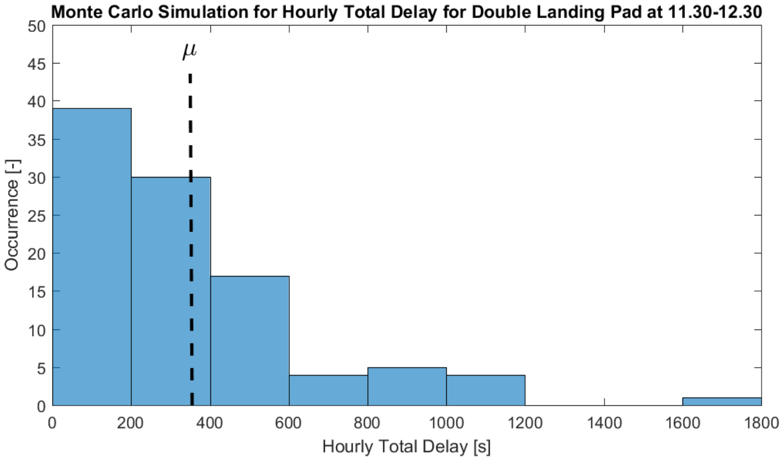

Figure C.9: Monte Carlo Simulation of Hourly Total Delay for Double Landing Pad using Hover and Rolling Horizon at 11.30-12.30

C.2.4. Monte Carlo Simulation of eVTOL Arrival Rate

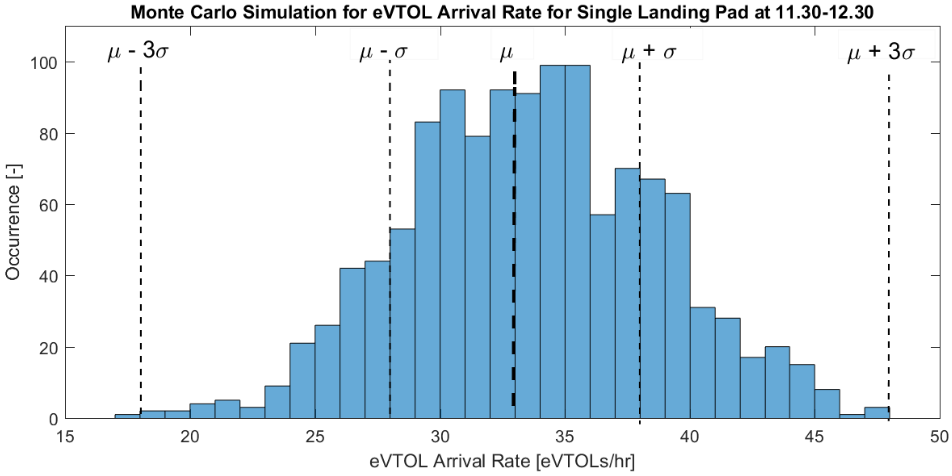

Figure C.10: Monte Carlo Simulation of eVTOL Arrival Rate for Single Landing Pad using Hover and Rolling Horizon at 11.30-12.30

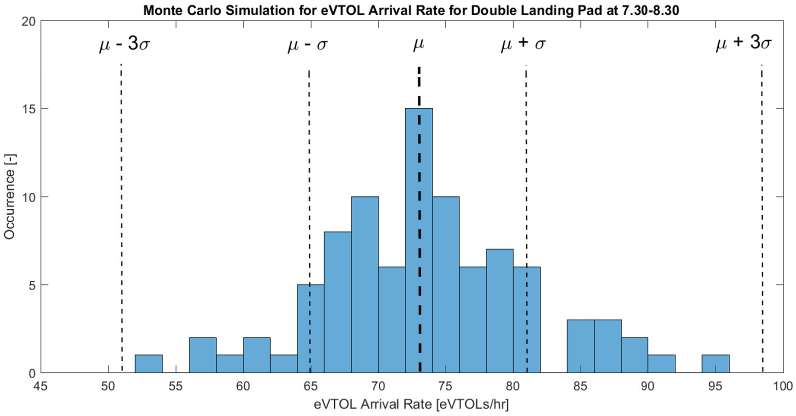

Figure C.11: Monte Carlo Simulation of eVTOL Arrival Rate for Double Landing Pad using Hover and Rolling Horizon at 7.30-8.30

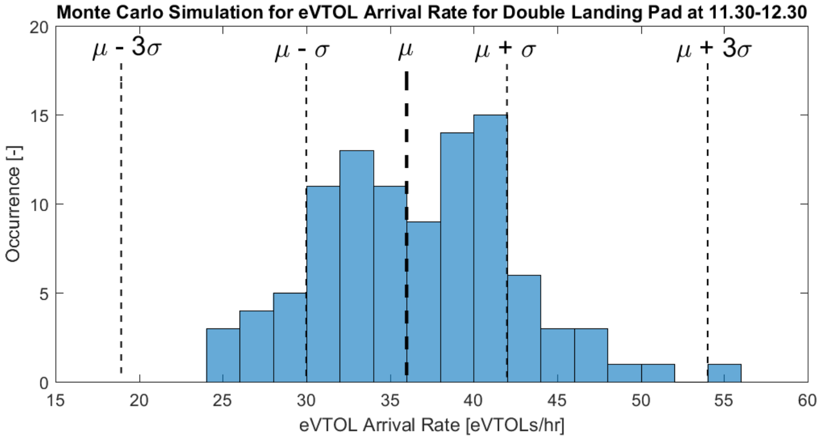

Figure C.12: Monte Carlo Simulation of eVTOL Arrival Rate for Double Landing Pad using Hover and Rolling Horizon at 11.30-12.30